

**AD-A218 175**

**DTIC FILE COPY**

①

FROM: AFIT/CI

7 July 1989

SUBJECT: Review of Thesis/Dissertation for Public Release

TO: PA

1. Request you review the attached for public release prior to being sent to DTIC.
2. Reply by indorsement to CI NLT \_\_\_\_\_.

*Ernest A. Haygood*  
ERNEST A. HAYGOOD, 1st Lt, USAF  
Executive Officer  
Civilian Institution Programs

1 Atch.  
THESIS 89-052  
HART

1st Ind., AFIT/PA

TO: CI

8 FEB 1990

Approved/Disapproved for public release.  
Log Number: 89-10-96

*Harriet D Moultrie*  
HARRIET D. MOULTRIE, Capt, USAF  
Director, Office of Public Affairs

**DTIC**  
**ELECTED**  
**FEB 22 1990**  
**S C E D**

## REPORT DOCUMENTATION PAGE

Form Approved  
OMB No. 0704-0188

1a. REPORT SECURITY CLASSIFICATION <b>UNCLASSIFIED</b>		1b. RESTRICTIVE MARKINGS <b>NONE</b>	
2a. SECURITY CLASSIFICATION AUTHORITY		3. DISTRIBUTION / AVAILABILITY OF REPORT <b>APPROVED FOR PUBLIC RELEASE; DISTRIBUTION UNLIMITED.</b>	
2b. DECLASSIFICATION / DOWNGRADING SCHEDULE			
4. PERFORMING ORGANIZATION REPORT NUMBER(S)		5. MONITORING ORGANIZATION REPORT NUMBER(S) <b>AFIT/CI/CIA- 89-052</b>	
6a. NAME OF PERFORMING ORGANIZATION <b>AFIT STUDENT AT PURDUE UNIVERSITY</b>	6b. OFFICE SYMBOL ( <i>If applicable</i> )	7a. NAME OF MONITORING ORGANIZATION <b>AFIT/CIA</b>	
6c. ADDRESS (City, State, and ZIP Code)		7b. ADDRESS (City, State, and ZIP Code) <b>Wright-Patterson AFB OH 45433-6583</b>	
8a. NAME OF FUNDING / SPONSORING ORGANIZATION	8b. OFFICE SYMBOL ( <i>If applicable</i> )	9. PROCUREMENT INSTRUMENT IDENTIFICATION NUMBER	
8c. ADDRESS (City, State, and ZIP Code)		10. SOURCE OF FUNDING NUMBERS	
		PROGRAM ELEMENT NO.	PROJECT NO.
		TASK NO.	WORK UNIT ACCESSION NO.
11. TITLE ( <i>Include Security Classification</i> ) ( <b>UNCLASSIFIED</b> ) An Aircraft Investigation of a Convective Boundary Layer Over Lake Michigan			
12. PERSONAL AUTHOR(S) <b>Mary L. Hart</b>			
13a. TYPE OF REPORT <b>THESIS/DISERTATION</b>	13b. TIME COVERED FROM _____ TO _____	14. DATE OF REPORT (Year, Month, Day) <b>1989</b>	15. PAGE COUNT <b>119</b>
16. SUPPLEMENTARY NOTATION <b>APPROVED FOR PUBLIC RELEASE IAW AFR 190-1 ERNEST A. HAYGOOD, 1st Lt, USAF Executive Officer, Civilian Institution Programs</b>			
17. COSATI CODES		18. SUBJECT TERMS ( <i>Continue on reverse if necessary and identify by block number</i> )	
FIELD	GROUP	SUB-GROUP	
19. ABSTRACT ( <i>Continue on reverse if necessary and identify by block number</i> )			
20. DISTRIBUTION / AVAILABILITY OF ABSTRACT <input checked="" type="checkbox"/> UNCLASSIFIED/UNLIMITED <input type="checkbox"/> SAME AS RPT. <input type="checkbox"/> DTIC USERS		21. ABSTRACT SECURITY CLASSIFICATION <b>UNCLASSIFIED</b>	
22a. NAME OF RESPONSIBLE INDIVIDUAL <b>ERNEST A. HAYGOOD, 1st Lt, USAF</b>		22b. TELEPHONE ( <i>Include Area Code</i> ) <b>(513) 255-2259</b>	22c. OFFICE SYMBOL <b>AFIT/CI</b>

**AN AIRCRAFT INVESTIGATION OF A CONVECTIVE BOUNDARY LAYER  
OVER LAKE MICHIGAN**

**A Thesis**

**Submitted to the Faculty**

**of**

**Purdue University**

**by**

**Capt. Mary L. Hart, USAF**

**In Partial Fulfillment of the**

**Requirements for the Degree**

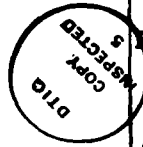
**of**

**Master of Science**

**1989**

**119 pages**

Accession For	
NTIS GRA&I	<input checked="" type="checkbox"/>
DTIC TAB	<input type="checkbox"/>
Unannounced	<input type="checkbox"/>
Justification	
By _____	
Distribution/ _____	
Availability Codes _____	
Dist	Avail and/or Special
DTIC COPY MSPECIFIED	
A-1	



## ABSTRACT

Hart, Mary L. M.S., Purdue University, May 1989. An Aircraft Investigation of a Convective Boundary Layer over Lake Michigan. Major Professor: Ernest M. Agee.

Meteorological data from research aircraft flights have been used to study the structure of a Type I Cloud-Topped Boundary Layer (CTBL) that formed as a result of air mass modification by a Cold Air Outbreak (CAO) over Lake Michigan on 10 January 1984. Surface and upper air data were used as a source of information to describe the synoptic scale conditions that accompanied the CAO event. Two NCAR research aircraft flew several legs across the lake at 43°N latitude, collecting 20 Hz data at five separate flight levels within the CTBL. These multiple data levels provided a unique opportunity to study in detail the structure of a Type I CTBL.

Vertical cross-sections of the CTBL were constructed using the aircraft data and assuming a steady-state in the north-south direction (parallel to the cloud streets) during the 1 hour and 50 minute time period covered by the flights. The cross-sections show a complex CTBL structure with off-shore flow from both Wisconsin and Michigan imposing lateral boundary conditions on the convection.

Spectral representations of the convective well-mixed boundary layer contained length scales of approximately 3, 10, and 30 km. These length scales correspond to the basic convective mode (BCM), a higher convective mode (HCM) which relates to organization within the 2-D cloud streets, and the length scale associated with Mesoscale Cellular Convection (MCC). The temperature, specific humidity, and vertical velocity spectra also indicated the presence of strong turbulence in the lower CTBL. This turbulence is a result of strong thermal forcing caused by a

large temperature difference between lake and atmosphere. The temperature spectra also showed evidence of turbulence at the top of the CTBL, where turbulent mixing between the boundary layer and inversion takes place.

Calculations of the variance, covariances, and skewness support the contention that two separate processes govern the turbulent transports within the Type I CTBL. The dominant process is thermal forcing, which is the primary means by which turbulent energy is generated. The second set of processes occur at the top of the CTBL, where entrainment instability and radiational cloud-top cooling also contribute, to a lesser extent, to the energy balance of the CTBL.

PURDUE UNIVERSITY

Graduate School

This is to certify that the thesis prepared

By Mary L. Hart

Entitled An Aircraft Investigation of a Convective Boundary Layer  
Over Lake Michigan

Complies with University regulations and meets the standards of the Graduate School for originality and quality

For the degree of Master of Science

Signed by the final examining committee:

Ernest M. Agee, chair  
Judith A. Eng  
Philip G. Smith

Approved by the head of school or department:

28 April 1989 W. H. Hart

is

This thesis  is not to be regarded as confidential

Ernest M. Agee  
Major professor

**AN AIRCRAFT INVESTIGATION OF A CONVECTIVE BOUNDARY LAYER  
OVER LAKE MICHIGAN**

**A Thesis**

**Submitted to the Faculty**

**of**

**Purdue University**

**by**

**Mary L. Hart**

**In Partial Fulfillment of the**

**Requirements for the Degree**

**of**

**Master of Science**

**May 1989**

## ACKNOWLEDGEMENTS

My thanks to my major professor, Dr. Ernest Agee, for his enthusiastic support of my thesis research. Thanks also to the other members of my committee: Dr. Judith A. Curry, Dr. Dayton Vincent, and Dr. Phil Smith. Their suggestions and comments were most helpful.

I would like to thank Carla Briener, Ross Aiken, and Dan Vietor for their help in arranging the final version of this work. I would also like to thank Marina Zivkovic for many enlightening conversations about the statistical interpretation of these data.

I would like to express my appreciation to the Air Force Air Weather Service for selecting me to attend graduate school, and making this thesis possible. Last, but not least, I would like to take this opportunity to thank my parents for the encouragement and moral support they have always given me.

This research has been sponsored by the National Science Foundation Mesoscale Dynamic Meteorology Program (NSF Grant ATM-8711611), and by the Department of the Navy – Office of Naval Research (Grant N00014-86-K-0179).

## TABLE OF CONTENTS

	Page
<b>LIST OF TABLES .....</b>	v
<b>LIST OF FIGURES .....</b>	vi
<b>ABSTRACT .....</b>	xi
<b>1. INTRODUCTION AND STATEMENT OF OBJECTIVES .....</b>	1
1.1 Literature Review .....	1
1.1.1 Onset of Steady 2-D Convection .....	4
1.1.2 Onset of Steady 3-D Convection .....	7
1.1.3 Rolls vs. Cells in the PBL .....	9
1.2 Statement of Research Objectives .....	11
<b>2. COLD AIR OUTBREAK .....</b>	12
2.1 Synoptic Scale Weather Pattern .....	12
2.2 Surface Data .....	14
2.3 Upper Air Data .....	16
<b>3. PROJECT LESS .....</b>	23
3.1 Background .....	23
3.2 Data Analysis Methodology .....	24
3.3 Instrument Specifications .....	26
<b>4. MESOSCALE CTBL ANALYSES .....</b>	28
4.1 Flight #85 Description .....	28
4.2 Raw Data Plots .....	31
4.2.1 U Wind Component .....	31
4.2.2 V and W Wind Components .....	33
4.2.3 Temperature Data .....	35
4.2.4 Specific Humidity Data .....	39
4.3 CTBL Features .....	41
4.3.1 Cross-section Methodology .....	42
4.3.2 Vertical PBL Cross-section .....	43

4.3.3 Michigan Land Breeze . . . . .	46
4.3.4 Weak Wisconsin Land Breeze . . . . .	47
4.3.5 Michigan Snow Band . . . . .	48
4.3.6 Mid-lake Snow Band . . . . .	48
4.3.7 Microscale Convective Features . . . . .	49
4.4 Spectral Decomposition . . . . .	50
4.5 Spectral Frequency Plots . . . . .	54
4.5.1 Specific Humidity Spectra . . . . .	54
4.5.2 Temperature and Virtual Potential Temperature Spectra .	59
4.5.3 U and V Wind Component Spectra . . . . .	63
4.5.4 Vertical Velocity Spectra . . . . .	67
4.6 Turbulent Fluxes . . . . .	73
4.6.1 Mean Profiles . . . . .	73
4.6.2 Covariance Calculations . . . . .	77
5. CLOUD PHYSICS . . . . .	86
5.1 Precipitation Processes . . . . .	86
6. SUMMARY AND CONCLUSIONS . . . . .	101
LIST OF REFERENCES . . . . .	106

**LIST OF TABLES**

Table	Page
3.1 The instrument specifications for the weather data collected by the NCAR King Air and Queen Air research aircraft .....	27
4.1 The first 30 wave numbers represented in the spectra of the aircraft data and their associated frequencies and wavelengths .....	53
4.2 Covariance, variance, and skewness values for a representative sample of the convective boundary layer .....	78
5.1 The instrument specifications for the microphysical data collected by the NCAR King Air and Queen Air research aircraft .....	87

## LIST OF FIGURES

Figure	Page
1.1 Rayleigh-Prandtl stability diagram for a wide range of supercritical Ra and Pr (from Krishnamurti, 1975) .....	3
1.2 Vertical profile of potential temperature for a Type I CTBL which included the transition layer where penetrative convection occurs (from Agee and Gilbert, 1989) .....	6
2.1 GOES satellite image for 10 January 1984 at 1930 GMT .....	13
2.2 Plot of surface data for 1200 and 1800 GMT on 10 January 1984 ...	15
2.3 500mb and 850mb analyses for 1200 GMT on 10 January 1984 ....	17
2.4 Analysis of inversion base heights calculated from 1200 GMT 10 January 1984 soundings in the vicinity of Lake Superior and Lake Michigan (from Agee and Gilbert, 1989) .....	18
2.5 Vertical cross-section of virtual potential temperature for 1200 GMT 10 January 1984. Surface intersection between STC and GRB, based on streamline analysis by Agee and Gilbert, 1989 .....	20
2.6 Height of the inversion base vs. fetch taken from aircraft observations during MIZEX and MASEX (from Walters, 1986) .....	21
4.1 The five flight levels of the NCAR King Air and Queen Air from 1812 to 1959 GMT during the cold air outbreak of 10 January 1984 .....	30
4.2 Plots of raw aircraft u wind component measurements (m/s) for flight levels 1 through 5 on 10 January 1984 .....	32
4.3 Plots of raw aircraft v wind component measurements (m/s) for flight levels 1 through 5 on 10 January 1984 .....	34
4.4 Plots of raw aircraft w wind component measurements (m/s) for flight levels 1 through 5 on 10 January 1984 .....	36

Figure	Page
4.5 Plots of raw aircraft ambient temperature measurements ( $^{\circ}\text{C}$ ) for flight levels 1 through 5 on 10 January 1984 .....	38
4.6 Plots of raw aircraft specific humidity measurements (g/kg) for flight levels 1 through 5 on 10 January 1984 .....	40
4.7 Vertical cross-sections for u wind component (m/s - top), virtual potential temperature ( $^{\circ}\text{K}$ - middle), and specific humidity (g/kg - bottom), based on the five research aircraft flight levels over Lake Michigan on 10 January 1984 .....	45
4.8 Cross-section of vertical velocity (m/s - 5km averages) .....	47
4.9 The five flight levels of the NCAR King Air and Queen Air aircraft, indicating the location of the inversion layer (A), the transition layer (B), the well-mixed boundary layer (C), and the Michigan land breeze (D) .....	51
4.10 Plots of detrended aircraft Lyman-alpha measurements (g/kg) for flight levels 1 through 5 on 10 January 1984 .....	55
4.11 Plots of detrended aircraft specific humidity measurements (g/kg) for flight levels 1 through 5 on 10 January 1984 .....	56
4.12 Spectral representations of the Lyman-alpha (left) and specific humidity (right) for the portions of flight levels 1 through 5 within the well-mixed CTBL .....	57
4.13 Plots of detrended aircraft ambient temperature measurements ( $^{\circ}\text{C}$ ) for flight levels 1 through 5 on 10 January 1984 .....	60
4.14 Plots of detrended aircraft virtual potential temperature measurements ( $^{\circ}\text{K}$ ) for flight levels 1 through 5 on 10 January 1984 .....	61
4.15 Spectral representations of the ambient temperature (left) and virtual potential temperature (right) for the portions of flight levels 1 through 5 within the well-mixed CTBL .....	62
4.16 Plots of detrended aircraft u wind component measurements (m/s) for flight levels 1 through 5 on 10 January 1984 .....	64
4.17 Plots of detrended aircraft u wind component measurements (m/s) for flight levels 1 through 5 on 10 January 1984 .....	65
4.18 Spectral representations of the u wind component (left) and v wind component (right) for the portions of flight levels 1 through 5 within the well-mixed CTBL .....	66

Figure	Page
4.19 Plots of raw aircraft w wind component measurements (m/s) for flight levels 1 through 5 on 10 January 1984 .....	69
4.20 Spectral representations of the w wind component, comparing the King Air (left) vs. the Queen Air (right) data .....	70
4.21 Spectral representations of the w wind component for the portions of flight levels 1 through 5 within the well-mixed CTBL. The log-log plot for level 5 (top right) shows -2/3 slope in the inertial subrange .....	72
4.22 Vertical profiles of the mean wind components, temperature and virtual potential temperature, and specific humidity .....	75
4.23 Variance of vertical velocity, the vertical TKE, and the horizontal covariances of vertical velocity .....	79
4.24 Measured covariances for heat and moisture .....	82
5.1 Vertical cross-section for relative humidity (%) based on the five research aircraft flight levels over Lake Michigan on 10 January 1984 .....	90
5.2 Vertical cross-sections for liquid water content, for particles of diameter 1.5 – 45 $\mu\text{m}$ ( $\text{g}/\text{m}^3$ – top), for particles of diameter $< 10 \mu\text{m}$ ( $\text{g}/\text{m}^3$ – middle), and for particles of diameter $\geq 10 \mu\text{m}$ ( $\text{g}/\text{m}^3$ – bottom), based on the five research aircraft flight levels over Lake Michigan on 10 January 1984 .....	92
5.3 Vertical cross-sections for FSSP concentrations, for particles of diameter 1.5 – 45 $\mu\text{m}$ ( $/\text{cm}^3$ – top), for particles of diameter $< 10 \mu\text{m}$ ( $/\text{cm}^3$ – middle), and for particles of diameter $\geq 10 \mu\text{m}$ ( $/\text{cm}^3$ – bottom), based on the five research aircraft flight levels over Lake Michigan on 10 January 1984 .....	96
5.4 Vertical cross-sections for particle concentrations ( $\text{cm}^{-3}$ – top), and the mean diameters ( $\mu\text{m}$ – bottom), for particles of diameter 300 – 4500 $\mu\text{m}$ from 1D-P (200Y) data, based on the five research aircraft flight levels over Lake Michigan on 10 January 1984 .....	99

## ABSTRACT

Hart, Mary L. M.S., Purdue University, May 1989. An Aircraft Investigation of a Convective Boundary Layer over Lake Michigan. Major Professor: Ernest M. Agee.

Meteorological data from research aircraft flights have been used to study the structure of a Type I Cloud-Topped Boundary Layer (CTBL) that formed as a result of air mass modification by a Cold Air Outbreak (CAO) over Lake Michigan on 10 January 1984. Surface and upper air data were used as a source of information to describe the synoptic scale conditions that accompanied the CAO event. Two NCAR research aircraft flew several legs across the lake at 43°N latitude, collecting 20 Hz data at five separate flight levels within the CTBL. These multiple data levels provided a unique opportunity to study in detail the structure of a Type I CTBL.

Vertical cross-sections of the CTBL were constructed using the aircraft data and assuming a steady-state in the north-south direction (parallel to the cloud streets) during the 1 hour and 50 minute time period covered by the flights. The cross-sections show a complex CTBL structure with off-shore flow from both Wisconsin and Michigan imposing lateral boundary conditions on the convection.

Spectral representations of the convective well-mixed boundary layer contained length scales of approximately 3, 10, and 30 km. These length scales correspond to the basic convective mode (BCM), a higher convective mode (HCM) which relates to organization within the 2-D cloud streets, and the length scale associated with Mesoscale Cellular Convection (MCC). The temperature, specific humidity, and vertical velocity spectra also indicated the presence of strong turbulence in the lower CTBL. This turbulence is a result of strong thermal forcing caused by a

large temperature difference between lake and atmosphere. The temperature spectra also showed evidence of turbulence at the top of the CTBL, where turbulent mixing between the boundary layer and inversion takes place.

Calculations of the variance, covariances, and skewness support the contention that two separate processes govern the turbulent transports within the Type I CTBL. The dominant process is thermal forcing, which is the primary means by which turbulent energy is generated. The second set of processes occur at the top of the CTBL, where entrainment instability and radiational cloud-top cooling also contribute, to a lesser extent, to the energy balance of the CTBL.

## 1. INTRODUCTION AND STATEMENT OF OBJECTIVES

### 1.1 Literature Review

In the field of fluid mechanics, convection is defined as the three-dimensional mass motion of a fluid that results in the transfer of fluid properties such as heat or momentum. Meteorologists have reserved the term convection specifically for the vertical transport of fluid properties in the atmosphere, and have accordingly introduced the term advection to describe horizontal atmospheric transport. Within the category of convection itself, there are more differentiations. Convection can be free or forced: forced convection is driven by external forcing (such as orographical or frontal lifting), and free convection is thermally driven by buoyancy effects. Convection is also classified in the atmosphere according to its vertical extent with respect to the tropospheric depth. Deep convection extends through the entire troposphere (as in thunderstorms), while shallow convection is limited to the planetary boundary layer (the bottom 1–2 km of the atmosphere).

Henri Benard (1901) was the first researcher to study shallow convection in a laboratory experiment. He used a thin layer of fluid (whale oil) at rest and heated it uniformly from below, producing a steady pattern of hexagonal convective cells. Lord Rayleigh (1916) developed a mathematical model that attempted to describe the convection seen in Benard's experiment. He invoked the Boussinesq approximations and solved the linear form of the momentum, continuity, state, and energy equations. Lord Rayleigh's solution showed that the convection was characterized by a non-dimensional parameter that now bears his name (the Rayleigh Number ( $R_a$ ), which was coined by Chandrasekhar (1957)).  $R_a$  represents a measure of the ratio of

buoyancy to the effects of friction (see Figure 1.1). The critical Rayleigh number indicates the threshold of buoyancy that a fluid heated from below (and/or cooled from above) needs to reach before convection can begin. Pellew and Southwell (1940) improved Rayleigh's convection model by artificially adding Christopherson's (1940) mathematical shape function to simulate hexagonal flow. Their new model created a realistic vertical velocity field with extrema at the cell centers and the vertices for hexagonal flows. Such models at that time were of little interest to meteorologists, because hexagonal convective cells were assumed not to occur in the atmosphere.

This state of affairs continued until satellite platforms for observing cloud patterns in the earth's atmosphere became available. In the 1960's, pictures of a group of hexagonal cloud cells over the North Atlantic Ocean revived interest in the possible relevance of Benard-Rayleigh convection to the atmosphere (see Kruger and Fritz, 1961). Hubert (1966) was the first to define the atmospheric convective cells as two groups: open and closed cells. Open cells have a clear area in the cell center with downward motion, and compensating upward motion in the cloudy cell walls. Closed cells have a cloudy center with upward motion, and clear air with downward motion in the walls. These types of cells seem to contradict classical fluid dynamics, where Palm (1960) showed that the vertical gradient of the kinematic viscosity determines the direction of the cell circulation (open or closed cells). In liquids, the viscosity decreases with increasing temperature and thus viscosity increases with height; the cells produced are closed (as convection begins at the bottom of the fluid). In gases, the viscosity decreases with height and decreasing temperature; the cells produced are open (the convection begins at the top of the fluid). Under these circumstances, one would not expect to find closed cells in the atmosphere.

Agee and Chen (1973) applied Palm's model to the atmosphere, and showed that the vertical gradient of the eddy diffusion coefficient will determine the

## Rayleigh-Prandtl Stability Diagram

where:

$$Ra = \frac{g \alpha \beta d^4}{\kappa \nu}$$

$$Pr = \frac{\nu}{\kappa}$$

$g$  = gravity acceleration constant

$\alpha$  = thermal expansion coefficient

$\beta$  = vertical temperature gradient ( $\Delta T / \Delta z$ )

$d$  = fluid depth

$\kappa$  = thermal conductivity

$\nu$  = kinematic molecular viscosity

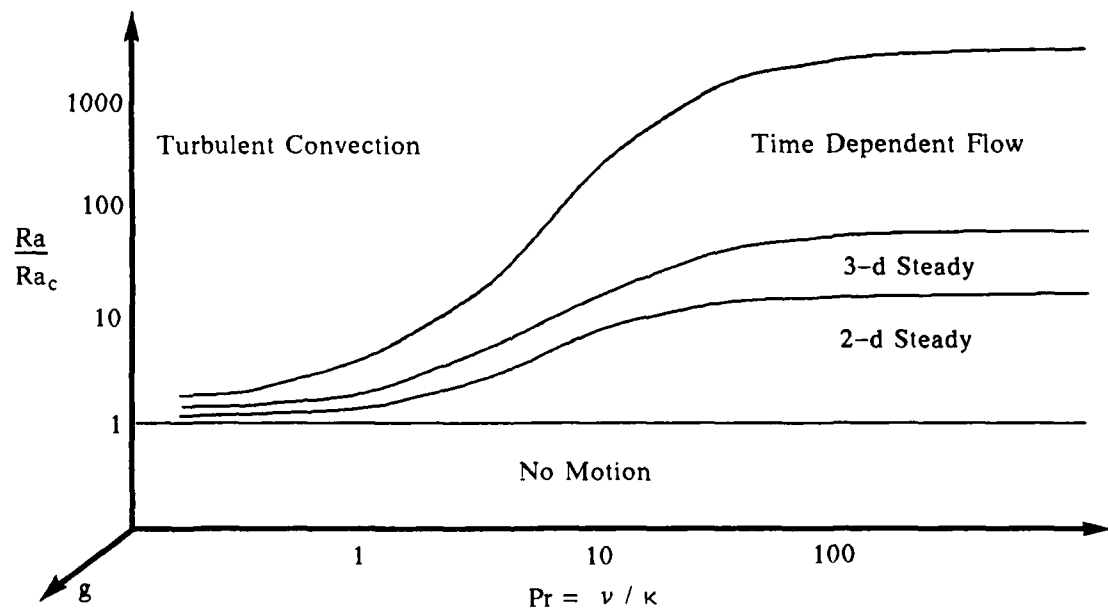


Figure 1.1 Rayleigh-Prandtl stability diagram for a wide range of super-critical Ra and Pr (from Krishnamurti, 1975).

circulation direction. If the sign of the vertical gradient changes, the circulation direction reverses. They concluded that both open and closed cellular arrays could occur in atmospheric thermal convection. Other physical mechanisms have also been seen to similarly affect the circulation direction. Krishnamurti (1975) showed numerically and experimentally that the large scale vertical motion affects the circulation direction, and Helfand and Kalnay (1983) demonstrated that local heating/cooling mechanisms in the boundary layer also can affect the circulation direction.

### 1.1.1 Onset of Steady 2-D Convection

Convection begins when the stability parameter (the Rayleigh number) reaches a critical value. Malkus and Veronis (1958) studied finite amplitude solutions in cellular convection. Under rigid/free boundary conditions they found that 2-D rolls will form as the initial instability, as opposed to 3-D hexagonal cells. As the heating continues and the Rayleigh number gradually increases, a new instability appears and the convection undergoes a transition (at approximately 10 times the critical Rayleigh number) to a hexagonal structure. A new steady state of convection is then established.

Krishnamurti (1970) experimented with fluids of differing viscosities (using a nondimensional parameter known as the Prandtl Number ( $\text{Pr}$ ) – see Figure 1.1). She found that a fluid heated from below and cooled from above will develop 2-D steady convective rolls when the Rayleigh number reaches a weakly supercritical  $\text{Ra}$ . This convective pattern will remain, until increased thermal forcing causes the Rayleigh number to reach a new critical threshold (at approximately 12 times the critical Rayleigh number). At that point, the convection becomes unstable and is transformed into steady 3-D convection. If the forcing continues to increase, the convecting fluid will reach additional transition points (see Zivkovic and Agee, 1988) enroute to its

change to turbulent convection. Classically speaking (see Kuo, 1979),  $\text{Ra} = 18 \times \text{Ra}_c$  is regarded as the transition point for laminar to turbulent convection. At this point, the turbulence increases the heat flux from a slope of  $1/4$  to  $1/3$ . Zivkovic and Agee have shown the subtleties of this transition out to  $50 \times \text{Ra}_c$ . Laboratory experiments have shown how the viscosity of the fluid affects how soon the convecting fluid will reach each transition point (and what the critical Rayleigh number will be for each transition). The lower the viscosity, the sooner the fluid will begin turbulent convection (and at lower Rayleigh numbers). Figure 1.1 shows the Rayleigh–Prandtl stability regimes for fluids, indicating the transition points between the types of convection.

Agee et. al. (1973) defined the atmospheric manifestation of Benard–Rayleigh convection as Mesoscale Cellular Convection (MCC). MCC is primarily found in Type I and Type II cloud-topped boundary layers (CTBL's) as discussed by Agee (1987). The types of CTBL's are differentiated by their geographic locations, time of year and the thermodynamic and dynamic forcing mechanisms that drive the convection. Type I CTBL's are generally observed to the east of continents in polar air streams over warm ocean currents, and are driven by heating from below. Type II CTBL's, alternatively, occur in the summer to the west of continents over cool currents. This convection is largely driven from above by cloud-top cooling and accompanying entrainment processes. This case study is of a cold air outbreak (CAO), which produces a Type I CTBL.

As noted above, the Type I MCC event is a wintertime phenomenon, usually seen off the east coasts of continents as well as over large middle and high latitude lakes (such as the U.S. Great Lakes). When the CAO begins, the stable cold air mass moves offshore and begins receiving heat and moisture from the warm ocean (or lake). As the air travels over the water, it begins to modify. Firstly, as noted in Figure

1.2, a shallow superadiabatic surface layer develops, then a deeper well-mixed layer capped by an inversion. The well-mixed layer usually contains a dry adiabatic subcloud layer and a moist adiabatic cloudy region (as shown). The transition layer identifies the mixing zone between the inversion and convection layers. After the air

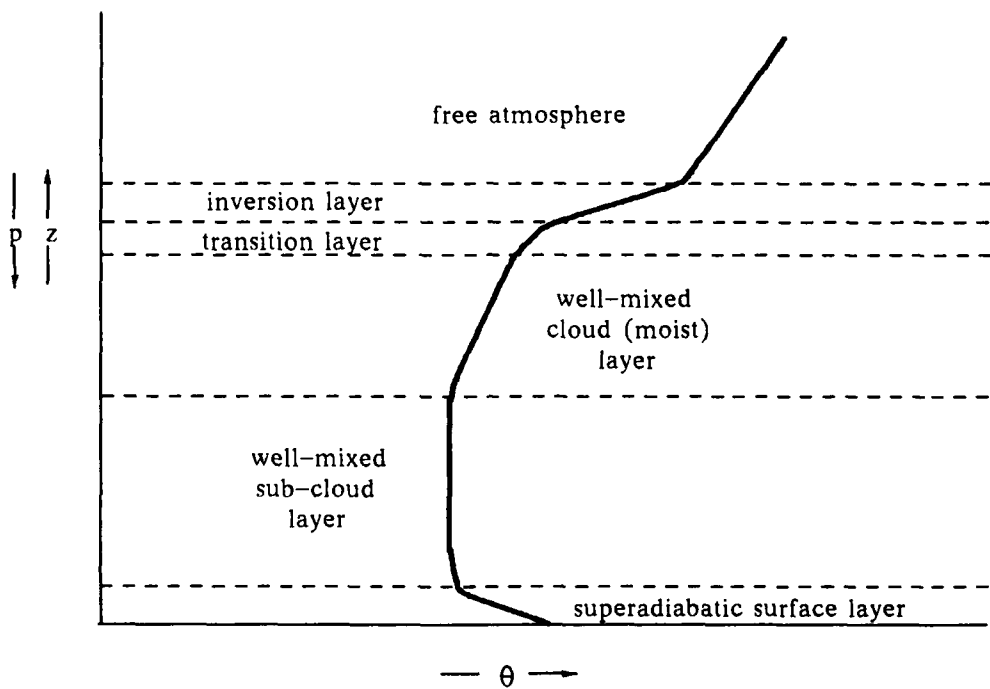


Figure 1.2 Vertical profile of potential temperature for a Type I CTBL which includes the transition layer where penetrative convection occurs (from Agee and Gilbert, 1989).

has modified sufficiently (over 200km fetch or 10 hours of time), 2-D cloud streets begin to form. The time for convection to begin is a function of the air-sea temperature difference  $\Delta T$  (Sheu and Agee, 1977, showed 16 hours for  $\Delta T > 5^\circ\text{C}$  in CAO events over the East China Sea during AMTEX). These streets, when viewed in satellite imagery, are the visible sign that 2-D steady convection is now established. For  $\Delta T \gg 5^\circ\text{C}$ , the time (and fetch) is much less.

In the CTBL, 2-D steady convection is manifested by longitudinal roll vortices, often sustained in the presence of vertical shear in the horizontal wind. With

increased thermal forcing, significantly strong wind shear can retain the 2-D structure (discussed in more detail in the next section). Rolls were observed over the ocean by LeMone (1973), who studied their structure and cross-roll wind component. Using aircraft flight data taken through the rolls, she showed their modulating effect on the distribution of turbulent kinetic energy (TKE) in the boundary layer (LeMone, 1976). Observational measurements over the ocean by Brümmer (1985) also showed how the roll vortices contribute to heat and momentum transport between the ocean and the top of the boundary layer. Mason and Sykes (1982) developed a numerical model of the roll vortices in a CTBL, which shows that the initial transport of heat and momentum is by boundary layer turbulence. Once convective rolls develop, however, heat and momentum are carried equally by the boundary layer turbulence and the roll vortices. Observations by Walter and Overland (1984) in a Type I CTBL over the Bering Sea showed that both thermal (convective) instability and dynamic (shear) instability contribute to the development of roll vortices.

### 1.1.2 Onset of Steady 3-D Convection

The transition from 2-D rolls to 3-D cells in the atmosphere depends on factors similar to those viewed in classical fluid mechanics. The temperature difference between the water surface and the air ( $\Delta T$ ), the length of time that the CAO continues, the amount of vertical shear in the CTBL, the size of the body of water (or fetch); all have an effect on when (or if) the 2-D convective cloud bands will give way to the open and/or closed 3-D convective cells. Generally, and as noted above, the 3-D structure is brought on by increased thermal forcing and an appropriate increase in the accompanying Ra. In order to study the detailed convective structure of the CTBL, aircraft observations are vitally important. Bunker (1960) took the first heat and moisture flux measurements – over the North Atlantic. Lenschow (1973) studied CTBL's over the Great Lakes and found them similar to maritime CTBL's in the

amount of heat and moisture transfer, and in the importance of thermal forcing. Lilly (1968) developed a model of a well-mixed boundary layer capped by stratus cloud and an inversion. In his model, radiative cooling was the forcing mechanism for the turbulent mixed layer (a case of a type II CTBL).

Strong thermal forcing from the surface is the main driving mechanism for the type I CTBL, but other mechanisms also contribute. The cloud tops can be destabilized by radiative forcing. The cloud top is cooled by longwave emission while just below the cloud top shortwave absorption heats the cloud, making the upper 100m of the cloud layer thermally unstable. Latent heat release (LHR) from the clouds also add to air parcel buoyancy. Entrainment from the dry capping inversion layer causes cloud evaporation, which can aid the sinking motion of negatively buoyant air (also see Randall, 1980). Small-scale turbulence due to both thermals and mechanical eddies is directly proportional to the entrainment process and a variety of physical mechanisms that contribute to the total kinetic energy (TKE) field. It can be further noted that preferred length scales may evolve within the CTBL that result from an upscale cascade of TKE (e.g. Moeng, 1986). It is also noted that the large scale vertical motion helps determine the cell circulation direction and vertical extent of the mixed layer (e.g. Krishnamurti, 1975).

The aspect ratio of a convective cell is defined as the ratio between the cell diameter and the depth of the convecting layer (the boundary layer depth for shallow convection). The aspect ratios of atmospheric convective cells are an order of magnitude larger than the ratios seen in classical fluid dynamics (30/1 vs. 3/1). Meteorologists have studied many physical processes that could possibly affect the cell structure. Van Delden (1985) showed the effect of latent heat release on cell expansion. Fiedler (1984) introduced the concept of 'Mesoscale Entrainment Instability' (MEI) for the instability mechanism at the top of the boundary layer,

which produces a larger length scale. Rothermel and Agee (1986) showed that extreme thermal forcing ( $800 \times Ra_c$ ) can produce cells with large aspect ratios, by the breakdown and coalescence of smaller cells into a few larger cells.

Rothermel and Agee (1980) used aircraft data from AMTEX (Air Mass Transformation EXperiment: 1974–75) to model a closed convective cell. Their model featured a double temperature cycle at low levels, where the cell center and cell vertices were warm with a cool region between. They hypothesized that the entrainment of warm air from the inversion and dry adiabatic subsidence worked along with heat transport from the surface to create this temperature profile. Ross and Agee (1985) also used AMTEX aircraft data to study the energy spectra of the CTBL. They found a Basic Convective Mode (BCM) that corresponds to the aspect ratio of Benard-Rayleigh convection ( $\lambda = 3\text{km}$ ) for a 1.5km deep CTBL. They compared the spectra of MCC and non-MCC convection and found that MCC convection has more energy in the longer wavelengths ( $\lambda = 30\text{km}$ ), indicating that energy is being transferred from the BCM to the MCC.

### 1.1.3 Rolls vs. Cells in the PBL

Miura (1986) did a survey of observational data of the Type I CTBL over eastern Asia, to compare the boundary layer profiles of the rolls and 2-D cloud streets with that of the 3-D cells. He found similar temperature and humidity profiles for both the rolls and the cells. A primary difference between a CTBL made up of rolls versus a CTBL with cells is the amount of vertical shear. Roll vortices are observed when the CTBL shear values are  $10^{-2} - 10^{-3} \text{ s}^{-1}$  or greater. The shear can dominate the convective process in spite of thermal forcing, and thus destroy any 3-D cells that try to develop during the course of the CAO. The 3-D convective cells are seen to develop when shear values are less than  $10^{-2} - 10^{-3} \text{ s}^{-1}$ , and sufficient heating is present in the CTBL. In the case of convection over the Great Lakes the fetch is

seldom long enough to allow 3-D cells to form. The heating, however, is strong ( $\Delta T = 30^{\circ}\text{C}$ ), which convectively mixes the layer in a short time, reducing the effective depth of the shear (from the upstream value over land). Studies of convection over the Great Lakes with an emphasis on lake-effect snowfall, have been common since the 1960's. Peace and Sykes (1966) conducted one of the first studies of snowfall on Lake Ontario. Their study of boundary layer winds and confluence/convergence in the snow bands was hampered by a lack of detailed observations that aircraft data sets can provide.

The University of Chicago Cloud Physics Group conducted a series of studies of convection over Lake Michigan, using aircraft and radar data, in the 1970's and 80's. Braham and Kelly (1982) studied the three most common convective structures over the lake: roll vortices (2-D streets), lake-induced mesolows, and land breeze convergence bands. Kelly (1984) followed up on this research with a two year study on winter convection, and found that the roll vortices are the most common convective structure during CAO's and that these patterns contribute the most to lake-effect snow accumulation. Passarelli and Braham (1981) studied the role of the winter land breeze from lower Michigan in aiding the convective bands over the lake to organize, as did Schoenberger (1984, 1986).

The Purdue Mesoscale Convection Research Group has also focused their attention on convection over Lake Michigan. Agee and Gilbert (1989) used aircraft data from Project LESS (Lake Effect Snow Studies: Dec 1983 – Jan 84) to study how a polar continental air mass is modified as it moves over the lake. The aircraft observations showed that an interfacial layer forms between the convective boundary layer and the capping inversion, as a result of the exchange of air parcels between the inversion and boundary layer. Figure 1.2 shows the detail of a Type I CTBL,

including the interfacial or entrainment zone between the moist mixed layer and the dry stable inversion.

### **1.2 Statement of Research Objectives**

This research has focused on the study of the Type I CTBL by doing an observational case study of a cold air outbreak over Lake Michigan on 10 Jan 1984. The special emphasis of this study has been to utilize multilevel research aircraft data and the spectral representations of these meteorological data to study the detailed structure of the convective boundary layer and embedded convection, snow bands, accompanying land breezes, and other CTBL features that developed during the CAO event. These aircraft data give information about five levels of the CTBL, so that horizontal and vertical profiles of meteorological variables and associated fluxes in the CTBL can be studied in more detail than has been previously possible. To achieve this objective, the following research goals were set:

1. Examine the dynamic and thermodynamic structure of the CTBL.
2. Determine the spectral peaks of organized mesoscale convection.
3. Determine magnitudes of the heat, momentum and moisture fluxes.
4. Examine the cloud physics and precipitation processes associated with the CTBL and large snow band.
5. Examine any of the above quantities on the length scale from 10's of meters to 10's of kilometers.
6. Use any findings to improve the CTBL conceptual model or the understanding of the process by which mesoscale convection becomes organized.

## 2. COLD AIR OUTBREAK

### 2.1 Synoptic Scale Weather Pattern

On 9 Jan 1984 a strong cold front associated with a low pressure system over northern Canada entered the Midwest region of the U.S., beginning a CAO that ended a period of mild weather. As the front moved across the Great Lakes region, widespread snow showers occurred over the northern Great Lakes. By 1200 GMT on the 10th, a strong high pressure system (1040mb) of continental polar (cP) origin was established over central Minnesota, and dominated the Midwest's weather. The cold front had moved to the east and was causing precipitation over the Ohio Valley and Appalachian mountains.

The high pressure system caused light to moderate north-northwesterly flow over the region, providing good conditions for the formation of a Type I CTBL over Lake Michigan. The 1930 GMT satellite picture (see Fig 2.1) shows Wisconsin and Minnesota under the influence of a dry, stable air mass. The clear skies over a snow-covered land surface further indicate that the new air mass over the Midwest is of continental polar origin (see Pettersen, 1956; and Curry, 1983). A large temperature difference between the polar air mass and unfrozen lakes established conditions for strong thermal forcing and convection (as can be seen by the 2-D cloud streets over Lake Superior and Lake Michigan). The orientation of the streets over both of the lakes is almost due north-south. The convection over Lake Michigan caused lake-effect snow along the southern and eastern shores of the lake. The southeast corner of Lake Michigan seems relatively cloud free, indicating a possible land-breeze effect. That effect can also be seen in the eastern most cloud

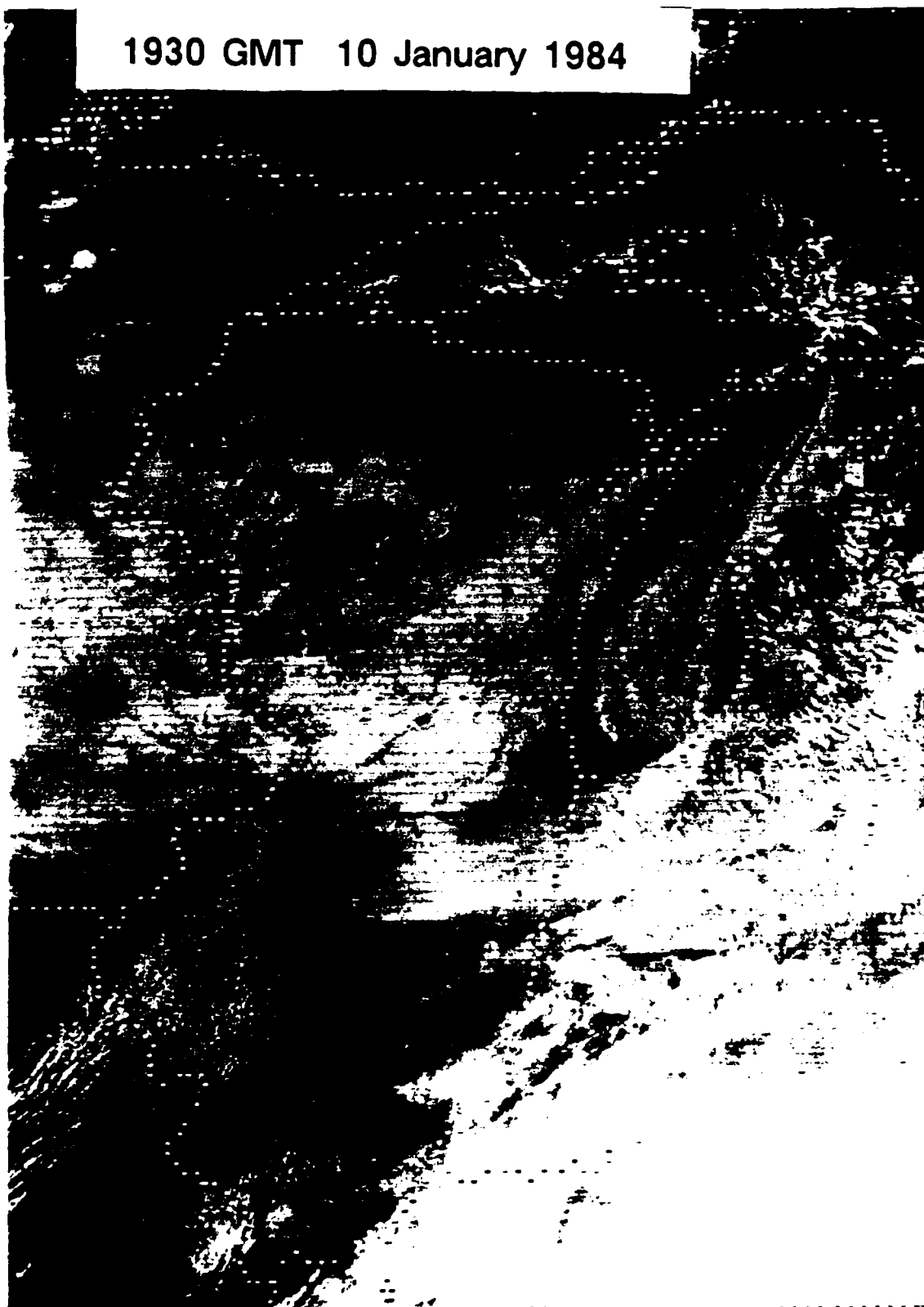


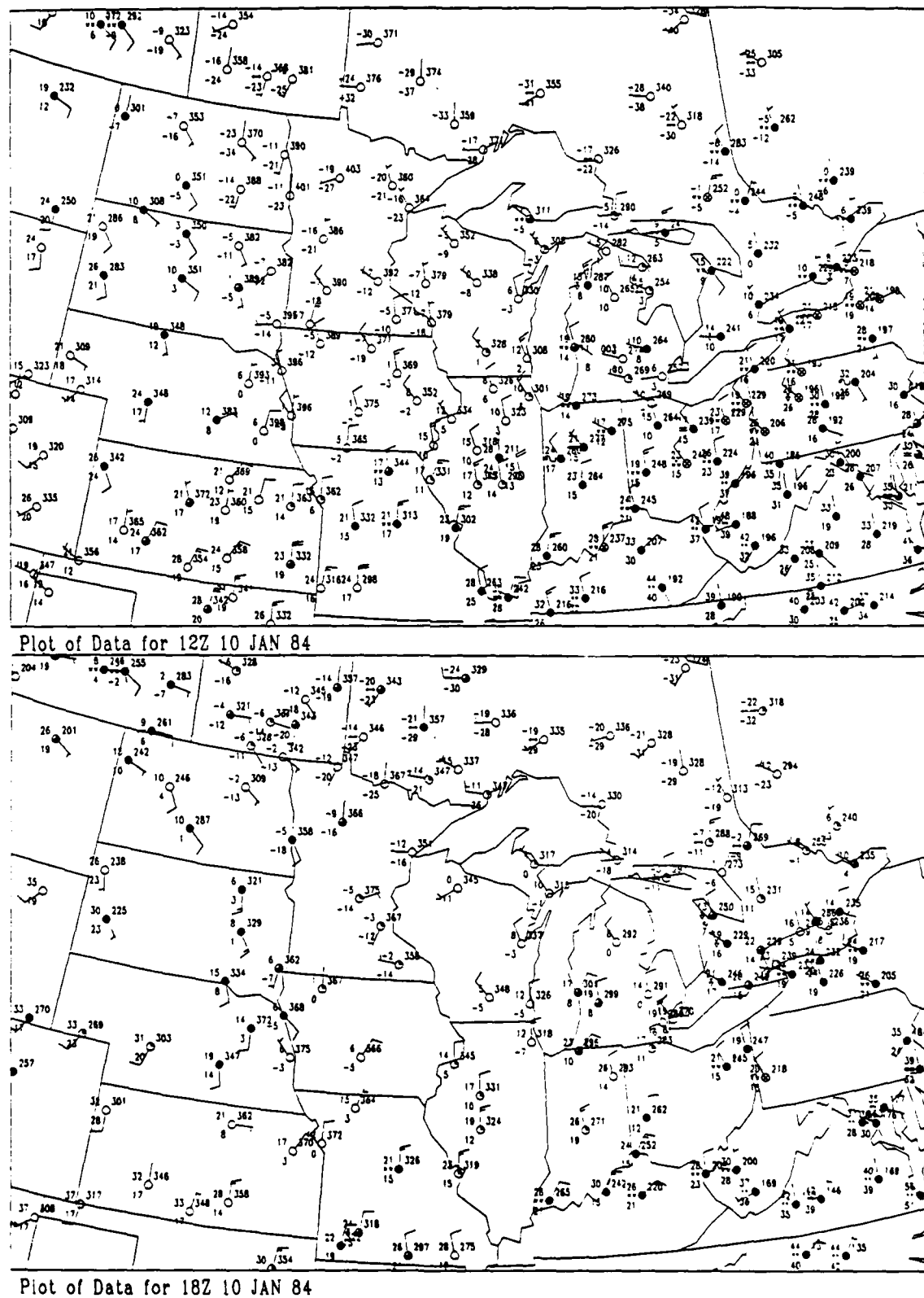
Figure 2.1 GOES satellite image for 10 January 1984 at 1930 GMT.

street - where a larger and better defined cloud band suggests a band of convergence caused by the collision of a land breeze with the mean flow over the lake. This is also observed to occur when the CAO is more northerly than westerly.

The high pressure system continued to dominate the weather and fuel convection over the lake for the next 24 hours. The high slowly shifted east during this period, and the northwest flow gradually changed to a weaker more westerly flow (by 1200 GMT on 11 Jan 1984), as the next weather system developed over the Great Plains. The 2-D convection over Lake Michigan continued, but as the mean flow weakened, the land breeze effect came to increasingly dominate the convection. Before the convection ended, the cloud streets had been concentrated into one convective band along the Wisconsin shore at 1500 GMT on 11 Jan 1984.

## 2.2 Surface Data

Figure 2.2 shows 1200 and 1800 GMT surface maps for the Midwest. At 1200 GMT, the mean flow over the Great Lakes region is from the north-northwest. The air over eastern Wisconsin was partially modified by its path over Lake Superior, as can be seen by the  $15^{\circ}\text{C}$  east-west temperature gradient across the state of Wisconsin, and the  $12^{\circ}\text{C}$  gradient in dewpoint. Since the air flow followed a path over both Lake Superior and Lake Michigan the air mass over southeastern Michigan and northern Indiana was more modified. The cloud cover, precipitation, and higher temperatures and dewpoints reported there show that heat and moisture have been transferred from the lakes to the boundary layer. Frontal-induced cloudiness is well to the southeast, so the precipitation over the Great Lakes region is due solely to the lake-effect (also see Fig 2.1). There is some evidence of a weak mesoscale trough over southern Lake Michigan in the 1200 GMT pressure analysis (not shown), most likely induced by the warming influence of the water. This feature could also be an early indication that a land breeze situation is setting up (Passarelli and Braham,



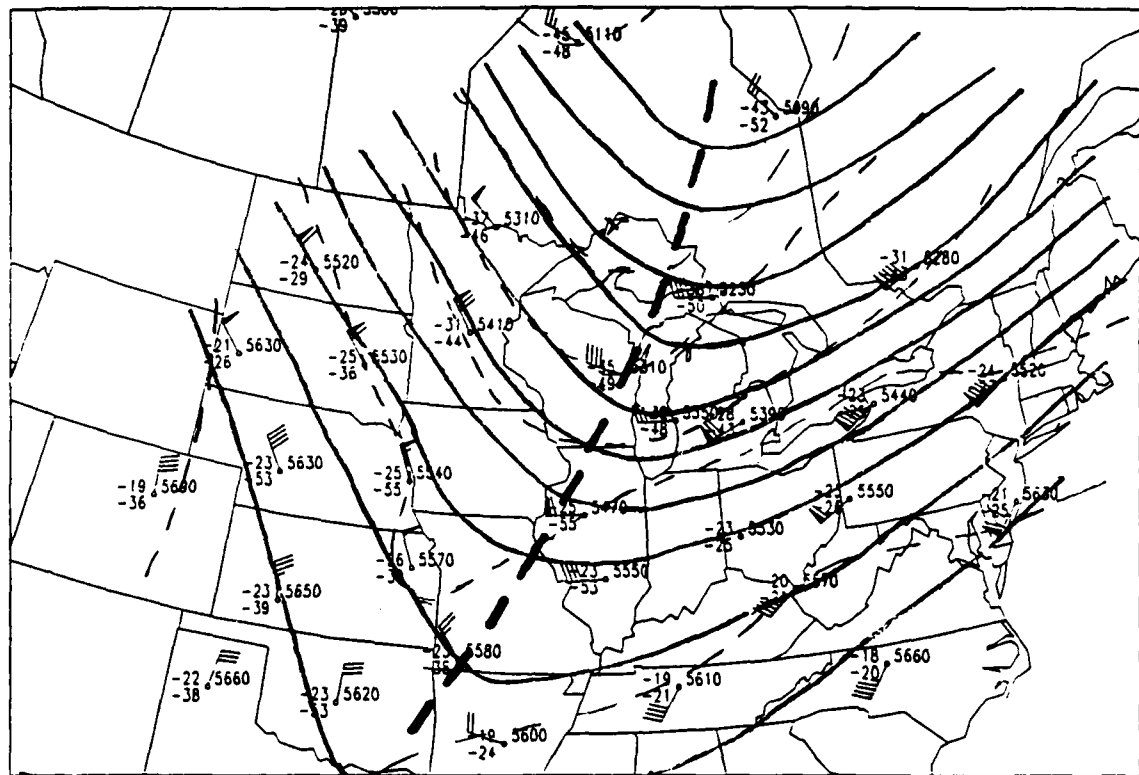
1981).

By 1800 GMT, the conditions have continued to change along the eastern shore of Lake Michigan. The winds at Muskegon (MKG) are now from the northeast and over the rest of Michigan the winds are almost due north. The southwest corner of the state remains cloudy, but the precipitation has stopped. This wind-shift points to a local land breeze, and explains the enhanced cloud band over Lake Michigan and the relative lack of clouds found over the southeast shore of the lake on the 1930 GMT satellite picture. In Chapter 4 the mesoscale data are examined to further determine the strength and character of this land breeze phenomenon.

### 2.3 Upper Air Data

A broad trough is positioned over the eastern U.S., over the Great Lakes region, at 1200 GMT on Jan 10 (see Figure 2.3). At 850mb the axis of the pressure trough is found over the eastern part of the Great Lakes region. The thermal trough is located over the western Great Lakes, and northwest flow with cold air advection (CAA) is strong over the entire Midwest. The winds between the surface and 850mb are backing from north-northwest at the surface to northwest at 850mb – another indication of the CAA. The airmass over the western Great Lakes is dry, with dewpoint depressions that are  $5^{\circ}$  to  $15^{\circ}\text{C}$ . On the lee (eastern) side of the Great Lakes the dewpoint depressions are within  $1^{\circ}$  to  $2^{\circ}\text{C}$ , indicating that the lakes were able to quickly modify the airmass. The small dewpoint depressions are evidence that the height of the convective boundary layer on the lee side of the lakes must be above the 850mb level. In fact, Figure 2.4 (taken from Agee and Gilbert, 1989) shows the analysis of convection depth of the PBL over the western Great Lakes region. Further, the 850mb heights in Figure 2.3 are seen to lie below the convective depth values of 1908m, 2440m, and 1730m, measured at MKG, NWI, and KNX, respectively.

At the 500mb level the pressure trough and the thermal trough are nearly



Plot of 500 mb Data for 12Z 10 JAN 84

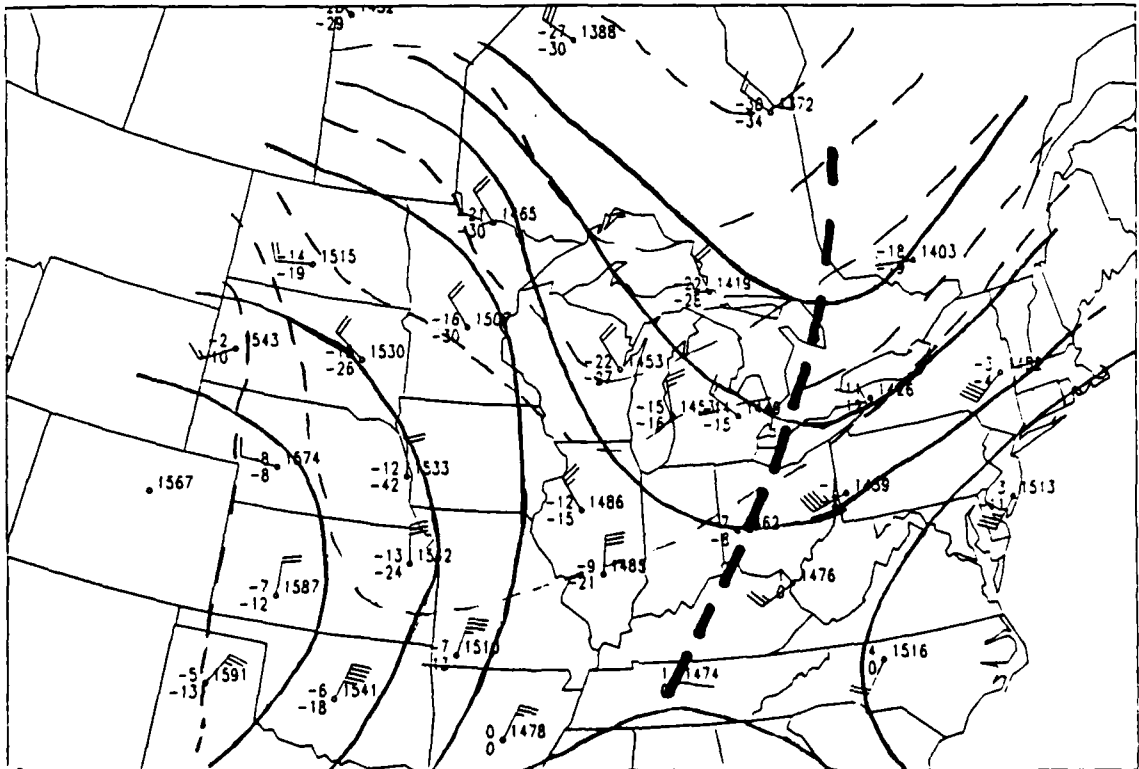


**Figure 2.3** 500 mb and 850 mb analyses for 1200 GMT on 10 January 1984.

INVERSION BASE HEIGHTS (m) 12Z 10 JAN 84

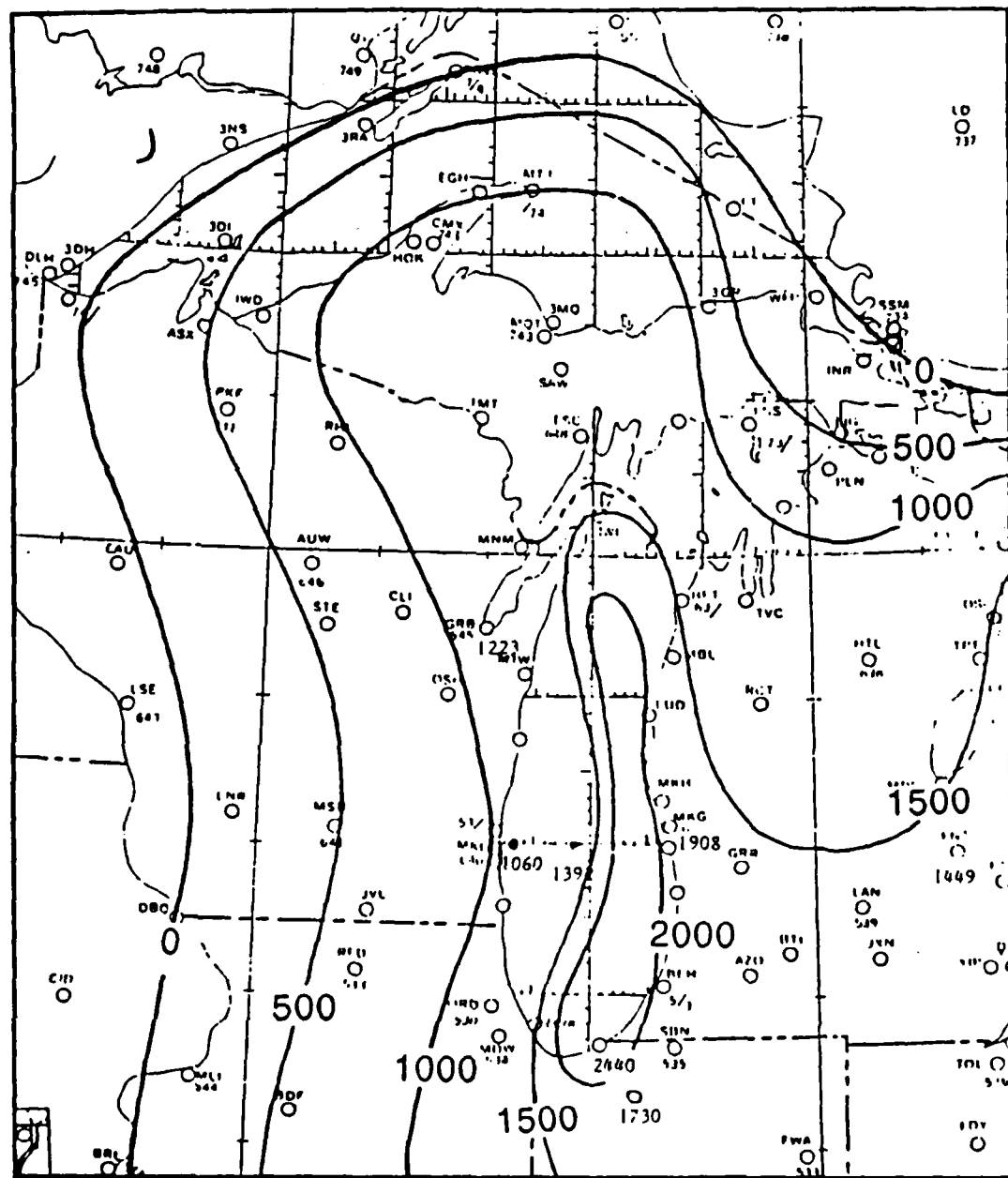


Figure 2.4 Analysis of inversion base heights calculated from 1200 GMT 10 January 1984 soundings in the vicinity of Lake Superior and Lake Michigan (from Agee and Gilbert, 1989).

aligned with each other, and the trough axis is just west of Lake Michigan. The mean flow over Lake Michigan is westerly, with weak CAA. There is a mid-level jet over the eastern U.S., with the jet axis to the south of Lake Michigan over central Indiana, and a jet max of 95kts over the eastern Great Lakes. The winds between 850 and 500mb continue to back, indicating CAA between these levels.

Figure 2.5 is a virtual potential temperature ( $\theta_v$ ) cross section of the western Great Lakes region. This vertical profile of  $\theta_v$  is on a line through the following locations: St. Cloud, Minn. (STC); Green Bay, Wis. (GRB); western Lake Michigan ( $43^{\circ}\text{N}$ ,  $87.4^{\circ}\text{W}$ ); eastern Lake Michigan ( $43^{\circ}\text{N}$ ,  $86.8^{\circ}\text{W}$ ); Muskegon, Mich. (MKG); and Flint, Mich. (FNT). The cross section shows how both Lake Superior and Lake Michigan have served to modify the air mass.

At STC the  $\theta_v$  profile shows unmodified cP air, with a strong vertical gradient indicating the stability of the air mass. Further east over Wisconsin, the cross section has a weaker vertical gradient. This weakening of the stability is due to the influence of thermal forcing over Lake Superior. The convective boundary layer is first seen over western Wisconsin, where the isopleths begin to intersect the ground. The influence of Lake Superior is weak due to a short fetch, and the CTBL height increases only gradually as one moves east toward GRB.

The  $\theta_v$  profile over Lake Michigan shows that the strong thermal forcing over a longer fetch (400 km) had a strong modifying influence on the air mass and the depth of the convective PBL. This is reasonably consistent with the results by Walters (1986), shown in Figure 2.6. The isopleths near the surface of the lake are almost vertical, and the height of the CTBL increases dramatically to almost 800 mb. The east-west  $\theta_v$  gradient over the lake is only  $3^{\circ}$  to  $5^{\circ}\text{C}$ , as the mean flow is almost due north and the north-south lake orientation makes the fetch along the east and west lake shores almost equal. Again, the largest CTBL heights are found over the eastern

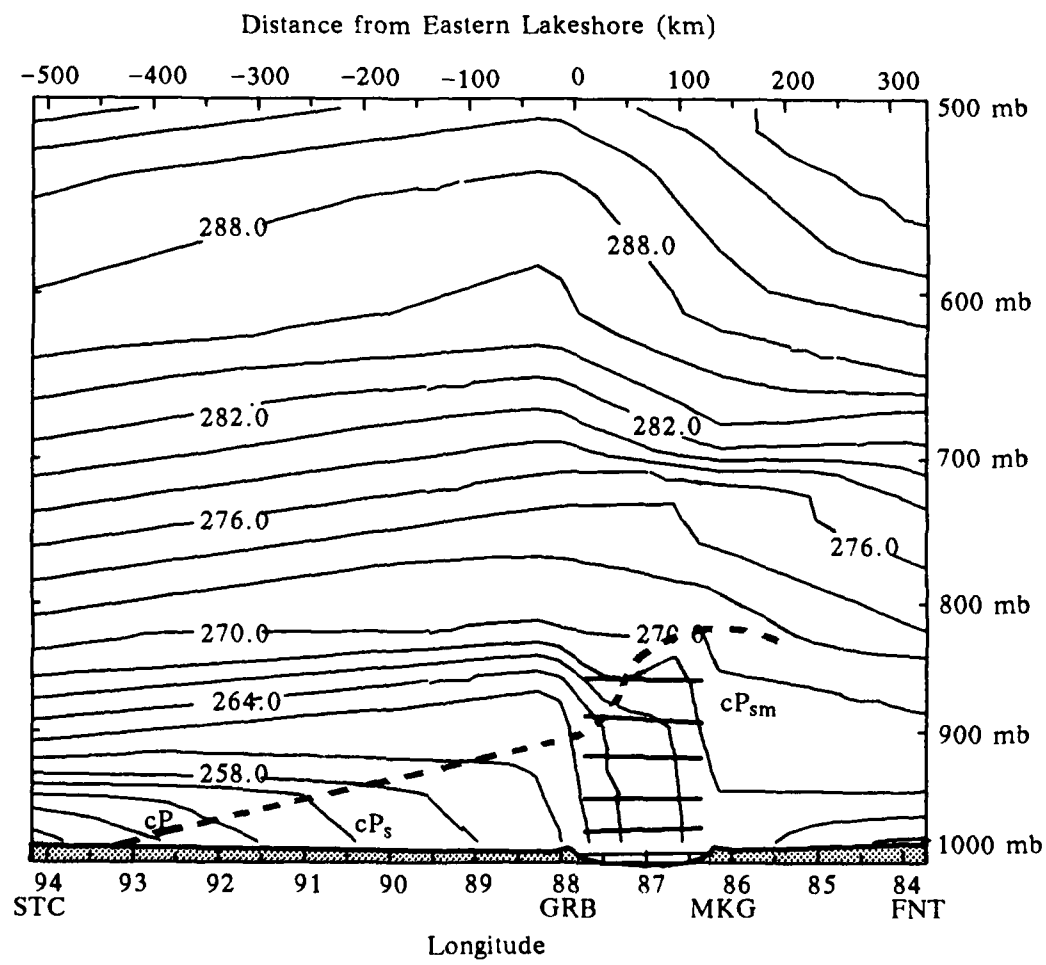


**Figure 2.5** Vertical cross-section of virtual potential temperature  $\theta_v$  for 1200 GMT 10 January 1984. Surface intersection between STC and GRB, based on streamline analysis by Agee and Gilbert, 1989.

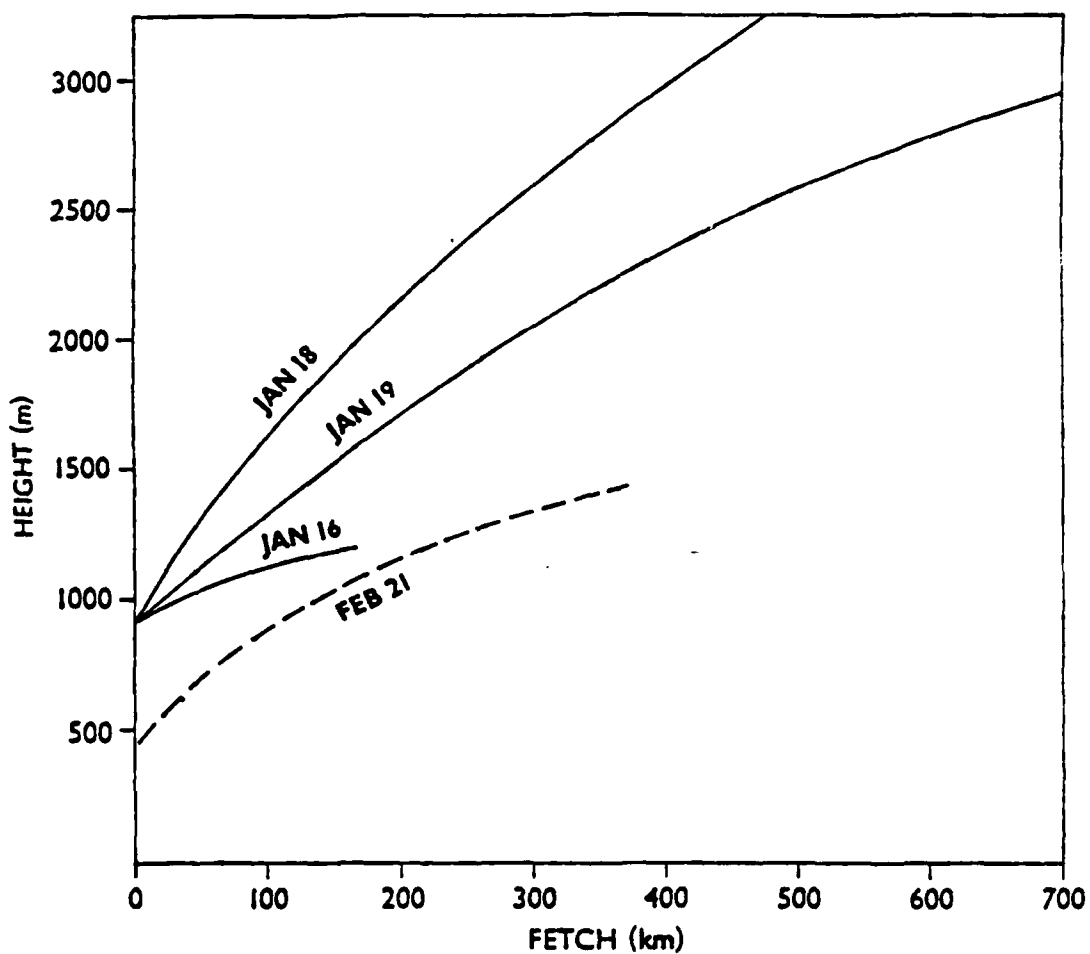


Figure 2.6 Height of the inversion base vs. fetch taken from aircraft observations during MIZEX and MASEX (from Walters, 1986).

half of the lake and near the south shore in northwest Indiana (see Fig 2.4). The height of the CTBL at MKG (1908m) is approximately 500m lower than the maximum (2440m) over northern Indiana.

Conventional surface and upper air data lack the resolution needed to examine the CTBL in enough detail to see the mesoscale and microscale features. Special aircraft data collected over Lake Michigan on 10 Jan 1984 were used in this case study to more closely examine the Type I CTBL. The location of these data in relation to CTBL location is also shown in Figure 2.5.

### 3. PROJECT LESS

#### 3.1 Background

Project LESS (Lake Effect Snow Studies) was a cooperative meteorological field experiment that ran from 1 Dec 1983 to 24 Jan 1984. The purpose of the experiment was to collect data in the vicinity of Lake Michigan, with a special emphasis on Cold Air Outbreaks (CAO's) and how cold air is modified as it travels over warm water (Rokosz, 1985).

The following groups were involved in the LESS field program: the University of Chicago Cloud Physics Group, located at Muskegon, Michigan (MKG); the Purdue Mesoscale Convection Research Group, located at the Indiana Dunes National Lakeshore Headquarters in Porter, IN (NWI); and the National Center for Atmospheric Research (NCAR) which provided specialized field equipment used to collect supplemental observations during LESS.

NCAR provided 24 Portable Automated Mesonet (PAM II) remote surface weather stations for project LESS. These stations measured pressure, temperature, humidity, winds, and precipitation. The data from the stations were sent to NCAR real-time via the GOES satellite. The majority of the stations were positioned on the Michigan side of the lake. Fifteen stations out of the total had reliable data for temperature and winds, which could be used to supplement regular observations.

The Purdue and Chicago groups manned special rawinsonde stations during the experiment at MKG and NWI, providing routine daily upper air soundings at 0000 GMT and 1200 GMT. Supplemental soundings were also taken during CAO

periods. Additional rawinsonde information came from the US Army SNOW TWO field experiment at Camp Grayling, Michigan (CGR). These extra observations were added to the National Weather Service and Canadian Atmospheric Environment Service upper air data for analyses performed.

NCAR King Air and Queen Air research aircraft flew at multiple levels over Lake Michigan to collect 1Hz and 20Hz data (sample rates of one and 20 times per second). Under the direction of the Chicago research group, the planes flew 15 missions during project LESS. The data used in this thesis research came from NCAR flight mission # 85, the King Air and Queen Air research flights that took place during a cold air outbreak on 10 Jan 1984. Flight # 85 was unique in Project LESS in that the two planes made several east-west trips across the lake, recording data at five different levels in the boundary layer within a one hour and 48 minute period. Portions of the King and Queen Air data from this mission were used to construct vertical cross-sections for analysis of the convective boundary layer (CBL).

### 3.2 Data Analysis Methodology

Spectral decomposition of the aircraft data was used to analyze the mesoscale and microscale features of the CBL. In this method, a time series is transformed from real space to Fourier space by use of the International Mathematical and Statistical Library (IMSL) routines that do the fast Fourier transform. The data selected for decomposition met the following criteria:

- 1) the plane flew at a constant height or pressure level and a constant heading within the boundary layer,
- 2) the portion of the flight path selected contains an even number of observations, and
- 3) the flight path was long enough to provide statistically significant results.

All the meteorological measurements used in the spectral analysis were 20Hz data.

This helps to ensure that the third criterion is met. The 1Hz data were only used to calibrate the 20Hz specific humidity data (see Friehe, et al., 1986), and to verify the time-averaged mean states (discussed later).

Spectral representation makes it possible to remove the large scale circulation modes from a time series, allowing the intermediate scale modes of the data to be seen. These intermediate modes are not easily detectable by conventional methods. An atmospheric variable can be conceptualized as the sum of an infinite number of independent waves that can be represented as the sum of the scale components plus an error term:

$$\theta_{\text{TOTAL}} = \theta_{\text{SYNOPTIC}} + \theta_{\text{MESOSCALE}} + \theta_{\text{MICROSCALE}} + \theta_{\text{ERROR}}$$

where  $\theta_{\text{SYNOPTIC}}$  contains the macro  $\beta$  and meso  $\alpha$  scales which include features such as baroclinic waves;  $\theta_{\text{MESOSCALE}}$  includes the meso  $\beta$ , meso  $\gamma$  and micro  $\alpha$  scales that show organized convection;  $\theta_{\text{MICROSCALE}}$  contains the micro  $\beta$  and micro  $\gamma$  scales which represent the large eddies, thermals, and random small scale turbulence (see Orlanski, 1975). The error term indicates both random and systematic error. The spectral decomposition process has two separate parts. First, the synoptic scale signal must be removed from these data, leaving the mesoscale and microscale components of the data – a process called detrending. To do this, the IMSL routine RLFOTH was used to fit a second-order polynomial to the data and to determine the curvature and y-intercept. Once the curvature and y-intercept have been subtracted from the data, they are detrended. Removing the curvature removes the synoptic scale signal. When the y-intercept is removed, this eliminates the mean value of the data field plus any systematic error that might be present. Such errors could result from improper instrument calibration and/or inaccurate measurements. Any random errors in the data would remain.

After the data are detrended, the Fourier transformation can be done. The

IMSL fast Fourier routine FFTRC is used to transform the data by calculating the Fourier coefficients. Given N observations, FFTRC computes the first ( $N/2 + 1$ ) complex Fourier coefficients and their complex conjugates. The spectral energy densities are computed by multiplying each coefficient by its complex conjugate. Then the densities are normalized by dividing by N to yield results for the range of wavelengths from L to  $2L/N$ . (L is the length of the flight segment in meters.) The spectral density is lastly multiplied by the frequency, and can be plotted versus the log of the frequency and the wavelength. The equal areas under the curve of these plots will represent equal energy.

### 3.3 Instrument Specifications

The NCAR Beechcraft King Air and Queen Air aircraft are all metal, low-wing, pressurized monoplanes. These planes can measure up to 150 separate weather variables and plane information. The data are sampled at the rate of either once per second (1Hz) or 20 times per second (20Hz) . Table 3.1 gives specifications for the weather data used in this case study:

**Table 3.1** The instrument specifications for the weather data collected by the NCAR King Air and Queen Air research aircraft.

**NCAR KING AND QUEEN AIR INSTRUMENTATION (20Hz)**

VARIABLE MEASURED	SAMPLING DEVICE	RANGE	ACCURACY
Ambient Temperature	Rosemont 102E2AL	-60 to 40°C	±.5 C
Absolute Humidity	Lyman-alpha Hygrometer	.1 to 25 g/m	±5%
Cloud Liquid Water Content	Johnson-Williams LWH	0 to 5 g/m	-----
Horizontal Wind Component	Gust Probe and INS	0 to 100 m/s	±.1 m/s
Vertical Wind Component	Gust Probe and INS	-15 to 15 m/s	±.1 m/s

**NCAR KING AND QUEEN AIR INSTRUMENTATION (1Hz)**

VARIABLE MEASURED	SAMPLING DEVICE	RANGE	ACCURACY
Dewpoint Temperature	Thermoelectric Hygrometer	-50 to 50°C	± .5°C (>0°C) ±1.0°C (<0°C)
Cloud Droplet Spectrum	Laser Spectrometer (FSSP)	.5 to 45 μm	-----
Hydrometeor Spectrum	Laser Spectrometer (Y200)	300 to 4500 μm	-----
Latitude	Inertial Navigation System	+ 90	< 1.0 NM per flight hour
Longitude		+ 180	

\*NOTE: The NACA Pressure Altitude is not measured directly, but is the NACA standard height corresponding to the measured static pressure. The fluctuation error for temperature is 0.03 K (LeMone, 1976), and the fluctuation error for the three wind components is 0.1 m/s (Lenschow, 1973).

#### 4. MESOSCALE CTBL ANALYSES

##### 4.1 Flight # 85 Description

Flight Mission # 85, on 10 Jan 1984, was one of the fifteen research missions flown by the NCAR King Air and Queen Air research aircraft during Project LESS. This flight is the only one made during a cold air outbreak with northerly flow. The Purdue Mesoscale Convection Research Group was interested in this particular case because the flow had the longest fetch over the lake and allowed the greatest amount of air mass modification.

The King Air took off from MKG at 1558 GMT, and headed toward northwest Indiana on a flight route that formed a triangle over southern Lake Michigan, with the corners at MKG, Valparaiso Indiana (KNX), and MKE. The portion of the King Air flight data used in this case study comes from the latter portion of flight # 85, after the plane had reached MKE and turned east toward Michigan. The King Air then flew southeast a short distance to orient the plane, so the flight path would be perpendicular to the north-south cloud streets that had developed over the lake, and so that the heading would take the plane back to MKG. This portion of the flight ran along 43°N latitude and lasted from 1925 to 1949 GMT. The plane collected nearly five hours worth of data that day, with the flight ending at 2042 GMT.

The Queen Air also took off from MKG, at 1536 GMT. The plane headed south toward Indiana in order to fly a path similar to the King Air. Shortly after the Queen Air had turned south, instrument problems developed and the plane was forced to return to MKG at 1646 GMT. The problems were fixed and the Queen Air took off again at 1755 GMT. So much time had been lost that it was impossible to fly

the original scheduled triangular flight path over the lake. Instead, the Queen Air flew a series of four east-west legs (perpendicular to the cloud streets) at four different heights along 43°N latitude. All four of the Queen Air flight legs are included in this case study and lasted from 1812 to 2000 GMT.

The King Air and Queen Air data make up a unique data set; five separate vertical levels of boundary layer data that were collected in less than a two-hour time period. If a north-south steady-state is assumed for the two-hour observing period during the 10 Jan 84 cold air outbreak, it is possible to use these data to construct a quasi-simultaneous detailed vertical cross section of the convective boundary layer. Not all of the aircraft data collected could be used in the cross sections. The data selected had to meet the following criteria:

- 1) the plane must be at a nearly constant height within the boundary layer, and
- 2) the plane must fly along a constant latitude (43°N) and at a constant heading perpendicular to the cloud streets so that the flight data could be stacked vertically.

The following portions of the aircraft data satisfy the above criteria:

Level	Time (GMT)	Height	Heading	Length	Speed
5	19:25–19:49	1392m	west-east	109.8 km	75.9 m/s
4	19:35–20:00	1090m	west-east	111.6 km	71.7 m/s
3	19:07–19:32	800m	east-west	109.9 km	73.5 m/s
2	18:40–19:04	480m	west-east	102.4 km	72.0 m/s
1	18:12–18:37	210m	east-west	105.8 km	69.5 m/s

The heights are NACA pressure altitude, measured from mean sea level for a standard atmosphere. Lake Michigan is approximately 160m above sea level (see Fig 4.1).

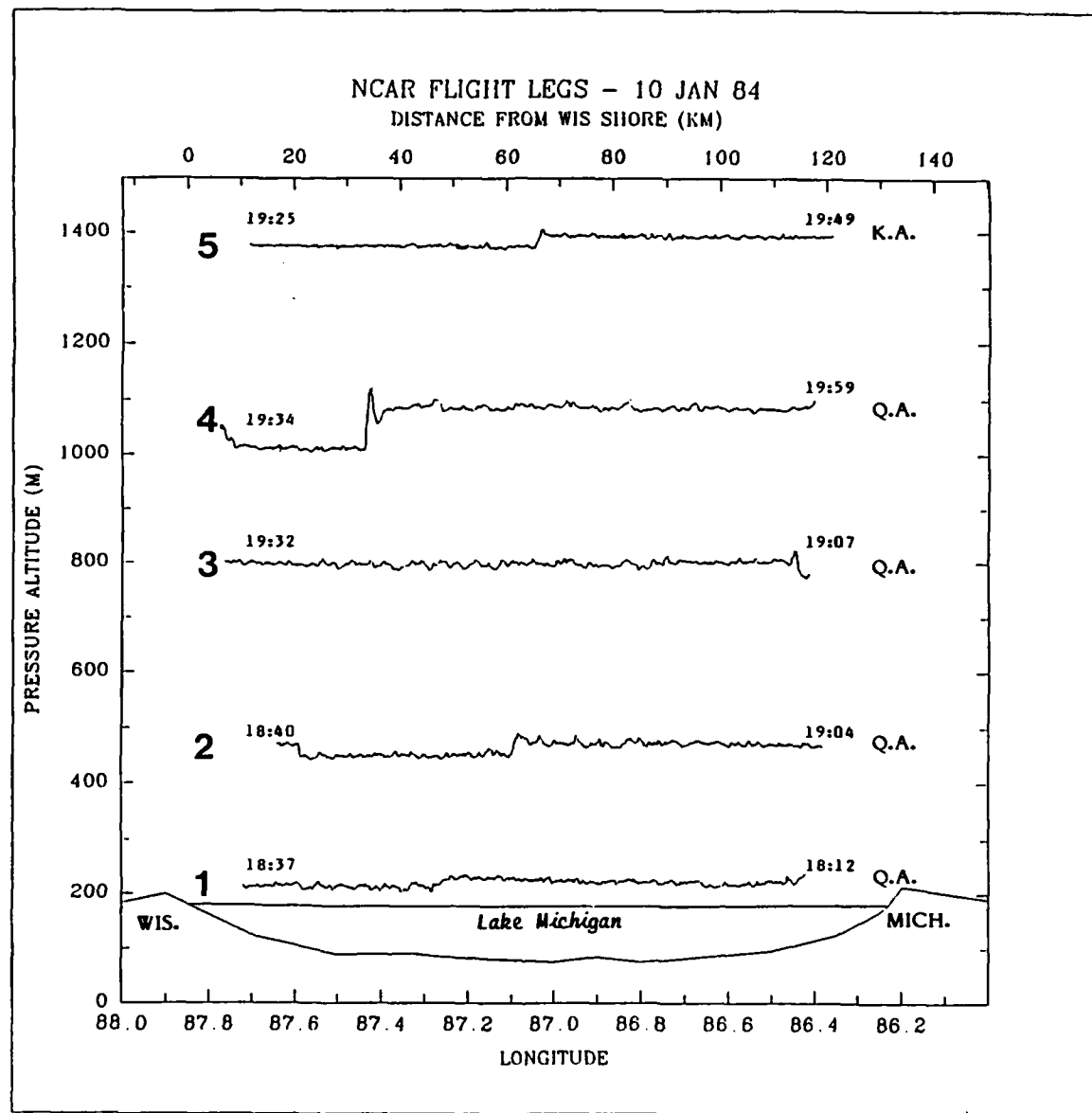


Figure 4.1 The five flight levels of the NCAR King Air and Queen Air from 1812 to 1959 GMT during the cold air outbreak of 10 January 1984.

## 4.2 Raw Data Plots

The meteorological measurements collected for this case study consist of the following 20Hz data: the three wind components (U, V, and W); temperature (T); virtual potential temperature ( $\theta_v$ ); and specific humidity (Q). The specific humidity is itself 1Hz data but by using it to calibrate 20Hz absolute humidity (Lyman-Alpha) fluctuations, one can obtain 20Hz specific humidity values (see Friehe, et al., 1986). Each data trace is plotted with respect to longitude and the aircraft's distance from the Wisconsin shoreline in kilometers. In order to simplify descriptions of the plots, the distance from Wisconsin (the top axis of each plot) is used to describe the location of features seen in each plot.

### 4.2.1 U Wind Component

The first data to be examined are the U wind component plots (Fig 4.2). In levels one and two the plots show the x-direction of wind predominantly from the west. Both levels show a definite direction change on the eastern side of the plots, at approximately 95 km (from Wisconsin). This easterly flow seems associated with a Michigan land breeze (discussed in section 4.33). Another direction change with a less pronounced area of easterly flow is found in the bottom level only, at about 22 km. This seems to indicate another (yet weaker) land breeze convergence zone, associated with forcing caused by the cP flow off the Wisconsin shore colliding with warmer air over the lake near the surface of the boundary layer. The third level has easterly flow predominating on the western side of the lake between 6 and 50km, with only occasional gusts from the west. The flow becomes more westerly in the western half of the plot (50–95km). The strongest westerly gusts occur between 90 and 95km, where the land breeze convergence zone is present. There is no abrupt direction change as in the levels below, but in the land breeze zone itself (90 to 115km) the winds become more easterly.

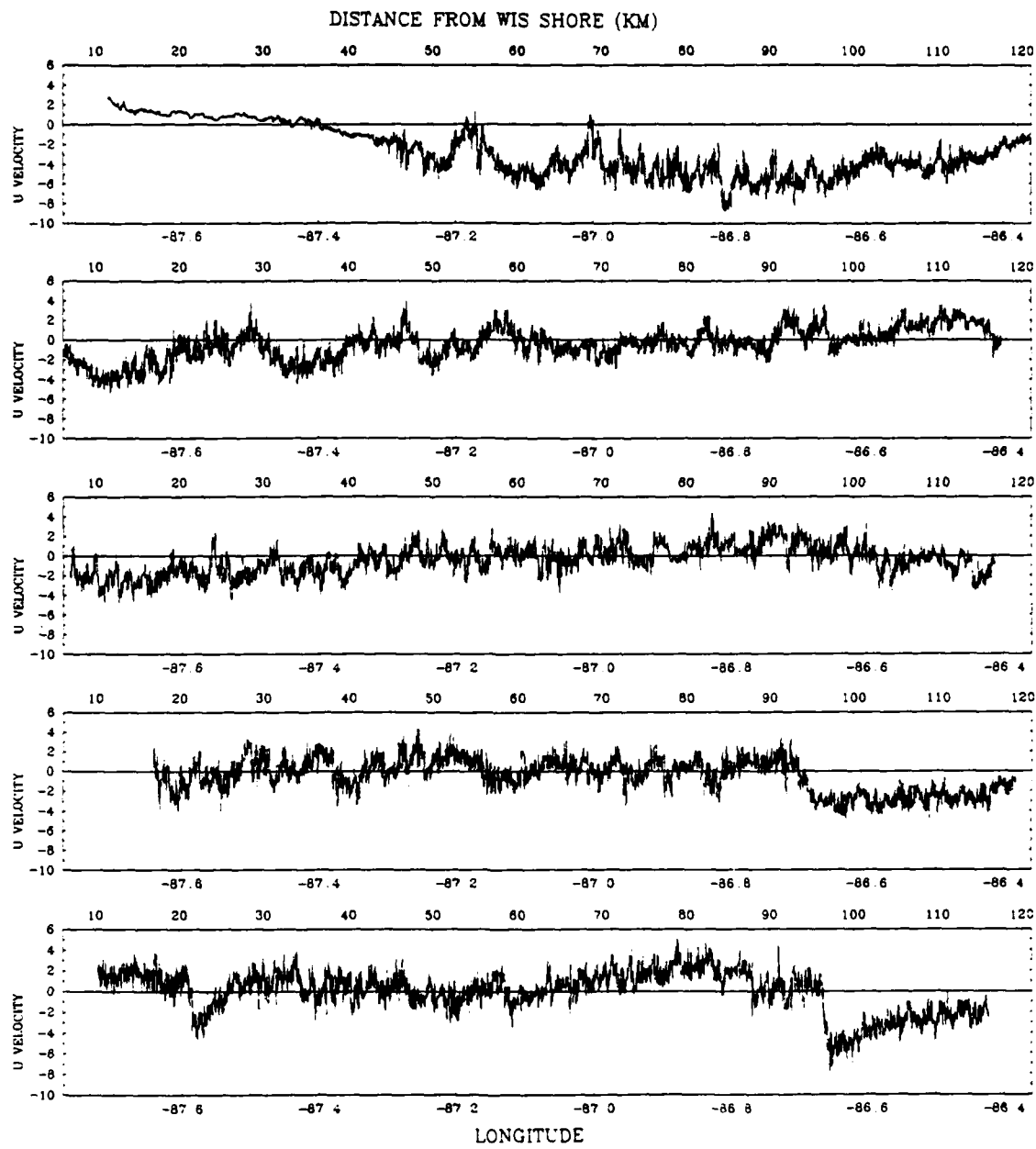


**Figure 4.2** Plots of raw aircraft u wind component measurements (m/s) for flight levels 1 through 5 on 10 January 1984.

The fourth level shows no direct signs of the land breeze. The winds at the western end of the plot are from the east, showing the strongest easterly flow of the level. Following the trace from west to east, the mean wind gradually changes direction from east to west. At the eastern end of the plot (90–115 km), the winds are predominantly from the west. This portion of the plot is in the region where the land breeze feature was seen in the lower levels and may be influenced by it. The most striking feature on level 4 is a regular wave pattern on the scale of 10's of kilometers. This can be seen most clearly in the western half of the trace. The top trace also shows part of the flight level outside the CTBL. There are weak westerlies and a minimum of turbulence at the western end of the plot showing that the aircraft is within the inversion layer (10–40km). The transition or interfacial layer (40–50km) can be seen to a certain extent in the shift of the u component of wind from west to east and in the increase in turbulence. The exact location of the transition zone is difficult to pinpoint here – the temperature and moisture plots do a better job. The CTBL (50–122km) is marked by strong easterlies and turbulence. The average easterly flow at this level is stronger here than in the lower levels. The strongest easterlies begin at 60 km, and continue to 100 km (where the Michigan land breeze front would be if it reached to this level). Beyond 100 km the easterlies gradually weaken and the mean wind begins to decrease in strength. All the levels show some indication of waves embedded in the flow (on the scale of 10's of km), with level four having the most obvious fluctuations (perhaps because that level has the longest horizontal stretch of boundary layer undisturbed by land breezes or inversions).

#### **4.2.2 V and W Wind Components**

The V wind component (Fig 4.3) shows a strong northerly flow (4–10 m/s) at all levels. The strongest average winds are at the lowest levels, near the CTBL surface. The third and fourth levels have the weakest average winds (1–2 m/s slower). The

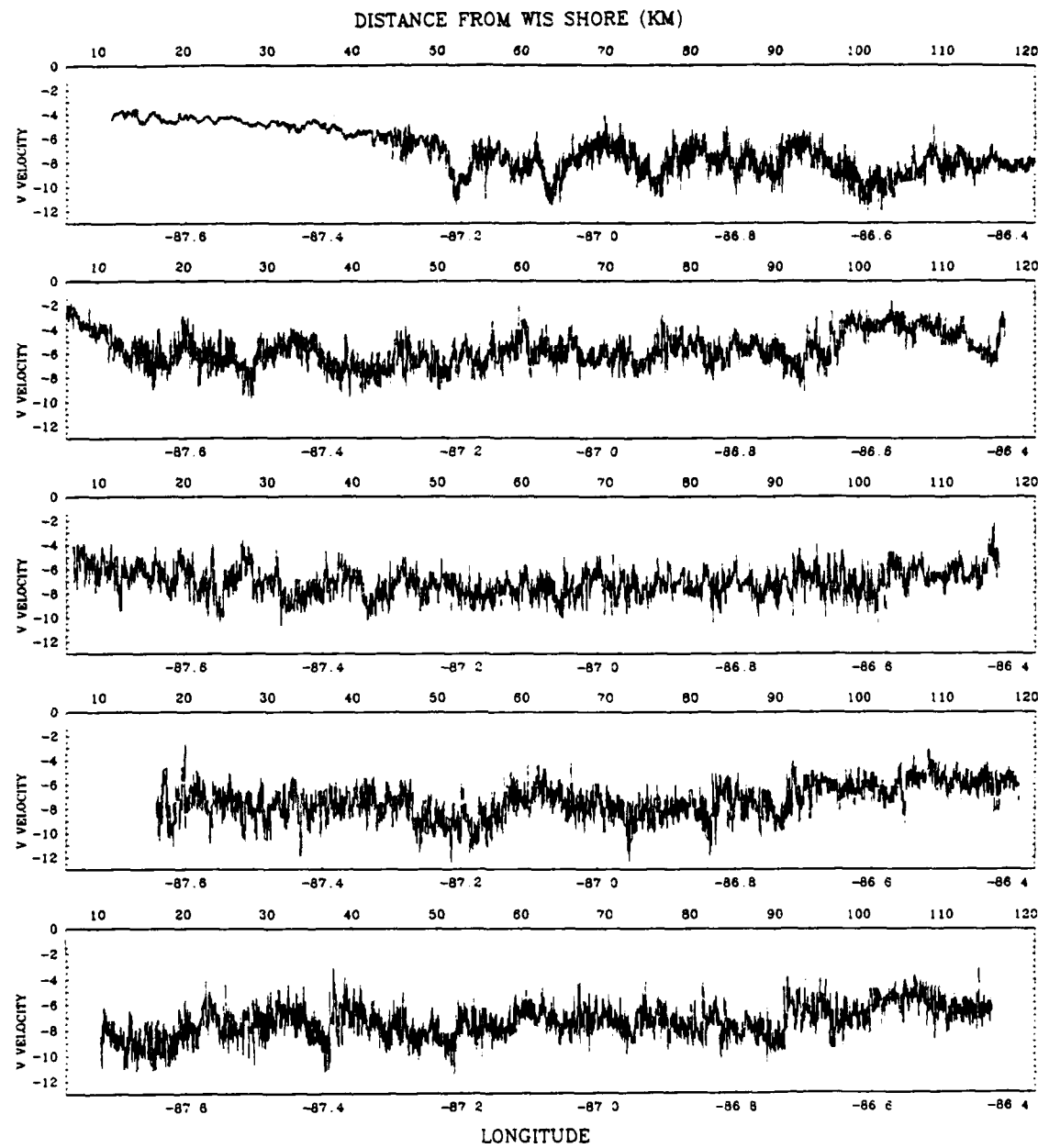


Figure 4.3 Plots of raw aircraft v wind component measurements (m/s) for flight levels 1 through 5 on 10 January 1984.

fourth level shows some evidence that the extreme western end of the trace is outside the CTBL (6–15km), with the wind speed decreasing markedly. The top level also shows weaker northerly flow with much less turbulence at the west end of the plot (10–40km). The change from the boundary layer to the inversion layer is quite clear, but the change from the boundary layer to transition layer is not as obvious. There is only weak evidence of a land breeze at any of the levels. There are also smaller scale waves (10's of km scale) embedded in the flow as in the u-component. The most regular pattern of waves can be seen in the top level between 50 and 100 km. With a strong and persistent northerly flow, it seems reasonable to assume a north-south steady-state condition for the two hour period covered by the data analyzed. This assumption makes it possible to 'stack' the levels and make cross-sections of the boundary layer (to be presented later in this chapter).

All five levels show large fluctuations in the W component of velocity (approximately 3–4 m/s) in the CTBL (Fig 4.4). In the top level the vertical velocity fluctuations decrease in the inversion layer (10–40km) to approximately .5 m/s. The average velocity becomes weakly negative, indicating subsidence. The lowest flight levels show the most turbulent fluctuations and the greatest change in speed between positive and negative values. The horizontal distance between speed maxima and minima increases in the upper levels (which seems to indicate that the size of turbulent eddies increases with height in the CTBL). Levels 3 and 4 show some evidence of the mesoscale wave feature seen in the U and V components (10's of km scale). There is too much turbulent noise in the lowest two levels to distinguish any mesoscale features.

#### 4.2.3 Temperature Data

The temperature ( $T$ ) and virtual potential temperature ( $\theta_v$ ) have the same mesoscale trends. The inverse correlation between temperature and humidity cause differences in the microscale fluctuations between  $T$  and  $\theta_v$ , with the  $\theta_v$  fluctuations

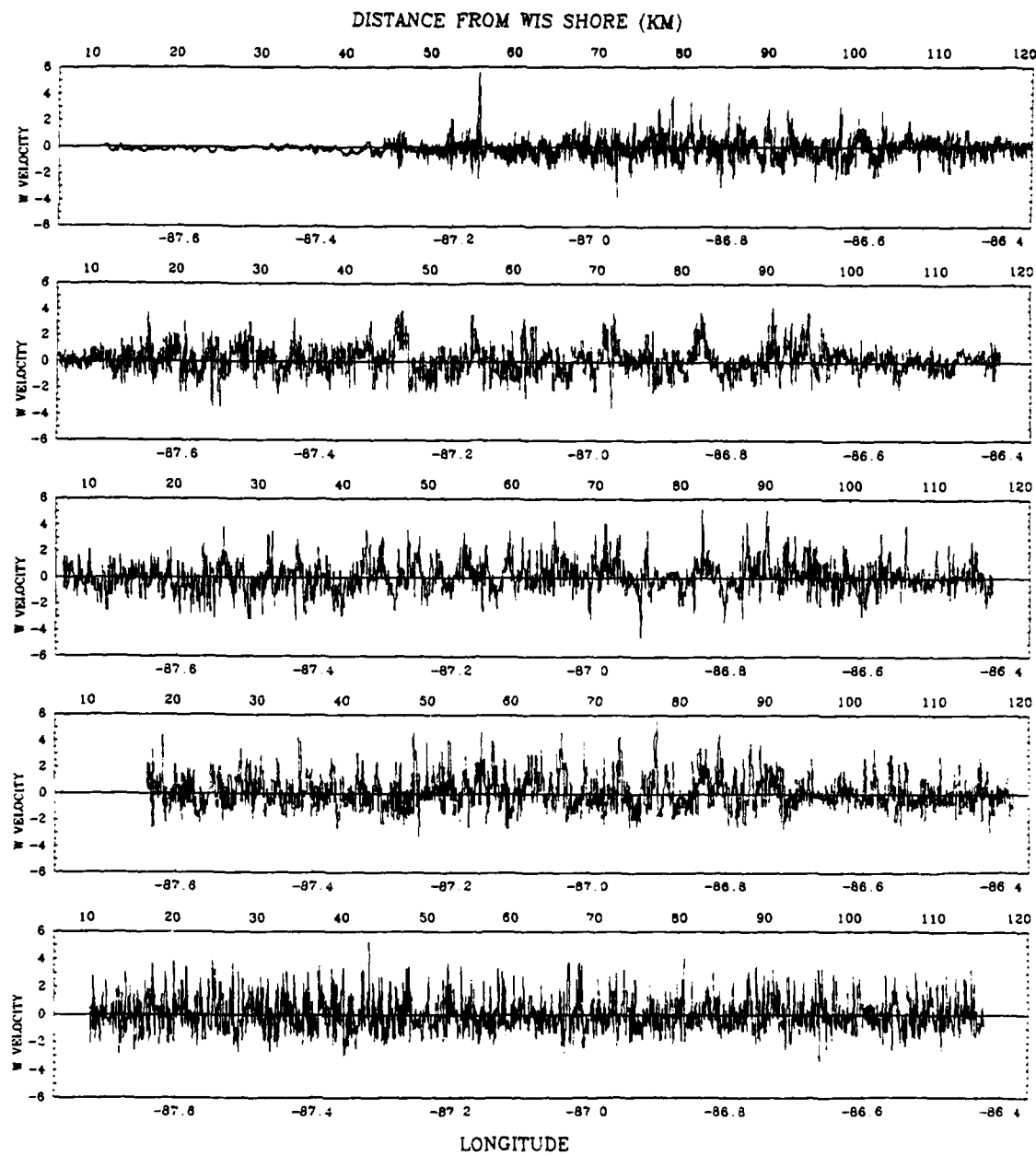
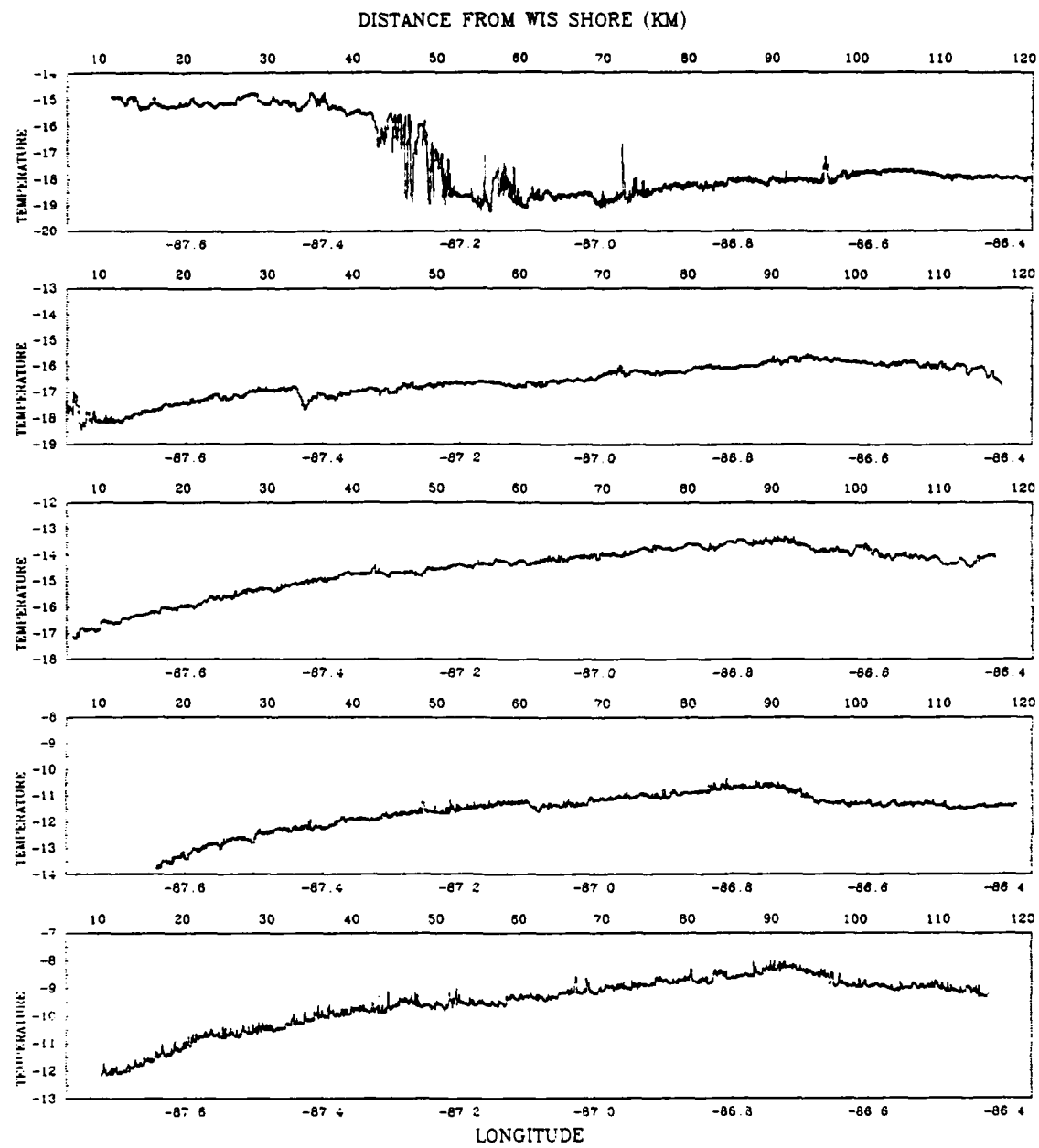


Figure 4.4 Plots of raw aircraft w wind component measurements (m/s) for flight levels 1 through 5 on 10 January 1984.

damped by the humidity. For the purpose of this mesoscale analysis, the temperature data (Fig 4.5) will be discussed. Both temperature and  $\theta_v$  will be examined in the section on spectral analysis and microscale fluctuations. The bottom three levels show a strong mesoscale trend, with the coldest temperatures on the western side of the plot (with 2–4°C horizontal difference). This relatively small horizontal temperature gradient shows the result of the strong northerly flow. The flow is almost parallel to the main axis of Lake Michigan, and the difference in fetch between the west and east sides of the lake is small. The flow has also spent a sufficient amount of time over the lake already to be significantly modified to allow convection over the entire east–west traverse covered by the aircraft data. The maximum temperatures are not at the extreme eastern end of the plots (nearest the shoreline), but are found near the area of the Michigan land breeze convergence zone (90–95km). The temperatures within the land breeze area (95–115km) are about 1–2°C cooler than the maximum temperatures found just west of the convergence zone. The fourth level has a large-scale trend similar to that in the bottom three levels, except for a small (1°C) temperature increase and an increase in turbulent fluctuations at the extreme western end of the level where the aircraft data values were recorded in the transition layer (6–15km) found between the CTBL and the inversion. The temperature maximum associated with the Michigan land breeze convergence band has disappeared at this level.

The temperature trace for the top level is very different from the levels underneath. The warmest temperatures at this level are found in the inversion layer (6–40km), where the temperatures warm up 3 – 4°C over the coldest CTBL temperatures. The transition layer (40–60km) is plainly marked by 4 – 5°C fluctuations in temperature, and a decrease in the mean temperature by 2 – 3 °C. The coldest temperatures occur in the middle section of this level (at approximately



**Figure 4.5** Plots of raw aircraft ambient temperature measurements ( $^{\circ}\text{C}$ ) for flight levels 1 through 5 on 10 January 1984.

60km), where the aircraft left the transition layer and entered the convective boundary layer. The coldest temperatures are found just east of this point at 60–75 km.

#### 4.2.4 Specific Humidity Data

The final plots to be examined are for Q (Fig 4.6). The bottom three flight levels show strong turbulent fluctuations, as well as the same type of waves seen in the wind data (at 10's km length scale). The locations of these local humidity maxima would seem to indicate areas where convective precipitation is falling, and correspond with the areas of precipitation observed by the scientists in the aircraft and recorded in the flight log. The single largest maximum size and intensity is on the Michigan side of the lake (at 95–105km), in the area of the land breeze convergence zone. The humidity values decrease somewhat further east (by .3-.4 g/kg) within the region of the Michigan land breeze (105–115km). Other significant moisture bands are located at approximately 80km, 60km, 40km, and 20km. The moisture band found between 50 and 60km is the most pronounced next to the land breeze frontal band. The 20km moisture band corresponds to the precipitation associated with the weaker Wisconsin land breeze convergence zone. Despite the turbulent fluctuations, the average humidity of the three levels is high – 1.2 to 1.6 g/kg. It is interesting to note that in the third level the amount of turbulent moisture fluctuations decreases at the western end of the trace (6–35km). This may be an indication that the western end of the third flight level is within the base of the clouds.

The fourth level has fluctuations that are less turbulent than the levels below, showing that this level, too may be within the clouds. The average humidity for most of the level remains high (1.2 g/kg), but decreases dramatically to .5 g/kg at the extreme western end of the level (6–15km) where the data were recorded within the transition layer. The lack of strong mesoscale peaks ( 10km) in a at this level, indicative of precipitation bands, is further evidence that this level is within (and not

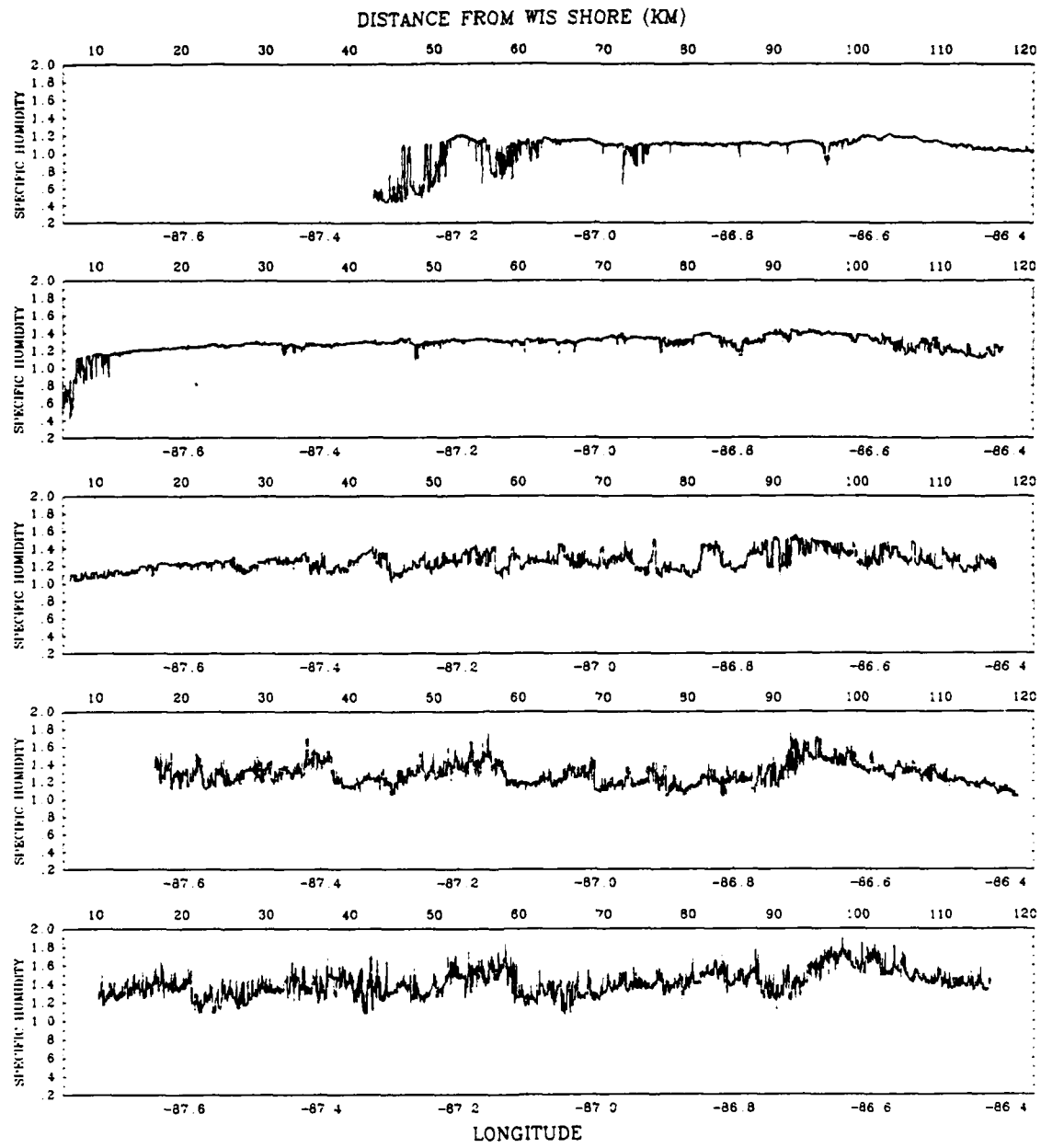


**Figure 4.6** Plots of raw aircraft specific humidity measurements (g/kg) for flight levels 1 through 5 on 10 January 1984.

below) the cloud deck. The top level also has a relatively smooth trace in the portion of the level within the CTBL (60–120km), as well as a fairly high average humidity (1 g/kg). The wide fluctuations of the humidity trace (.5–.6 g/kg) between 40 and 60km shows the location of the transition layer clearly. In the highly stable and dry inversion layer the humidity fluctuations vanish and the Lyman–Alpha trace becomes zero. The 1Hz specific humidity trace (not shown) decreases to a baseline value of .18 g/kg.

#### 4.3 CTBL Features

It is appropriate at this point to summarize the main features that were present in the CTBL, before going on to the details of the CTBL cross-sectional analysis. The first feature that can be seen is the change in the height of the CTBL. The data traces of level 5 for all variables show that the top of the CTBL on the western side of the lake is below that flight level. The difference in fetch between the east and west sides of the lake allows different amounts of air mass modification and different thicknesses in the CTBL. The inversion is strongly evident and is characterized by weak subsidence, a lack of turbulence in the winds, and relatively warm and dry air along the western end of the plots.

The Michigan land breeze feature is also strongly evident in the U-component data at the bottom two levels, with some indirect support found in the temperature and moisture data. The land breeze is made up of a relatively dry, cold flow off the Michigan coast. A band of strong convergence and precipitation over the lake is also associated with the Michigan land breeze front. The strength of this front is seen in the temperature and specific humidity data. There is also a shallow land breeze effect caused by convergence along the Wisconsin shore. This can be seen in the U-component data at the bottom level. There is weak support for this convergence band in the humidity data, but the land breeze front is too weak to show up in the

temperature data. In the following sections the characteristics of both land breezes will be discussed in detail. The bottom two levels of the specific humidity data also show an enhanced convective band at mid-lake, between 50 and 60km.

Data traces in general, except temperature and the W-component of wind, show clear evidence of mesoscale (10's of km) waves in the CTBL. The turbulent noise in the vertical velocity data masks any larger scale features, and in the temperature data the large scale trend is too strong to allow the smaller scale waves to be seen. (Detrended data will be analyzed in a later section.) The next step in the research analysis was to construct mesoscale cross-sections of the CTBL to see if the features mentioned above could be identified more clearly.

#### **4.3.1 Cross-section Methodology**

The vertical cross sections of the CTBL were created using the NCAR graphics package CONRAN (CONtour RANDom data), which is designed to contour randomly-spaced data fields on an x,y plane. The longitude and the NACA pressure altitude (the height above sea level for a standard atmosphere) were used as the x and y gridpoints, respectively. These aircraft variables are sampled at 1Hz frequency. In order for CONRAN to have a single data value for each x,y location, the 20Hz data had to be averaged over each second. It was also necessary to occasionally average the data over 2-4 seconds to eliminate redundant x,y points. In the worst case (4 second averaging), the smallest length scale possible in the horizontal is approx 300m (based on an average plane speed of 75m/s). In order to 'stack' the multiple levels of observations made over a two hour time period, a north-south steady state is assumed (i.e. the atmospheric conditions along the axis of the mean wind flow, and the properties of the rolls, change very little during the observational time). In the case of the vertical velocity profile, the values contoured are the mean values averaged over 5

km sections of the CTBL. This allows the mean statistics of the mesoscale CTBL features to be seen.

#### 4.3.2 Vertical PBL Cross-section

Figure 4.7 shows three cross-sections of the PBL constructed from the aircraft data for the U wind component, virtual potential temperature ( $\theta_v$ ), and specific humidity (Q). In looking at the portion of the CTBL included in this area, several features are evident. First, the overall structure of the CTBL can be seen most clearly in those variables that are associated with moisture ( $\theta_v$  and Q). Both of these cross-sections (Figs 4.7.2 and 4.7.3) show a well-mixed CTBL that gradually increases in depth from west to east across the lake. Agee and Gilbert (1989) discovered that the maximum depth of the CTBL was 2000m over the eastern third of the lake. The CTBL depth over the western end of the lake is shown here to be approximately 900m. This relatively deep CTBL along the western shore of the lake shows that the air moving down from the north-northwest over Lake Michigan has already been partially modified by Lake Superior, and that the long fetch over Lake Michigan has further modified the air over the entire east-west slice of the lake. The isopleths and high humidity values in the CTBL show that a good deal of heat and moisture have already been absorbed by the atmosphere. There is enough of a difference in fetch across the lake, however, to cause a horizontal  $\theta_v$  gradient over the length of the cross-section. As the depth of the CTBL increases from west to east, the  $\theta_v$  values also increase.

This makes the contrast between the CTBL and the inversion layer above very apparent in the western half of the cross-sections. Strong vertical gradients in  $\theta_v$  and Q clearly mark the stable inversion. The inversion can also be seen in the U-component cross-section as an area of weak westerly flow (Fig 4.7.1). The U-component cross-section also shows a CTBL with north-northwest flow in the

Figure 4.7 Vertical cross-sections for u wind component (m/s - top), virtual potential temperature ( $^{\circ}\text{K}$  - middle), and specific humidity (g/kg - bottom), based on the five research aircraft flight levels over Lake Michigan on 10 January 1984. The contour intervals are 1 m/s (top),  $.2^{\circ}\text{K}$  (middle), and .05 g/kg (bottom).

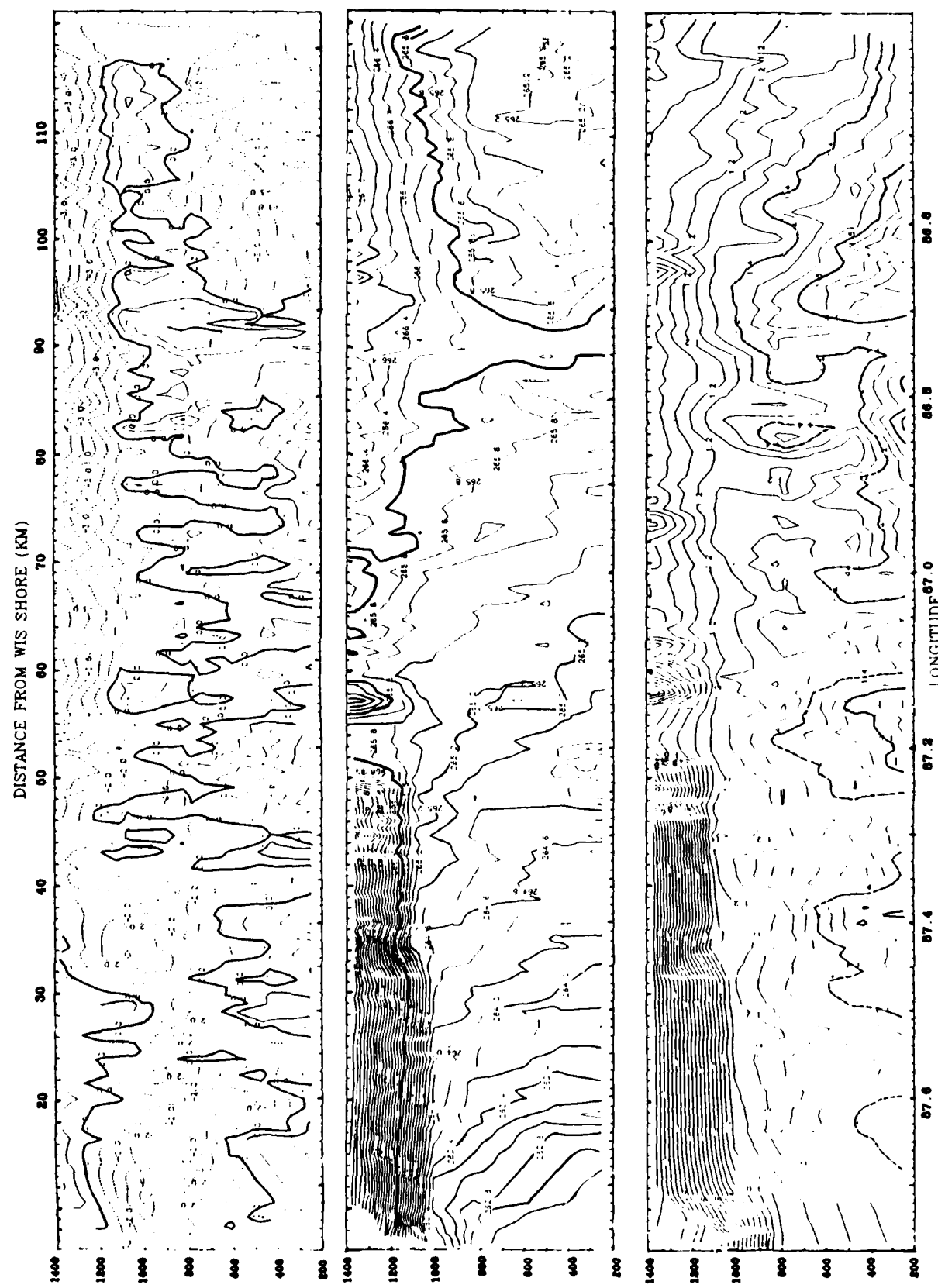


Figure 4.7

lower levels and north-northeast return flow above. The exception to this lies at the eastern end of the cross-section, where a land breeze has developed.

#### 4.3.3 Michigan Land Breeze

The land breeze feature is the most obvious in the U-component profile. An area of strong east winds in the lower half of the CTBL can be seen between 92 and 120km (Fig 4.7.1). There is also evidence in the  $\theta_v$  data that this region is under the influence of somewhat colder air flowing westward from lower Michigan (Fig 4.7.2). Within the area covered by the land breeze, the horizontal  $\theta_v$  gradient is reversed. Here, the  $\theta_v$  gradient decreases slightly from west to east (about  $1^{\circ}\text{C}$ ).

Three criteria given by Lyons (1972) are useful in determining if this is a true land breeze phenomenon. First, the northeast flow seen here must not be associated with any synoptic scale weather system. The synoptic maps in Chapter 2 show (Fig 2.3) that the mean flow is north-northwest, so this requirement is met. Second, there must be a return flow associated with the land breeze. We see a band of west winds in the mid-level CTBL, which is in opposition to the mean northeast CTBL return flow. Third, the land breeze must generate a convergence 'front' at the point where the land breeze meets the mean flow. This convergence front can be seen in the U-component profile between 88 and 94km. The  $\theta_v$  cross-section also clearly shows that this front is a strong source of heat transport. The Q profile further shows the influence of this front, with a large area of moisture extending up into the CTBL (Fig 4.7.3). The moisture band is too widespread to show the exact location of the front. The wind and  $\theta_v$  cross-sections give the location more precisely.

This land breeze feature is a cold air gravitating outflow from lower Michigan. Such a gravity current is known to possess stably stratified oscillating gravity waves. These stable damped waves are evident in the vertical velocity cross section (Fig 4.8) to the east of the land breeze boundary and have a wavelength of about 10 km.

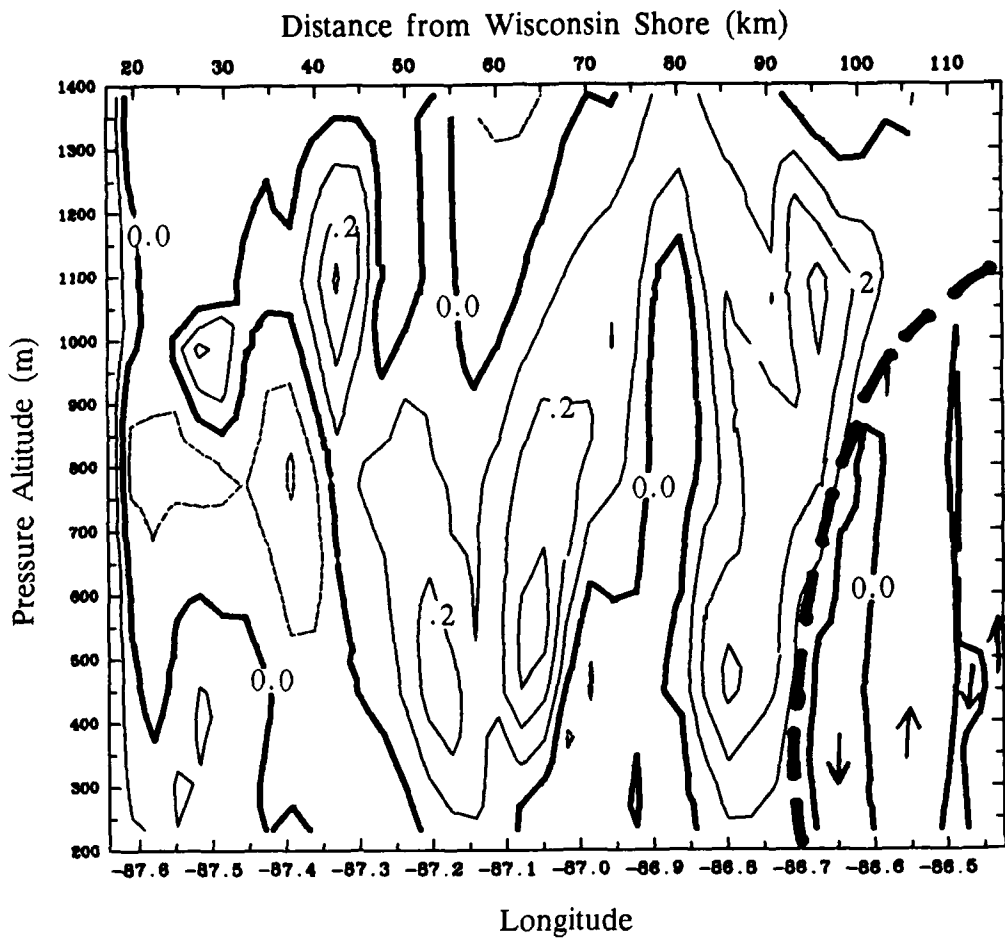


**Figure 4.8** Cross-section of vertical velocity (m/s – 5km averages). Note the cold air gravitating outflow from lower Michigan, to the east of the land breeze convergence band, with evidence of stably stratified oscillating gravity waves ( $\lambda$  about 10km). The contour intervals are .1 m/s.

#### 4.3.4 Weak Wisconsin Land Breeze

The local land breeze effect seen in the U-component data plots (Fig 4.7.1) can also be seen in the cross-section between 6 and 22km. There is a shallow layer of north-northwest flow in the lower third of the CTBL, that becomes north-northeast between 22 and 28km. But according to the land breeze criteria mentioned above, this is not a true land breeze. There is a band of convergence similar to a front found in the specific humidity cross-section (Fig 4.7.3) and to a small extent in the  $\theta_v$  data

(Fig 4.7.2). But the 'land breeze' feature turns out to be part of the mesoscale north-northwest surface flow across the lake. The return flow found above it also coincides with mean return flow of the CTBL. Rather than being a true land breeze, the wind-shift and moisture found at 22km seems to be the first of the many 2-D mesoscale convective bands embedded in the Type I CTBL over Lake Michigan.

#### 4.3.5 Michigan Snow Band

One of the effects of the strong Michigan land breeze is a strong band of convergence along the line where the two opposing wind flows collide. This band (Fig 4.7) is found between 86 and 96km and is marked by a strong wind speed gradient (from  $-3$  m/s at 96km to  $+1$  m/s at 86km), a band of upward vertical velocity (Fig 4.8), a band of the warmest virtual potential temperatures ( $266^{\circ}\text{K}$ ) in the lower CTBL, and a broad area that includes the highest moisture values in the CTBL (1.6 g/kg). These high levels of heat and moisture are evidence that the convergence caused by the land breeze is driving a powerful band of convection. The effects of this single band dominate the eastern half of this CTBL cross-section. The maximum amount of precipitation and the largest single cloud street are associated with this snow band (see the satellite image in Fig 2.1). This snow band marks the effective eastern boundary of convection in the CTBL, since to the east of this band is the land breeze region where convection is suppressed by the more stable outflow from Michigan. In effect, the off-shore flow from both the east and west sides of the lake imposes lateral boundary conditions on the CTBL and limit the area where a more natural mixed convective layer can be found.

#### 4.3.6 Mid-Lake Snow Band

The vertical velocity profile (Fig 4.8) shows the presence of a large band of upward motion, caused by convergence, between 50 and 60 km. The specific

humidity and virtual potential temperature cross-sections (Fig 4.7) also show evidence of this band, which can be identified by local maxima found at the surface of the CTBL. The U-component data also marks the location of this band with a wind-shift line. Braham and Kelly (1982) noted that in a northerly flow event, the narrowness of the lake limits the number of cloud streets that can develop with a tendency to favor the development of a convective band in the middle of the lake. This band is the next largest convective band seen in the present CTBL analysis, after the convective band associated with the land breeze convergence front. As the CAO and the convective roll vortices weaken over time, this convective band is unmasked and becomes the main feature remaining in the CTBL. This mid-lake band is the last feature lingering at the end of the CAO. The movement of the surface high pressure system eastward to the eastern Great Lakes region caused the synoptic scale flow to become easterly, which slowly pushed the mid-lake convective band west toward the Wisconsin shore before it dissipated.

#### 4.3.7 Microscale Convective Features

In the aircraft data plots of the five levels in the PBL, there were indications that some sort of mesoscale and microscale structures were present. In all of the cross-sections (Fig 4.7), there is evidence of these structures with a wavelength of approximately 20km near the CTBL surface. The specific humidity data show three of these structures in the western half of the cross-section (at 17, 38, and 56km). The Michigan snow band in the eastern half of the cross-section is so strong that it prevents these structures from appearing. The U-component cross-section also shows three definite wind-shift lines where surface convergence results (at 20, 40, and 60km). There is an indication of another wind-shift at 78km, but due to the strength of the snow band at 92km, this line of convergence never reaches the surface of the CTBL. The  $\theta_v$  cross-section shows the least evidence for these structures, but even here weak

local temperature maxima (at 18 and 50km) also exist.

It is impossible to determine exactly what these structures are, even with the detailed aircraft data available. It is equally possible that the structures in the cross-sections are made by actual 2-D cloud streets observed over the lake, or that they are made up of a coalescence of several 2-D cloud streets. While the actual sizes and locations of the streets over the lake are somewhat unknown, the actual nature of embedded smaller microscale structures appear even more difficult to determine. In the next section, spectral analyses of the data will be examined to see if these structures can be better resolved.

#### 4.4 Spectral Decomposition

In order to obtain the most meaningful results from the spectral analysis, the aircraft data used should come from a homogenous sample of the CTBL. Figure 4.9 shows the portion of each flight level selected in order to exclude any influence from the land breeze or inversion layer on the spectral decomposition results. The spectral plots will show the structure of the well-mixed CTBL. The length of each flight level and the speed of the aircraft vary, so the size of the maximum wavelength ( $L_x$ ) also varies between the flight levels. It is important to note here that the depth of the CTBL increases from west to east across each flight level. The portions of the top two levels used cover the eastern half of the CTBL, where the mean inversion height ( $Z_i$ ) is approximately 1.9 km above the lake. The bottom three levels include the western half of the CTBL, where the depth of the CTBL increases most rapidly.  $Z_i$  for these levels is 1.36 km above the lake. When interpreting the spectral data, it is necessary to take into account the difference in CTBL depth between the top two levels and the three levels beneath. The minimum resolvable wavelength ( $L_x$ )<sub>min</sub> for each level can be calculated as follows:

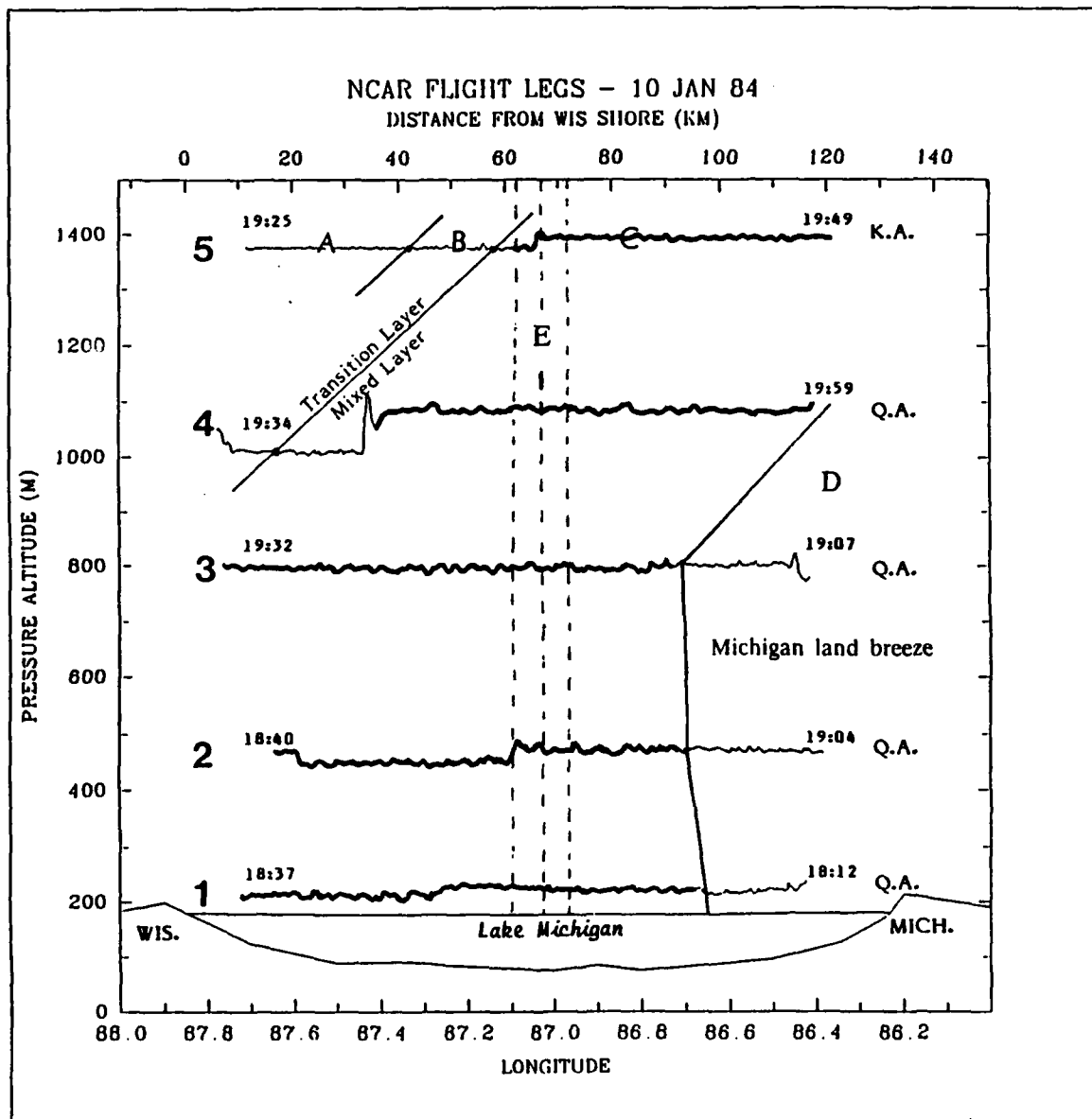


**Figure 4.9** The five flight levels of the NCAR King Air and Queen Air aircraft, indicating the location of the inversion layer (A), the transition layer (B), the well-mixed boundary layer (C), and the Michigan land breeze (D). Area (E) is the representative subsection of the CTBL (between 61 and 71km) used when calculating the covariances. The portions of the aircraft data within area C were used in the spectral analysis.

$$(Lx)_{\min} = \frac{2 * \text{aircraft speed}}{\text{collection rate}} \quad (4.1)$$

The aircraft speed for each level was given in section 4.1. The data collection rate is 20Hz. The minimum wavelength varies between 6.95 and 7.59 meters, for aircraft speeds varying between 69.5 and 75.9 m/s. Table 4.1 shows the wavelengths associated with the first 30 wave numbers for each flight level.

Before any spectral decomposition can be done, the data must be detrended (as discussed in section 3.2). A second-degree polynomial was fitted to the data that make up the selected portions of the CTBL in order to remove the synoptic scale trends. The spectral energy values were normalized, multiplied by their frequencies, and plotted against the log of the frequency and wavelength. This ensures that equal areas under the curve represent equal energy. This technique was employed by Ross and Agee (1985) on AMTEX data, and Agee and Gilbert (1989) on Project LESS data. When interpreting spectral data, the following limitations must be kept in mind. There is a large difference in the wavelength size at the smaller wave numbers (see table 4.1). All the energy at this end of the scale is represented at those particular wavelengths. For example, at Level 1 the wavelengths associated with the first two wave numbers are 81.0 and 40.5km, respectively. Any intermediate-sized wavelengths would not be properly represented in the analysis. The second limitation is the method used in detrending. When fitting the polynomial to the data, the correlation between the curve and the actual data needs to be closely examined to make sure that no artificial signals are added to the spectra by a poor curve-fit. Lastly, statistical theory states that energy peaks seen for wave numbers less than 10 would not be statistically significant (due to insufficient sampling). In order to minimize this problem, the aircraft data were scrutinized carefully in order to select a portion of the CTBL where the sample environment was well-known. This makes it

**Table 4.1** The first 30 wave numbers (k) represented in the spectra of the aircraft data and their associated frequencies (f) and wavelengths (L<sub>x</sub>).

	<b>Level 1</b>		<b>Level 2</b>		<b>Level 3</b>		<b>Level 4</b>		<b>Level 5</b>	
k	L <sub>x</sub>	f								
1	81.0	$8.5 \times 10^{-4}$	73.8	$9.67 \times 10^{-4}$	87.6	$8.36 \times 10^{-4}$	84.1	$8.50 \times 10^{-4}$	60.1	$1.24 \times 10^{-3}$
2	40.5	$1.7 \times 10^{-3}$	36.9	$1.93 \times 10^{-3}$	43.8	$1.67 \times 10^{-3}$	42.1	$1.70 \times 10^{-3}$	30.1	$2.49 \times 10^{-3}$
3	27.0	$2.6 \times 10^{-3}$	24.6	$2.90 \times 10^{-3}$	29.2	$2.51 \times 10^{-3}$	28.0	$2.55 \times 10^{-3}$	20.0	$3.73 \times 10^{-3}$
4	20.3	$3.4 \times 10^{-3}$	18.5	$3.87 \times 10^{-3}$	21.9	$3.34 \times 10^{-3}$	21.0	$3.40 \times 10^{-3}$	15.0	$4.98 \times 10^{-3}$
5	16.2	$4.3 \times 10^{-3}$	14.8	$4.84 \times 10^{-3}$	17.5	$4.18 \times 10^{-3}$	16.8	$4.25 \times 10^{-3}$	12.0	$6.22 \times 10^{-3}$
6	13.5	$5.1 \times 10^{-3}$	12.3	$5.80 \times 10^{-3}$	14.6	$5.02 \times 10^{-3}$	14.0	$5.10 \times 10^{-3}$	10.0	$7.46 \times 10^{-3}$
7	11.6	$6.0 \times 10^{-3}$	10.5	$6.77 \times 10^{-3}$	12.5	$5.85 \times 10^{-3}$	12.0	$5.95 \times 10^{-3}$	8.6	$8.71 \times 10^{-3}$
8	10.1	$6.8 \times 10^{-3}$	9.2	$7.74 \times 10^{-3}$	11.0	$6.69 \times 10^{-3}$	10.5	$6.80 \times 10^{-3}$	7.5	$9.95 \times 10^{-3}$
9	9.0	$7.7 \times 10^{-3}$	8.2	$8.70 \times 10^{-3}$	9.7	$7.53 \times 10^{-3}$	9.3	$7.65 \times 10^{-3}$	6.7	$1.12 \times 10^{-2}$
10	8.1	$8.5 \times 10^{-3}$	7.4	$9.67 \times 10^{-3}$	8.8	$8.36 \times 10^{-3}$	8.4	$8.50 \times 10^{-3}$	6.0	$1.24 \times 10^{-2}$
11	7.4	$9.4 \times 10^{-3}$	6.7	$1.06 \times 10^{-2}$	8.0	$9.20 \times 10^{-3}$	7.7	$9.35 \times 10^{-3}$	5.5	$1.37 \times 10^{-2}$
12	6.8	$1.0 \times 10^{-2}$	6.2	$1.16 \times 10^{-2}$	7.3	$1.00 \times 10^{-2}$	7.0	$1.02 \times 10^{-2}$	5.0	$1.49 \times 10^{-2}$
13	6.2	$1.1 \times 10^{-2}$	5.7	$1.26 \times 10^{-2}$	6.7	$1.09 \times 10^{-2}$	6.5	$1.11 \times 10^{-2}$	4.6	$1.62 \times 10^{-2}$
14	5.8	$1.2 \times 10^{-2}$	5.3	$1.35 \times 10^{-2}$	6.3	$1.27 \times 10^{-2}$	6.0	$1.29 \times 10^{-2}$	4.3	$1.74 \times 10^{-2}$
15	5.4	$1.3 \times 10^{-2}$	4.9	$1.45 \times 10^{-2}$	5.8	$1.25 \times 10^{-2}$	5.6	$1.28 \times 10^{-2}$	4.0	$1.87 \times 10^{-2}$
16	5.1	$1.4 \times 10^{-2}$	4.6	$1.55 \times 10^{-2}$	5.5	$1.34 \times 10^{-2}$	5.3	$1.36 \times 10^{-2}$	3.8	$1.99 \times 10^{-2}$
17	4.8	$1.45 \times 10^{-2}$	4.3	$1.64 \times 10^{-2}$	5.2	$1.42 \times 10^{-2}$	4.9	$1.45 \times 10^{-2}$	3.5	$2.11 \times 10^{-2}$
18	4.5	$1.53 \times 10^{-2}$	4.1	$1.74 \times 10^{-2}$	4.9	$1.51 \times 10^{-2}$	4.7	$1.53 \times 10^{-2}$	3.3	$2.24 \times 10^{-2}$
19	4.3	$1.62 \times 10^{-2}$	3.9	$1.84 \times 10^{-2}$	4.6	$1.59 \times 10^{-2}$	4.4	$1.62 \times 10^{-2}$	3.2	$2.36 \times 10^{-2}$
20	4.1	$1.71 \times 10^{-2}$	3.7	$1.93 \times 10^{-2}$	4.4	$1.67 \times 10^{-2}$	4.2	$1.70 \times 10^{-2}$	3.0	$2.49 \times 10^{-2}$
21	3.9	$1.79 \times 10^{-2}$	3.5	$2.03 \times 10^{-2}$	4.2	$1.76 \times 10^{-2}$	4.0	$1.79 \times 10^{-2}$	2.9	$2.62 \times 10^{-2}$
22	3.7	$1.88 \times 10^{-2}$	3.4	$2.13 \times 10^{-2}$	4.0	$1.84 \times 10^{-2}$	3.8	$1.87 \times 10^{-2}$	2.7	$2.74 \times 10^{-2}$
23	3.5	$1.96 \times 10^{-2}$	3.2	$2.22 \times 10^{-2}$	3.8	$1.92 \times 10^{-2}$	3.7	$1.96 \times 10^{-2}$	2.6	$2.86 \times 10^{-2}$
24	3.4	$2.05 \times 10^{-2}$	3.1	$2.32 \times 10^{-2}$	3.7	$2.01 \times 10^{-2}$	3.5	$2.04 \times 10^{-2}$	2.5	$2.99 \times 10^{-2}$
25	3.2	$2.13 \times 10^{-2}$	3.0	$2.42 \times 10^{-2}$	3.5	$2.09 \times 10^{-2}$	3.4	$2.13 \times 10^{-2}$	2.4	$3.11 \times 10^{-2}$
26	3.2	$2.22 \times 10^{-2}$	2.8	$2.51 \times 10^{-2}$	3.4	$2.17 \times 10^{-2}$	3.2	$2.21 \times 10^{-2}$	2.3	$3.23 \times 10^{-2}$
27	3.0	$2.31 \times 10^{-2}$	2.7	$2.61 \times 10^{-2}$	3.2	$2.26 \times 10^{-2}$	3.1	$2.30 \times 10^{-2}$	2.3	$3.36 \times 10^{-2}$
28	1.9	$2.39 \times 10^{-2}$	2.6	$2.71 \times 10^{-2}$	3.1	$2.34 \times 10^{-2}$	3.0	$2.38 \times 10^{-2}$	2.2	$3.48 \times 10^{-2}$
29	2.8	$2.48 \times 10^{-2}$	2.5	$2.80 \times 10^{-2}$	3.0	$2.42 \times 10^{-2}$	2.9	$2.47 \times 10^{-2}$	2.1	$3.61 \times 10^{-2}$
30	2.7	$2.56 \times 10^{-2}$	2.46	$2.90 \times 10^{-2}$	2.9	$2.51 \times 10^{-2}$	2.8	$2.55 \times 10^{-2}$	2.0	$2.73 \times 10^{-2}$

possible to better understand the phenomena found at the lower wave numbers of the spectra.

## 4.5 Spectral Frequency Plots

### 4.5.1 Specific Humidity Spectra

One would expect convective features to show up the most clearly in the moisture data (see Lenschow and Stephens, 1980), so we will begin by examining the specific humidity data. Figure 4.10 shows the detrended 20 Hz Lyman-alpha data traces for the selected portions of the CTBL. With the synoptic scale trends now removed, the mesoscale and microscale trends are easier to see (compare with Fig 4.6). The bottom three levels show the presence of the mesoscale wave features (with the 10's of km wavelengths) that were seen in the raw data and the specific humidity cross-sections. The levels also show greater microscale fluctuations than are found in the top two levels, which indicates that the bottom three levels are below the cloud bases. These sub-cloud traces show relative maxima that mark the presence of bands of precipitation (this is corroborated by the mission logs). The top two levels show weaker mesoscale fluctuations that indicate they are within the well-mixed cloud layer. It is important to note here that Lyman-alpha data can be unreliable within clouds, as the liquid water in the clouds can cause scattering and absorption of the instrument's laser spectrometer. The 1 Hz specific humidity data, which are more accurate within the cloud layer, were also detrended and used for spectral analysis (Fig 4.11). The three sub-cloud layers show the same mesoscale features seen in the Lyman-alpha data. The traces of cloudy levels give better evidence of mesoscale wave features than can be seen in the 20 Hz Lyman-alpha data.

Figure 4.12 shows the Lyman-alpha and specific humidity spectral plots for all five flight levels in the CTBL sample. Both types of spectra have the same

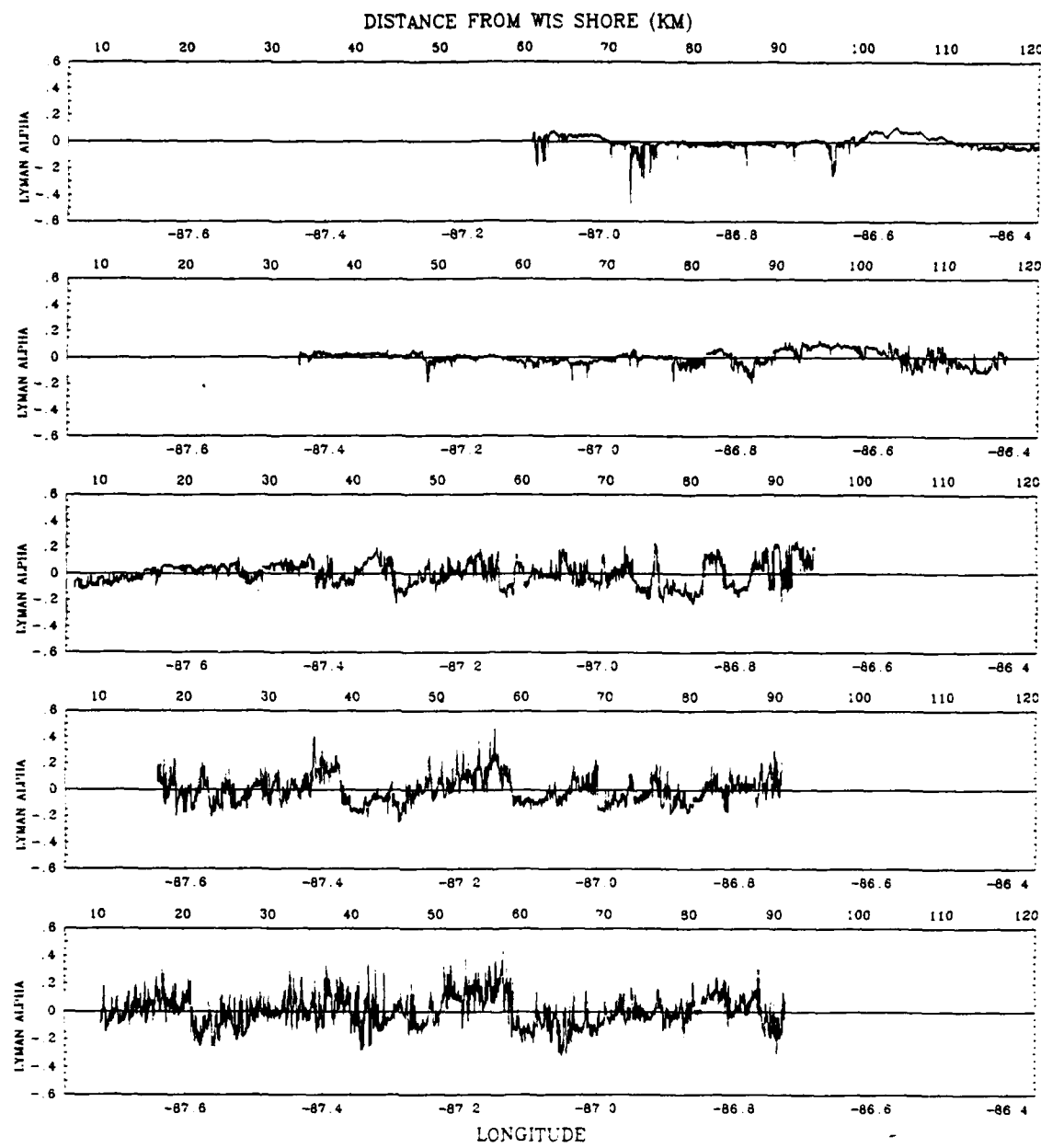


Figure 4.10 Plots of detrended aircraft Lyman-alpha measurements (g/kg) for flight levels 1 through 5 on 10 January 1984.

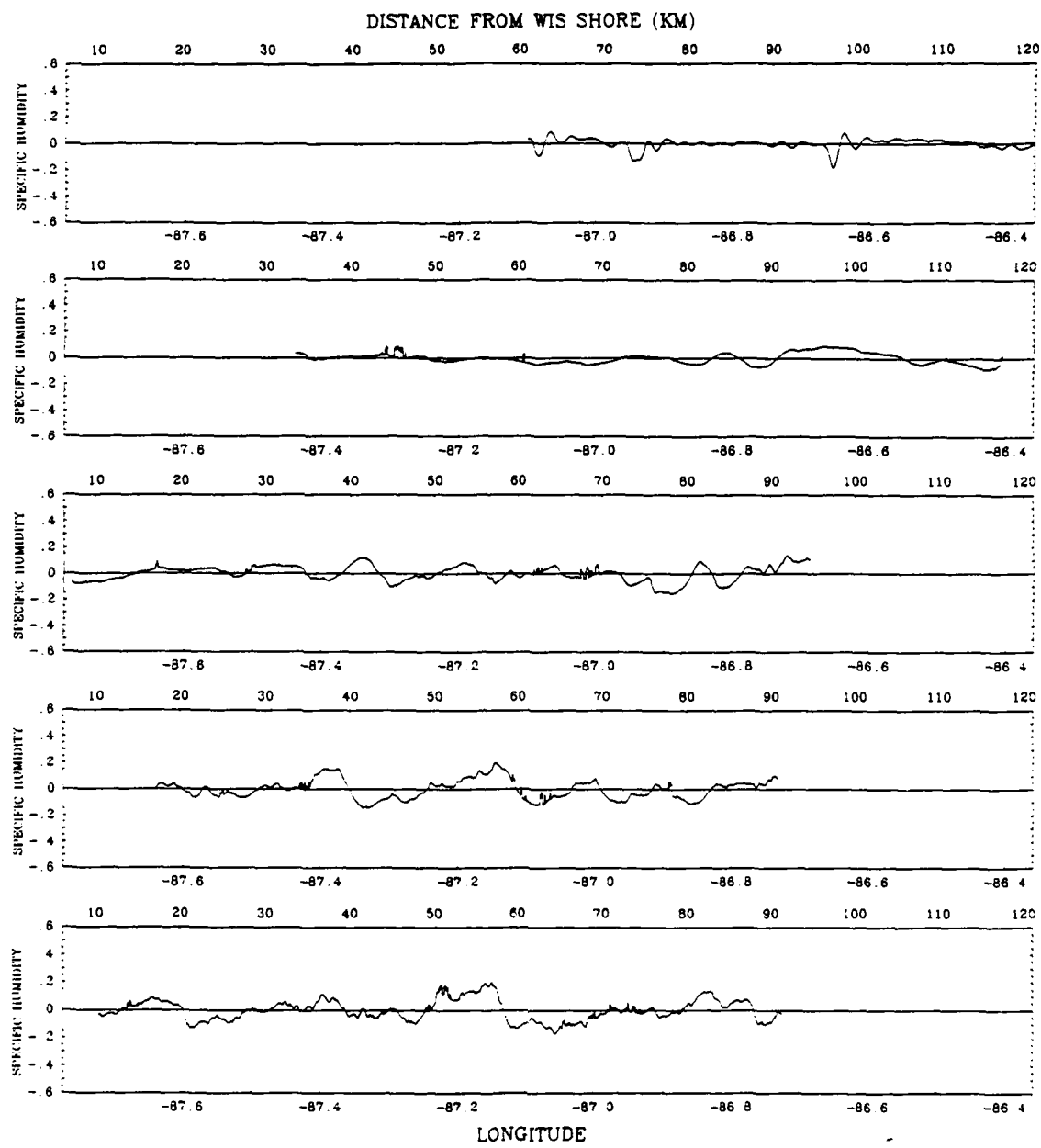


Figure 4.11 Plots of detrended aircraft specific humidity measurements (g/kg) for flight levels 1 through 5 on 10 January 1984.

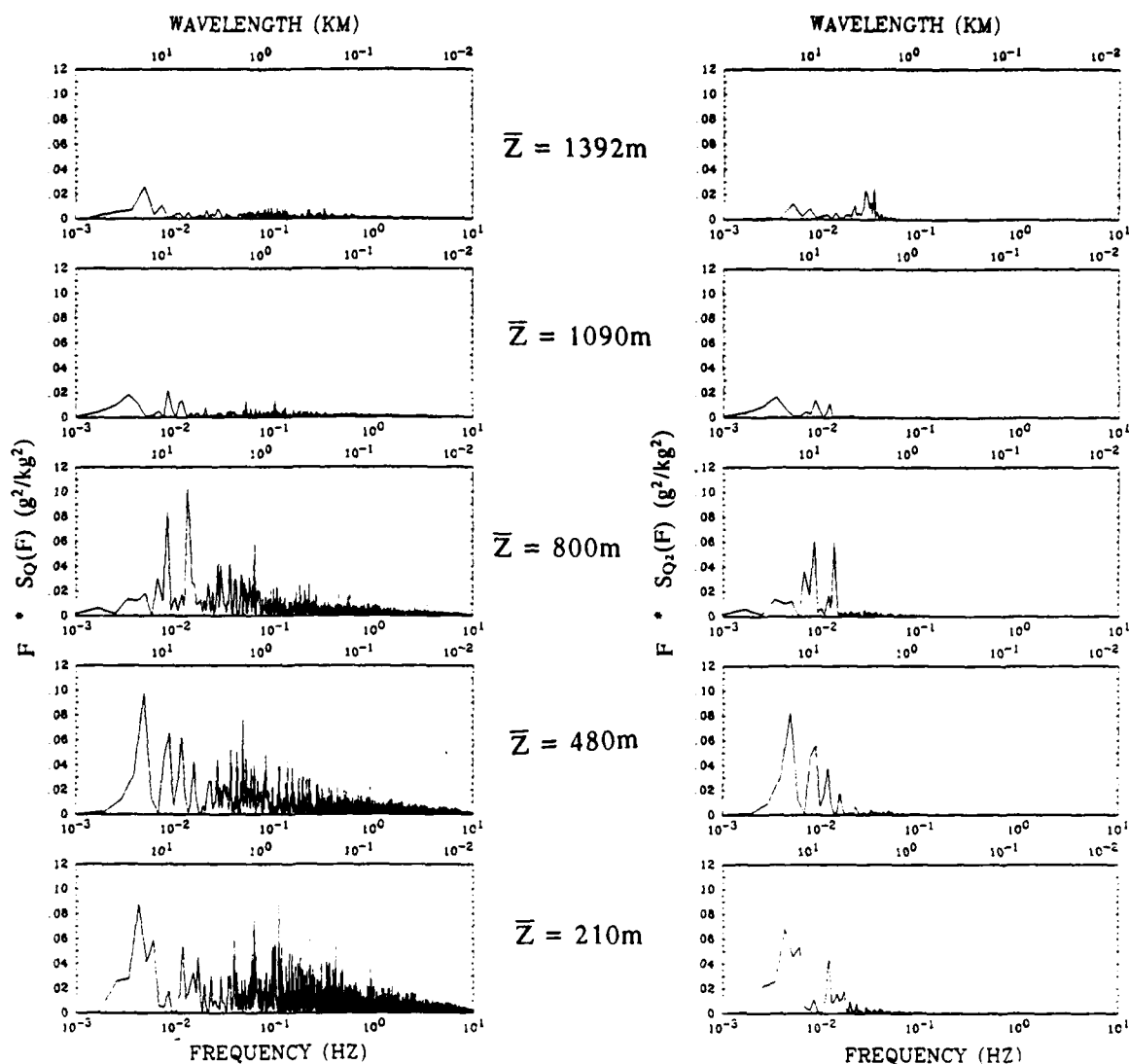


Figure 4.12 Spectral representations of the Lyman-alpha (left) and specific humidity (right) for the portions of flight levels 1 through 5 within the well-mixed CTBL.

mesoscale wave peaks in the three bottom, sub-cloud levels. The most significant spectral peak in the lower two levels is at a wavelength of approximately 16km. This peak is also present in the third level, but as a double peak and with much less energy. These peaks correspond to the mesoscale waves seen in the data plots and the CTBL cross-sections. The two cloud levels also show a weak mesoscale peak with a wavelength between 15 and 20 km. Several other strong energy peaks can be seen at slightly smaller wavelengths (5 – 10km) in the bottom three levels. These peaks (between 5 and 15km) correspond to the higher convective mode (HCM), associated with the 2-D cloud streets, found in the King Air spectra analyzed by Agee and Gilbert (1989). The energy associated with the HCM increases with height in the sub-cloud layer of the CTBL. In the top two levels, within the cloudy layer, the HCM peaks rapidly disappear with height. The overall spectral energy is much less in the cloud layer than in the sub-cloud layer, indicating that there is less horizontal variation in humidity in the cloudy layer, and that the amount of water vapor in the air decreases with height within the clouds (see Lilly, 1968). This decrease in humidity with height can be seen in the top level, where the HCM becomes insignificant and is overshadowed by significant peaks at 2 and 3 km in the 1 Hz specific humidity spectra.

In their spectral analysis of AMTEX aircraft data, Ross and Agee (1985) discovered a Basic Convective Mode (BCM) in the 3 – 5 km wavelength band (at 1.5  $Z_i$  as reported by Kaimal, et al. (1976)).  $Z_i$  was approximately 2km in this case. The BCM is the initial mode at which organized mesoscale convection occurs and has an aspect ratio typically of about 3 to 1. In their study of MCC cases during AMTEX, Ross and Agee also found a MCC spectral mode with an aspect ratio of about 30 to 1. The wavelength of the convective mode is determined by the spacing of the convective 2-D bands or the diameter of the 3-D cells. The aspect ratio is defined as the

wavelength divided by the convective depth. In the case of this Lake Michigan convection, the spectral peaks at 30 – 35 km appear to be associated with the larger scale organized convection. The changes in the spectral plots with height seem to indicate that most of the spectral energy is in the HCM at the lower levels, and that the energy is transferred from this range upscale to the MCC and downscale to the BCM at the higher levels in the CTBL. At the top level, where the BCM is significant and the mean depth of the CTBL is 1.9km, the aspect ratio is approximately 3 to 1.

#### 4.5.2 Temperature and Virtual Potential Temperature Spectra

The detrended temperature and virtual potential temperature plots (Figs 4.13 and 4.14) show strong similarities in their mesoscale and microscale fluctuations. The sizes of the turbulent microscale fluctuations are larger than those seen in the humidity data. The mesoscale waves (on the scale of 10's of km) are also present here. The temperature and  $\theta_v$  data plots show strong similarities to the synoptic scale trends, but the mesoscale and microscale differences between the two are more obvious when comparing their spectra (Fig 4.15). The temperature spectra show more energy overall in the mesoscale and wavelengths ( $> 1\text{km}$ ) than do the  $\theta_v$  spectra. This clearly shows the inverse correlation between temperature and humidity, where the effect of the specific humidity on the  $\theta_v$  spectra decreases the intensity of the mesoscale and microscale fluctuations. The dominant spectral peak at all levels for both temperature and  $\theta_v$  is at the 30 – 45 km wavelength, which corresponds to the MCC wavelengths.

This MCC spectral peak remains strong at all levels with the exception of the top level of the CTBL. Both T and  $\theta_v$  spectra have secondary spectral peaks between the 5 and 20km wavelengths (the HCM). The energy of these peaks tends to decrease with height in the sub-cloud layer. In the two levels within the well-mixed cloud layer, the HCM at the 16 km wavelength has become dominant at the expense of the

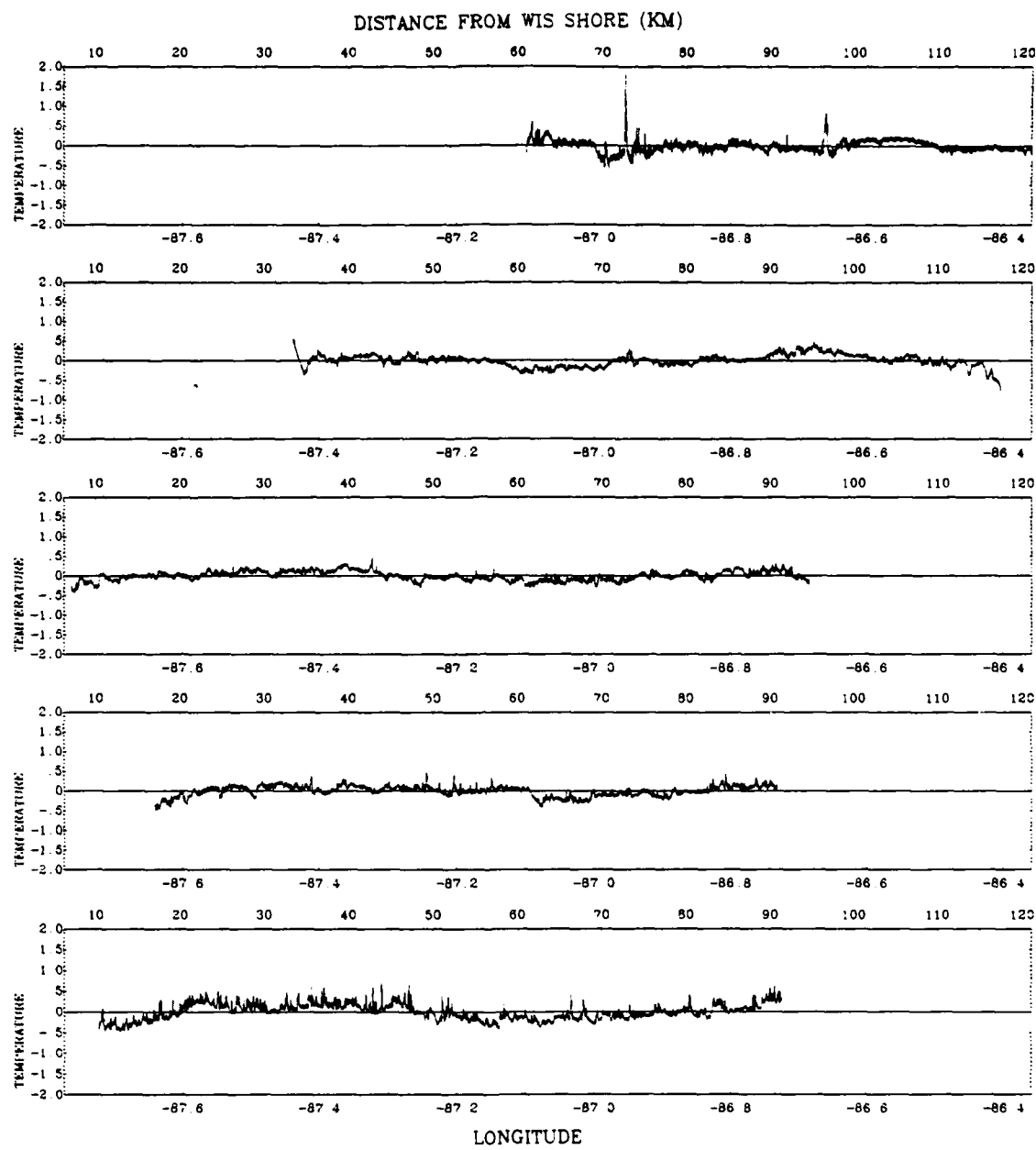
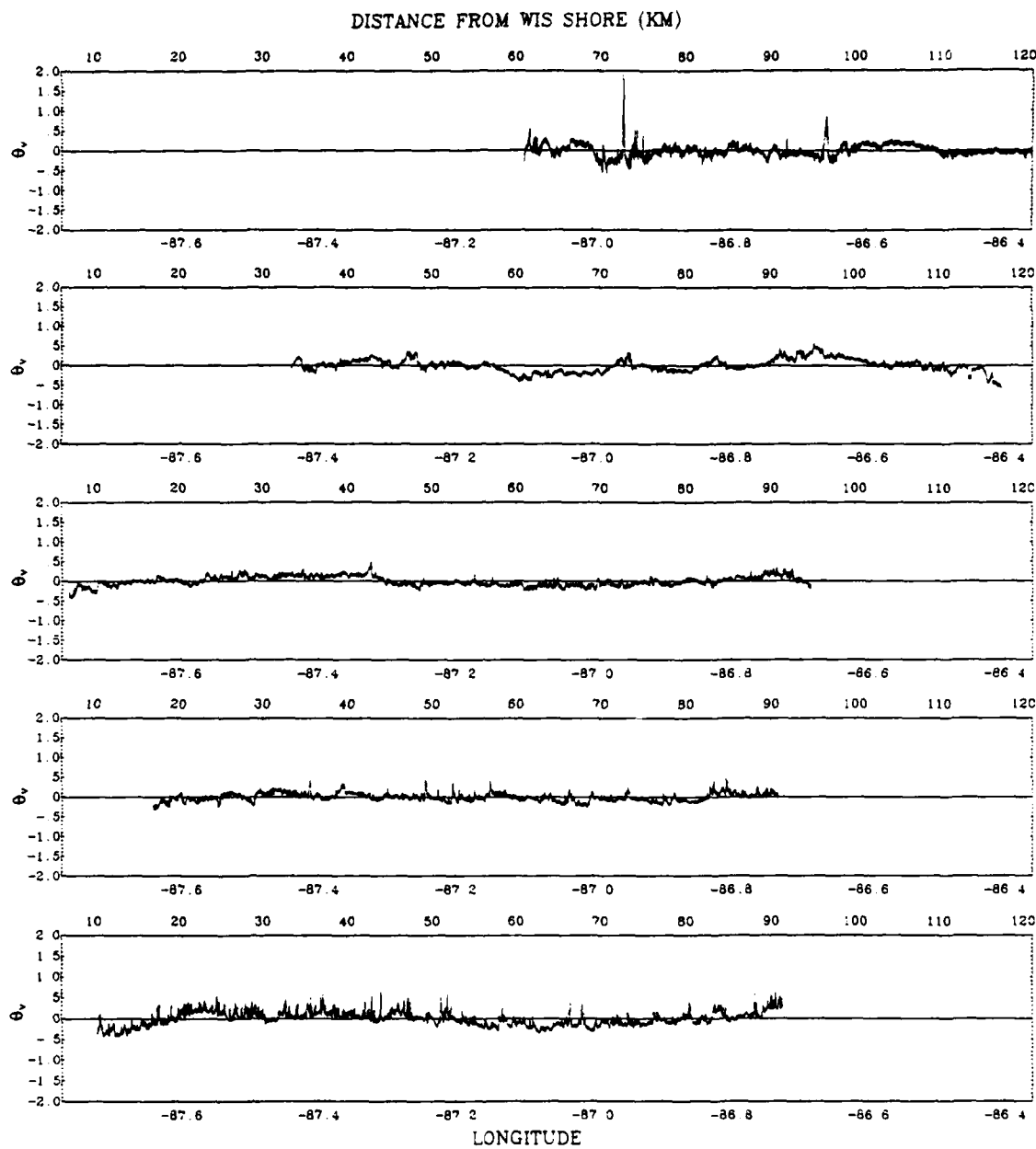


Figure 4.13 Plots of detrended aircraft ambient temperature measurements ( $^{\circ}\text{C}$ ) for flight levels 1 through 5 on 10 January 1984.



**Figure 4.14** Plots of detrended aircraft virtual potential temperature measurements ( $^{\circ}$ K) for flight levels 1 through 5 on 10 January 1984.

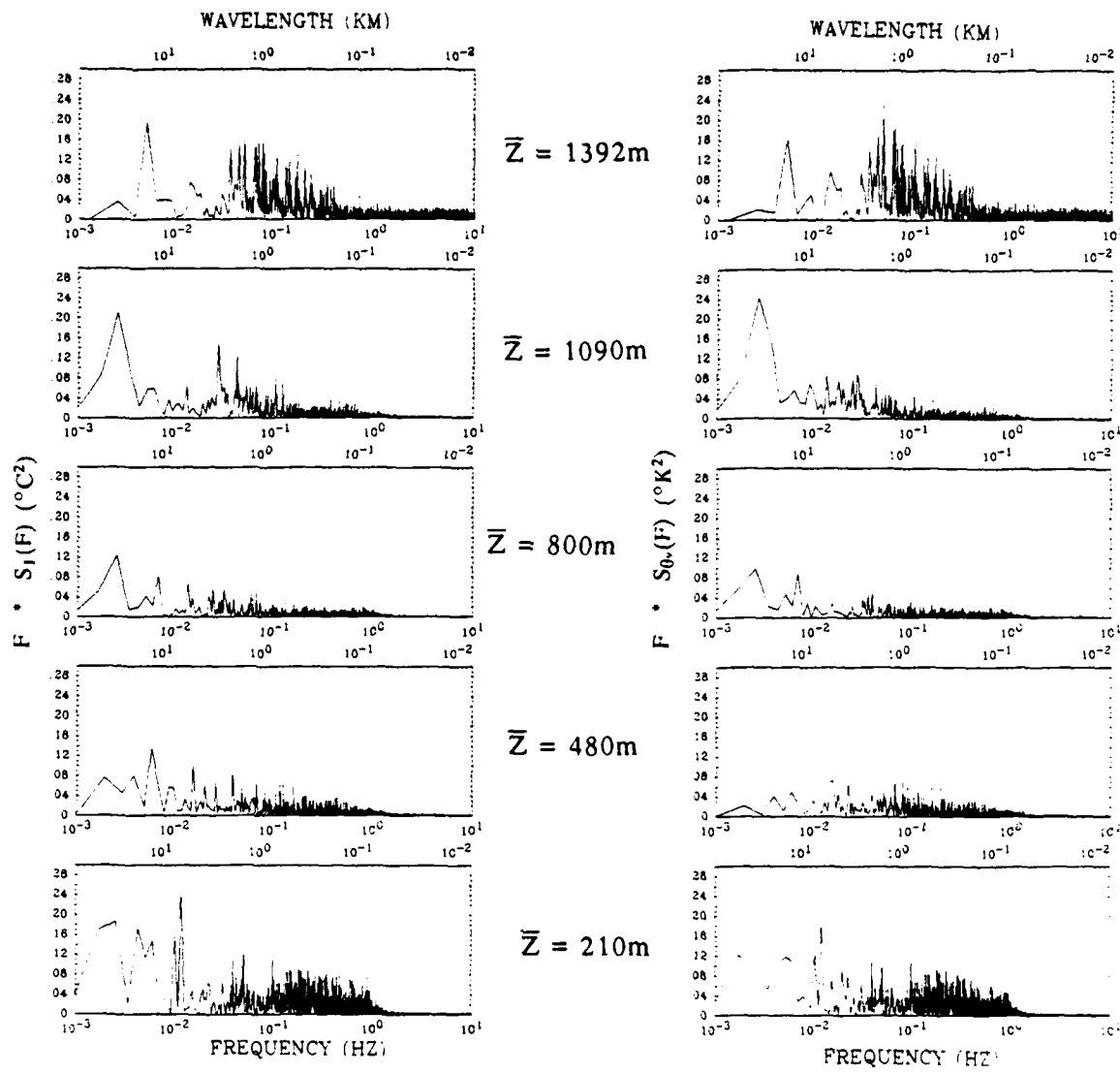


Figure 4.15 Spectral representations of the ambient temperature (left) and virtual potential temperature (right) for the portions of flight levels 1 through 5 within the well-mixed CTBL.

MCC. In the top two levels, within the cloud layer, the wavelengths associated with the BCM (1 – 3 km) also show a significant increase in energy.

At the top level, the energy at the BCM wavelengths is stronger for the  $\theta_v$  spectra than for the T spectra, which seems to contradict the inverse correlation between temperature and specific humidity. The dependence of  $\theta_v$  on specific humidity, with its strong BCM spectral signal, accounts for this seeming contradiction. The turbulent mixing between the top of the CTBL and the inversion layer also contributes to the increase in energy in the inertial subrange wavelengths (100m to 1km) at the top flight level. The energy increase at the BCM wavelengths also increases with height within the well-mixed cloud layer. In this case, the energy transfer is from the MCC to the shorter wavelengths of the HCM and the BCM. In the sub-cloud layer the energy transport is from the HCM to the MCC wavelengths.

#### **4.5.3 U and V Wind Component Spectra**

The turbulent microscale fluctuations seen in the U and V wind components (Figs 4.16 and 4.17) are much stronger than those in the temperature and humidity data. The mesoscale wave structures are also more strongly defined here. There seems to be several different mesoscale wavelengths present in both the U and V components. In the U (or cross-roll) component, the wind shift associated with the Wisconsin land breeze convergence is still present despite detrending. Another weaker wind shift associated with the mid-lake convective band is visible, now that the synoptic scale trends are removed. In the V component (parallel to the roll axes), the mesoscale wavelengths are visible, especially at the top level. In this northerly flow case, the spectral plots should reveal more information on the size of the 2-D cloud streets found over the lake.

Figure 4.18 contains the spectral plots for both U and V wind components. The most significant spectral peak in the U component spectra tends to be found at the

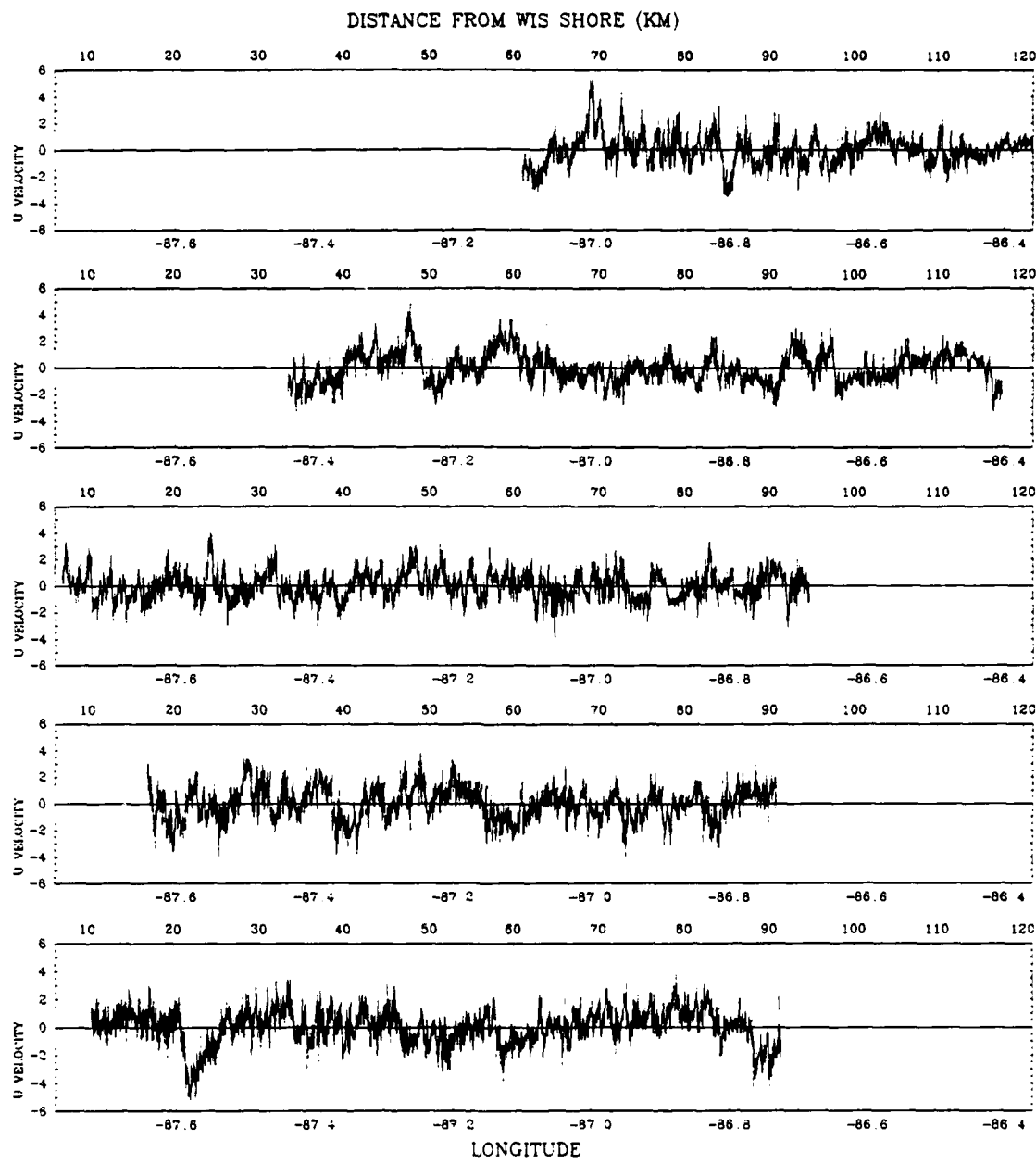


Figure 4.16 Plots of detrended aircraft u wind component measurements (m/s) for flight levels 1 through 5 on 10 January 1984.

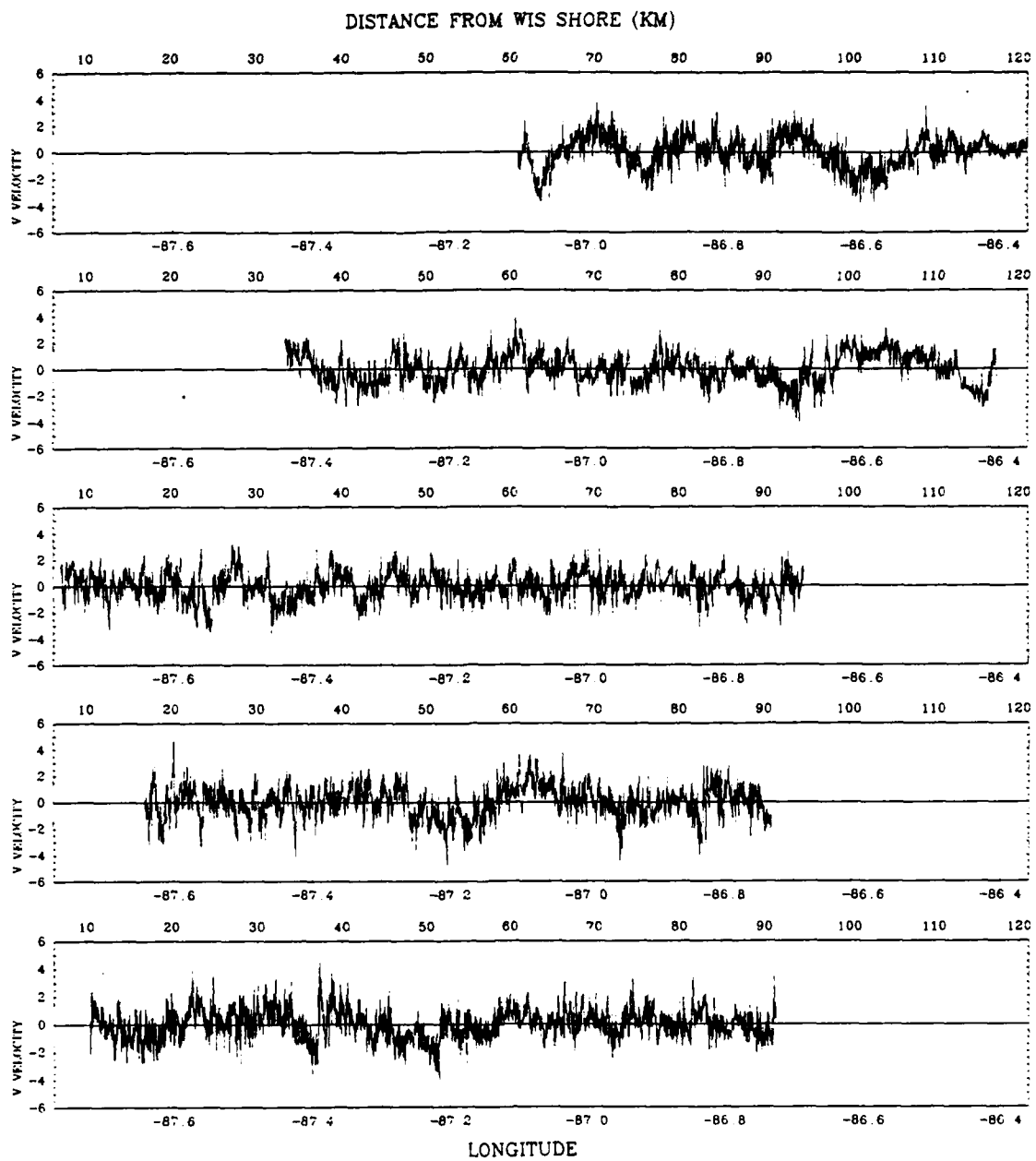


Figure 4.17 Plots of detrended aircraft v wind component measurements (m/s) for flight levels 1 through 5 on 10 January 1984.

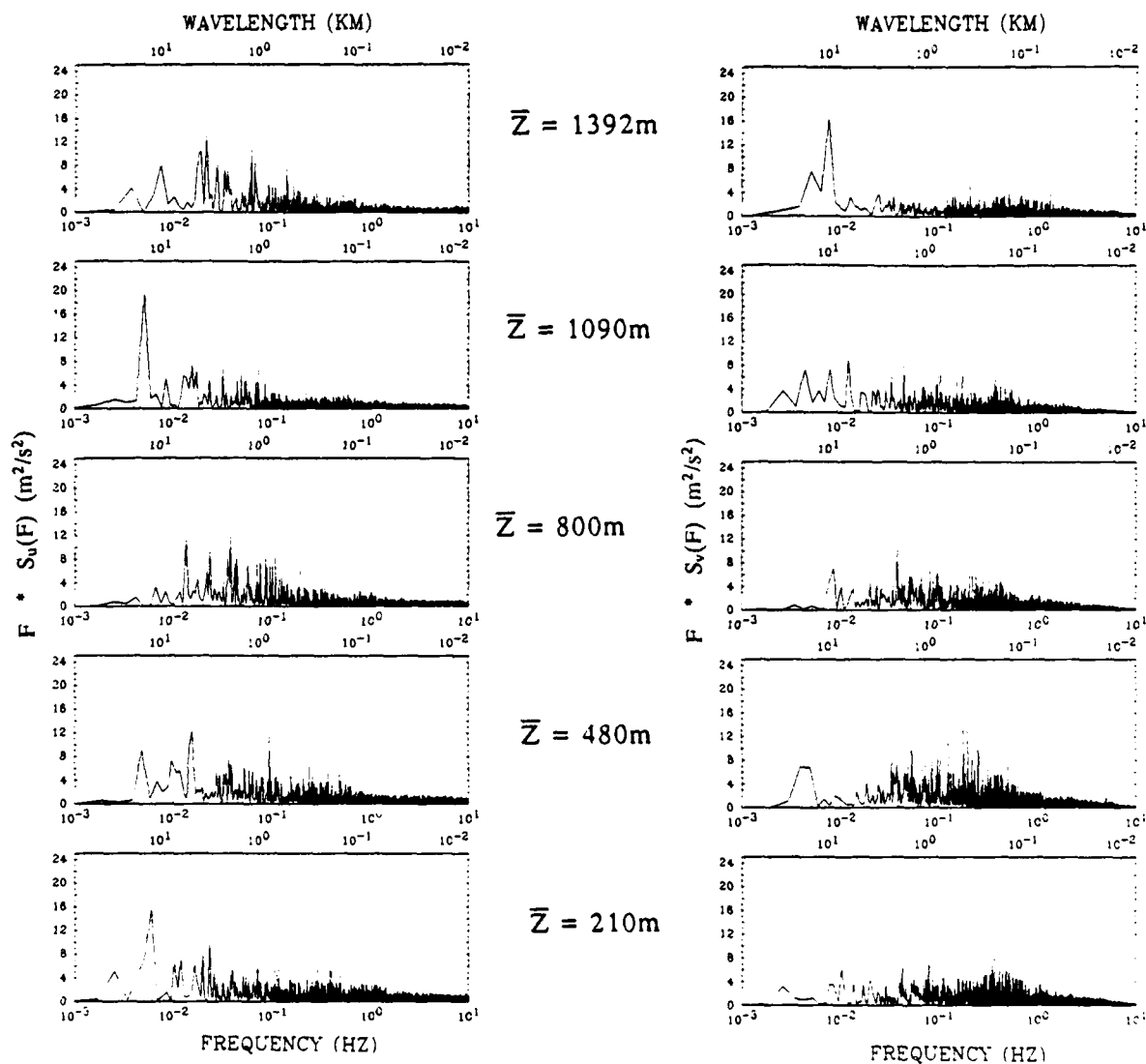


Figure 4.18 Spectral representations of the  $u$  wind component (left) and  $v$  wind component (right) for the portions of flight levels 1 through 5 within the well-mixed CTBL.

HCM wavelengths (5 – 20km), which are the mesoscale wavelengths associated with the larger convective structures. This peak is present at all levels, but tends to decrease with height in the bottom three sub-cloud levels. The peak reappears strongly in the fourth flight level (the one closest to the cloud base height) and also decreases with height within the well-mixed cloud layer. A weak spectral peak at the MCC wavelengths (20 – 40km) is present at all levels and changes little with height. In the sub-cloud layer the energy at the longer wavelengths of the HCM (10 – 20km) decreases with height, with a net transfer of energy to the shorter wavelengths of the HCM (5 – 10km). In the top two levels, within the well-mixed cloud layer, energy of the HCM (5 – 20km) decreases strongly with height, as the BCM wavelengths (2 – 5km) grow rapidly with height. The main energy transport is from the HCM to the BCM within the CTBL. Within the well-mixed cloud layer, there is also an energy transfer from the HCM to the MCC.

In the V component spectra the most significant spectral peaks are found at the HCM wavelengths. The MCC peaks (20 – 40km) are minor or almost non-existent at all five levels. The HCM peaks (5 – 20km) tend to become stronger with height and the wavelengths become longer; from 7.5km near the surface to 10km near the top of the CTBL. The BCM can be seen in the two flight levels within the well-mixed cloud layer, but are not very significant. The amount of energy in the inertial subrange (100m to 1km) is greater in the sub-cloud levels and decreases with height. The energy transport is from the shorter to the longer wavelengths, to the HCM in particular and to the BCM to a much lesser extent. The strong HCM signal seems to indicate that the approximate size of the 2-D cloud streets is about 10km.

#### 4.5.4 Vertical Velocity Spectra

The long-term average in the vertical velocity data was forced to zero during the data-processing step by use of the aircraft pitch and attack angle. As a result, it is

not necessary to detrend the vertical velocity data. Figure 4.19 shows the velocity data traces for the selected portions of the CTBL. It is obvious that while the top level is represented by 20 Hz data, the bottom four levels are not true 20Hz data. The high frequency turbulent fluctuations present in the top level are missing from the bottom four levels. The top level data came from the King Air aircraft, while the bottom four levels were recorded by the Queen Air aircraft. Further investigation of the records kept on flight mission # 85 (10 Jan 84) give no real clues as to why the Queen Air data are missing the higher frequency turbulent fluctuations. A likely cause of the error in the data is instrument problems (or more specifically, icing of the vertical gust probe), but there is no record of this happening in the mission reports. It is also possible that an error in processing the Queen Air data could have caused the problem, but there is no record of this either. A check of the raw INS vertical velocity data (1Hz data recorded by the aircraft that measures the larger scale wind fluctuations rather than the turbulent gusts) shows that the vertical velocity data do capture the larger wind fluctuations accurately. These data had to be used with appropriate caution, but it was still possible to get 1Hz information on the mesoscale and microscale fluctuations in vertical velocity. The four lower levels show evidence of the mesoscale waves (with a 10km wavelength) seen in the U and V wind components. The top level also shows mesoscale waves, but at smaller wavelengths than at the lower levels.

A comparison of the spectra between the Queen Air and King Air data for the fourth and fifth levels (Fig 4.20) shows that the missing turbulent fluctuations in the Queen Air data affect the spectra in the higher frequencies and the shorter wavelengths. The logarithmic spectral plot of the King Air data shows the expected  $-2/3$  slope in the inertial subrange (as was detected by Agee and Gilbert, 1989), while the logarithmic plot made of the fourth level data from the Queen Air shows a

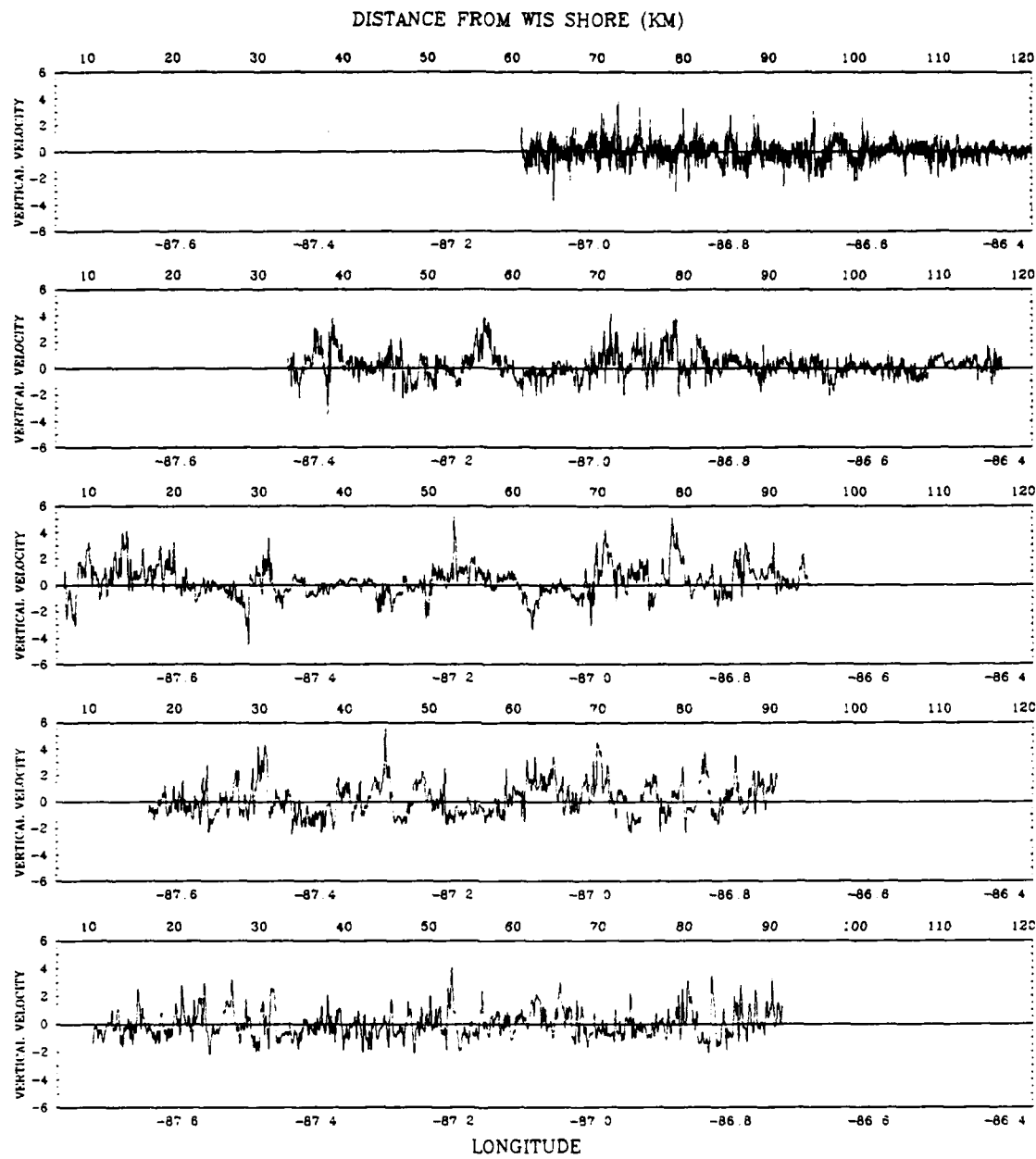
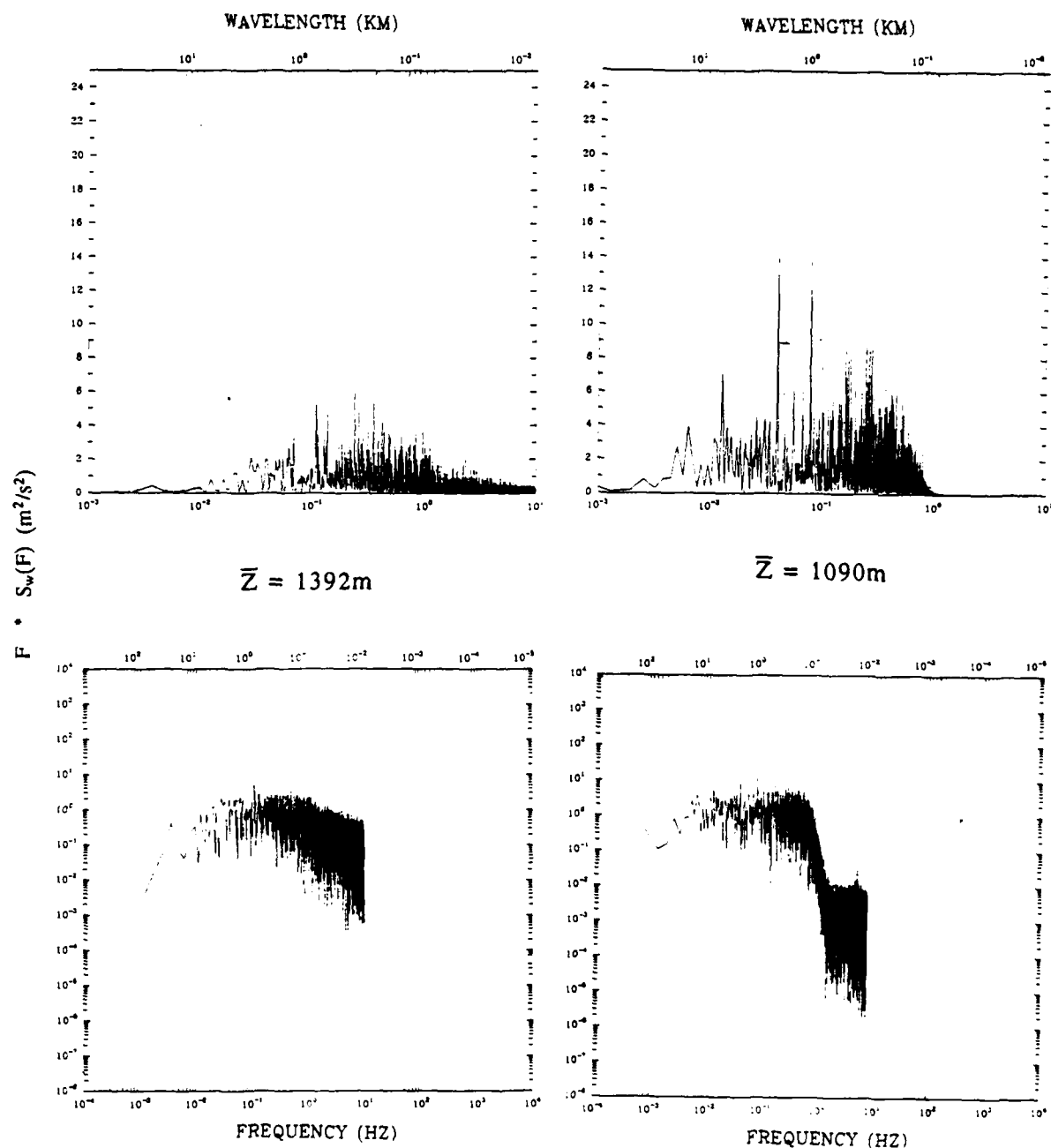


Figure 4.19 Plots of raw aircraft w wind component measurements (m/s) for flight levels 1 through 5 on 10 January 1984.



**Figure 4.20** Spectral representations of the  $w$  wind component, comparing the King Air (left) vs. the Queen Air (right) data.

sharp drop-off in the signal at the higher frequencies ( $> 1 \text{ Hz}$ ). The signal present at frequencies higher than 1 Hz is merely the effect of the instrument noise. When interpreting the vertical velocity spectra, only those frequencies below 1 Hz can be used.

Figure 4.21 shows the spectra for all five flight levels, where all frequencies greater than 1 Hz have been filtered for the bottom four levels. The linear spectral plots show that most of the energy in the spectra is confined to the inertial subrange, in the wavelengths between 100m and 1km. The amount of energy present in the inertial subrange decreases with height within the CTBL. The overall spectral energy for all five flight levels decreases as the height increases. The three sub-cloud levels in the CTBL also show evidence of some larger scale wave features. There are also several less significant peaks near the HCM wavelengths (5 – 20km). These spectral peaks increase somewhat in both energy and wavelength with height within the sub-cloud layer. The HCM spectral signature disappears with height within the cloud layer, while the BCM mode is present at both levels but decreases with height. The energy transport is from the inertial subrange to the HCM and BCM in the sub-cloud layer, and from the HCM to the BCM in the cloud layer. The main energy transport is from the inertial subrange to the longer wavelengths, with some of the energy apparently dissipating into the shorter wavelengths (which are unfortunately missing from the data) as well. The logarithmic spectral plots show the expected  $-2/3$  slope in the top level. The bottom four levels are missing the higher frequency data, but there is some evidence of a  $-2/3$  slope in the abbreviated spectra.

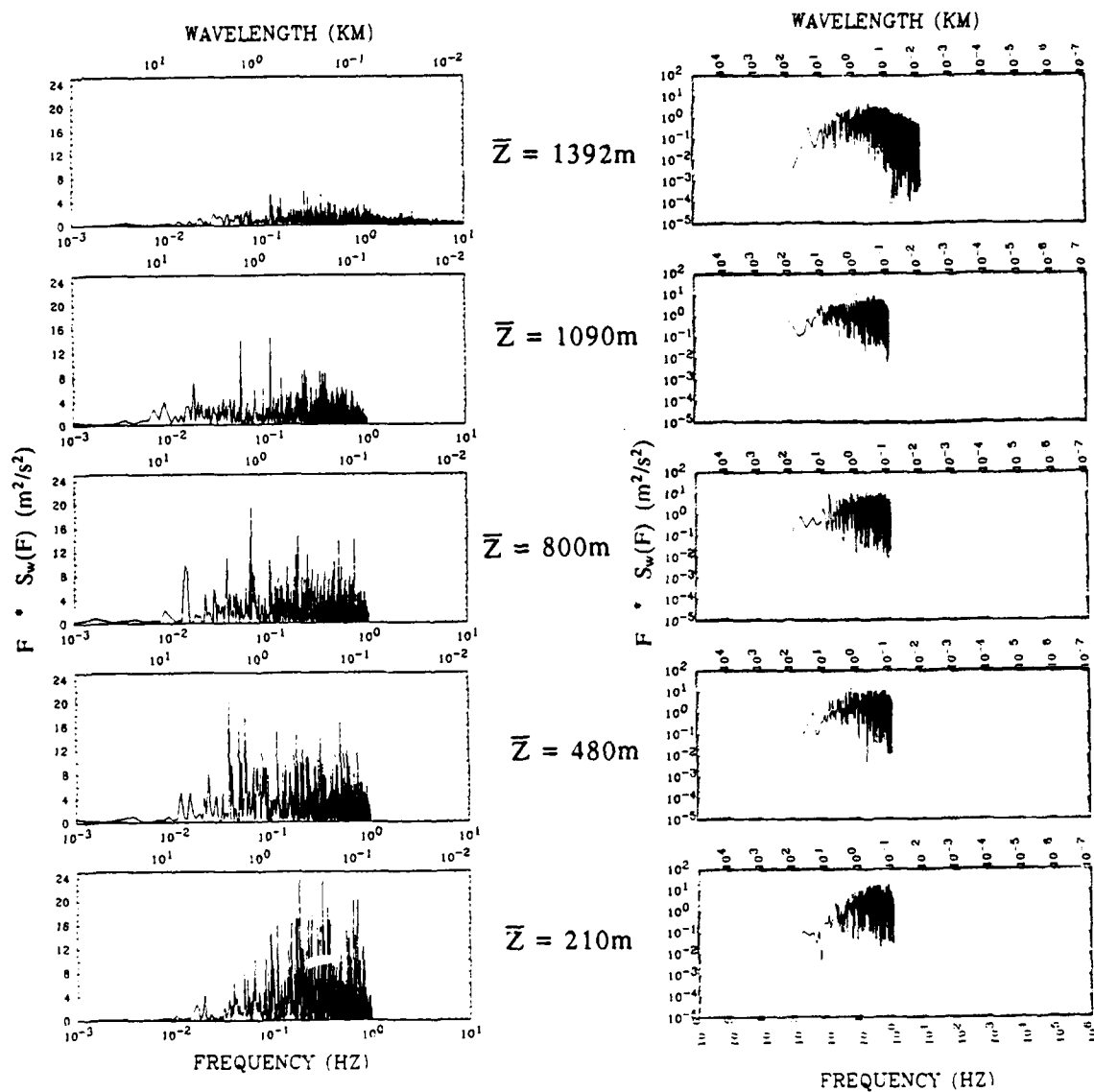


**Figure 4.21** Spectral representations of the  $w$  wind component for the portions of flight levels 1 through 5 within the well-mixed CTBL. The log-log plot for level 5 (top right) shows  $-2/3$  slope in the inertial subrange.

## 4.6 Turbulent Fluxes

### 4.6.1 Mean Profiles

This unique data set provides an opportunity to better understand the structure and dynamics of a Type I CTBL by an examination of the heat, moisture, and momentum fluxes. Observational case studies have been done on the Type II CTBL (Nicholls, 1984) to measure the turbulent transports and test model assumptions, but this case study gives the first opportunity to make quantitative estimates of the turbulent transports for multiple levels within a Type I CTBL. The complicated structure found in this CTBL, with its variation in the inversion height and its land breeze boundaries, makes it necessary to choose a portion of the CTBL away from the influence of any external forcing. A 10km segment of the CTBL, between 61 and 71 kilometers from the Wisconsin shore (to the east of the mid-lake convective band), was selected. This segment of the CTBL is sufficiently far from the influence of the land breezes, and is short enough that the change in the CTBL depth is relatively small. This segment is subdivided into two 5km sections to further minimize the change in CTBL depth.

The inversion height at 61km is 1395m above sea level, and increases to approximately 1500m at 71km, with a mean inversion height of 1450m over the 10km segment. The mean inversion height over the western 5km segment is 1400m, just above the height of the top flight level. The mean inversion height over the eastern segment is 1500m, with the top flight level approximately 100m below the height of the cloud tops. The height of the cloud bases range from 700m above sea level at 61km to 810m at 71km, with an average cloud base height of 790m for the whole 10km. The average cloud base height is 750m for the western segment, and 800m for the eastern 5km segment.

Figure 4.22 shows the mean vertical profiles of wind, temperature, and

Figure 4.22 Vertical profiles of the mean wind components, temperature and virtual potential temperature, and specific humidity.

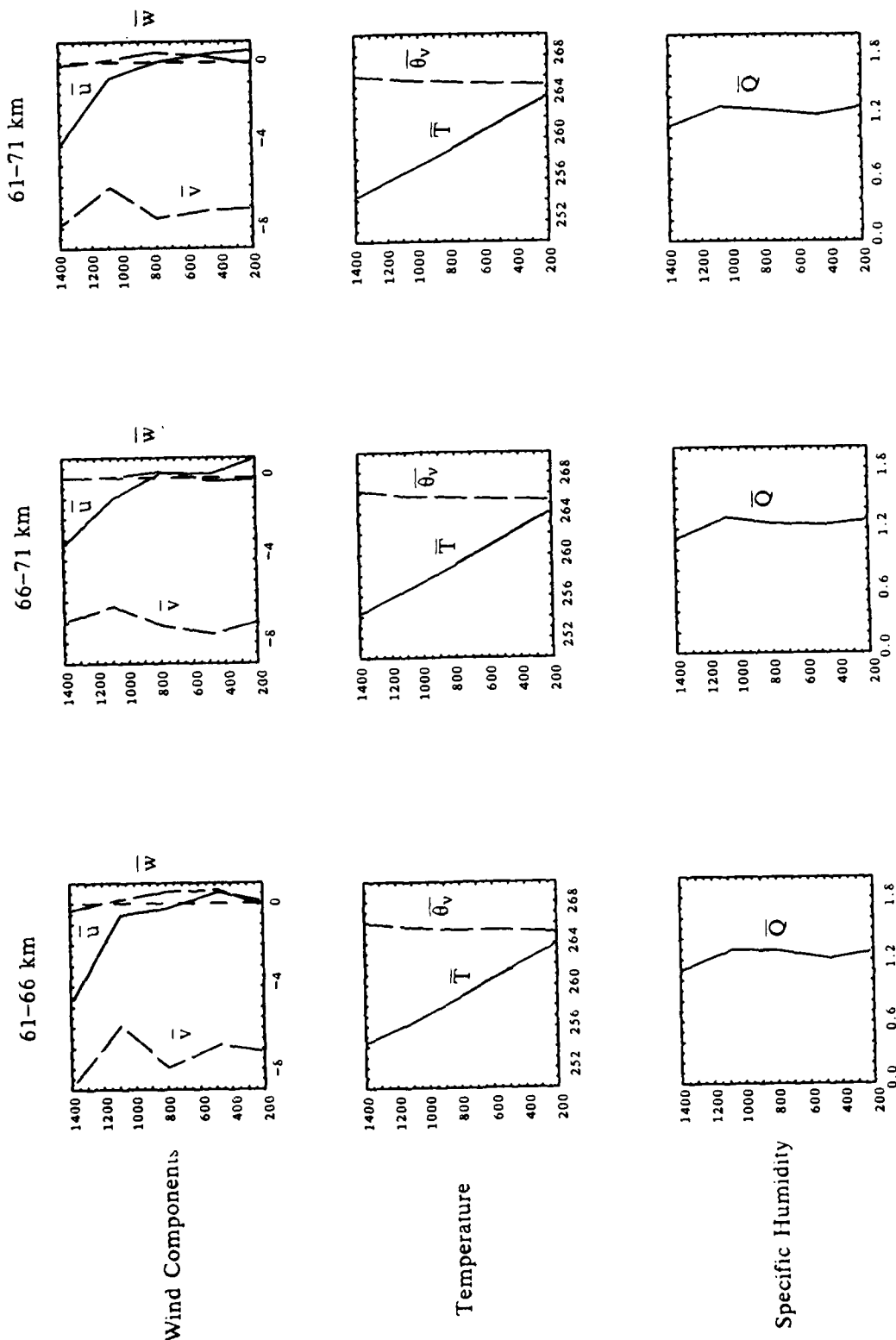


Figure 4.22

moisture for the 10km segment and its two sub-sections. When interpreting these 'profiles' it is important to note that these data consist of five discrete data levels, rather than a true sounding. It should be kept in mind that parts of the profiles between the data levels are linear interpolations.

The U (or cross-roll) wind component shows westerly flow in the sub-cloud layer. The flow becomes easterly in the well-mixed cloud layer, with a maximum in the return flow region at the top of the CTBL. The V component (along the roll axes) is northerly throughout the CTBL. There is a minimum in the northerly wind component present just above the cloud bases. The maximum northerly flow is at the very top of the CTBL, where the influence of the synoptic scale flow in the free atmosphere is felt. The northerly flow is almost constant in strength in the sub-cloud layer. There is weak downward vertical velocity at the surface of the CTBL, but it quickly changes to upward velocity in the sub-cloud layer. The maximum upward vertical velocity is found at the height of the cloud bases. The upward velocity decreases with height in the well-mixed cloud layer and changes to weak downward velocity at the top of the CTBL, where the effects of radiative cloud-top cooling and entrainment from the inversion are strong.

The temperature profiles show a linear decrease with height for all three profiles, and are almost identical. The virtual potential temperature profiles are also very similar in all three profiles, and show a well-mixed CTBL with a very slight temperature increase with height in the cloud layer. The entrainment of warmer inversion air is partially responsible for this warming. The specific humidity profiles are also very similar in all the profiles. All the profiles show two areas of maximum moisture values. One is at the CTBL surface under the influence of thermal forcing. The second maximum is found in the lower levels of the well-mixed cloud layer, above the cloud bases. This maximum is caused by the combination of an upward

moisture flux from the lake driven by convection, and a downward moisture flux from the top of the CTBL caused by entrainment instability (see Deardorff, 1980b, and Randall, 1980). This instability is the result of air parcels from the inversion layer becoming unstable by evaporative cooling and sinking into the lower levels of the cloud, thus transporting water vapor back to the cloud base. The humidity profiles also indicate a well-mixed CTBL by their high values throughout the layer.

#### 4.6.2 Covariance Calculations

The heat, moisture, and momentum fluxes were determined by calculating the vertical velocity variance, vertical turbulent kinetic energy (TKE), and the covariances. The first step in the process of calculating the covariances was to detrend the data for the chosen segments of the CTBL. Then the average data values for each segment were subtracted from the instantaneous values to obtain the perturbation values. The turbulent fluctuations were multiplied together to form the covariances, then averaged over the length of each segment. The vertical velocity data cannot be treated as true 20Hz data, so all the covariances were calculated based on half-second sampling (2Hz data). Table 4.2 lists the covariances for all five levels of each CTBL segment.

The momentum fluxes for the three segments are depicted in Figure 4.23. The method used to calculate the turbulent momentum fluxes results in a turbulent vertical velocity of the same order of magnitude or an order of magnitude larger than the horizontal turbulent velocity. The vertical velocity variances ( $\bar{w}^2$ ) are an order of magnitude larger than those observed in a Type II CTBL over the North Sea by Nicholls (1984). The variance profile for the eastern segment has a maximum value at the CTBL surface, with a secondary maximum at the cloud base. The profiles for the western segment and the 10km segment show a maximum in the middle of the sub-cloud layer, and second maximum in the well-mixed cloud layer. The two

**Table 4.2** Covariance, variance, and skewness values for a representative sample of the convective boundary layer.

### BOUNDARY LAYER SOUNDING

#### FLUX VALUES (61 - 66km)

LEVEL	$\overline{W'Q'}$	$\overline{W'T'}$	$\overline{Q'T'}$	$\overline{W'\theta_v'}$	$\overline{U'W'}$	$\overline{V'W'}$	$\overline{W'^2}$	$\overline{W'^3}$
5	.0043	.0235	-.0026	.0295	-.0235	-.0585	.2428	-.0167
4	.0094	.0240	.0007	.0249	-.1130	-.1514	1.1210	.2034
3	.0227	.0221	.0009	.0259	-.0013	.1357	1.1886	.6619
2	.0292	.0067	.0011	.0421	-.0095	.3897	1.3404	.7636
1	.0249	.0278	.0007	.0276	.0381	.0442	.7050	.5541

#### FLUX VALUES (66 - 71km)

LEVEL	$\overline{W'Q'}$	$\overline{W'T'}$	$\overline{Q'T'}$	$\overline{W'\theta_v'}$	$\overline{U'W'}$	$\overline{V'W'}$	$\overline{W'^2}$	$\overline{W'^3}$
5	.0014	.0136	.0003	.0133	-.0155	-.0115	.4012	.0165
4	.0062	-.0011	.0001	.0070	.1647	-.1991	.7175	.0250
3	.0385	.0176	.0011	.0191	-.0620	-.2161	1.0881	-.3507
2	.0298	.0517	.0018	.0665	-.2300	.1738	1.2837	2.2549
1	.0485	.1092	.0061	.1134	.2064	.0062	1.5902	1.7546

#### FLUX VALUES (61 - 71km)

LEVEL	$\overline{W'Q'}$	$\overline{W'T'}$	$\overline{Q'T'}$	$\overline{W'\theta_v'}$	$\overline{U'W'}$	$\overline{V'W'}$	$\overline{W'^2}$	$\overline{W'^3}$
5	.0023	.0209	-.0010	.0038	-.0455	.0549	.3492	.0388
4	.0082	.0084	.0003	.0138	.0448	-.1953	.9238	.1654
3	.0389	.0145	.0006	.0223	-.1034	-.1332	1.1582	.1769
2	.0254	.0310	.0016	.0562	-.1048	.2564	1.4760	1.5243
1	.0347	.0735	.0023	.0764	.0986	.0497	1.1540	1.1366

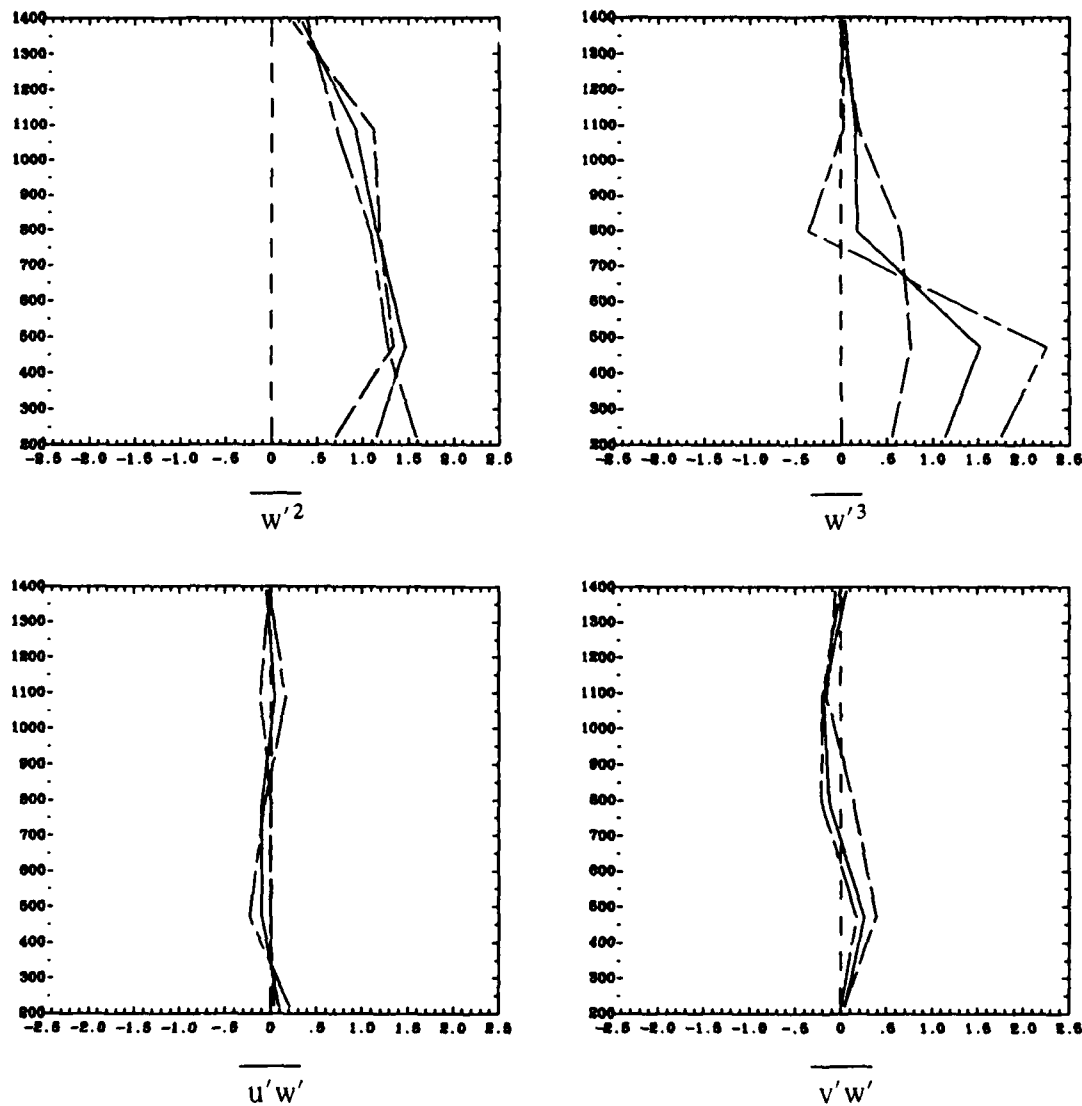


**Figure 4.23** Variance of vertical velocity, the vertical TKE, and the horizontal covariances of vertical velocity. The dashed lines represent the segments from 61-66 km and 66-71 km, respectively. The solid line represents the 61-71 km average.

profiles roughly correspond to variance profile measured by Nicholls. The western segment (61 – 66km) matches the North Sea data the most closely. These two separate  $\overline{w'^2}$  maxima are due to two separate convective processes simultaneously occurring in the CTBL. In the sub-cloud layer turbulence is generated by heating from below, while in the well-mixed cloud layer the turbulence is caused by both surface heating and cloud-top cooling. This interpretation may also explain the results of a large-eddy simulation model by Meng (1986). This model is driven primarily by radiational cooling and shows the maximum generation of turbulence in the cloud layer.

The vertical turbulent flux of the vertical component of TKE ( $\overline{w'^3}$ , also known as the skewness) profiles for all three segments also show maximum upward transport in the sub-cloud layer, and maximum downward transport at the base of the well-mixed cloud layer. This downward maximum is absent from the western profile because the cloud base height is between the second and third flight levels, and was therefore missed. The upward TKE flux increases slightly with height in the lower half of the cloud layer, then decreases with height in the upper half of the layer. At the very top of the CTBL there is a weak downward TKE flux. These flux profiles show good agreement with those from the North Sea data, when taking into account the effects of surface heating. The results of a large-eddy simulation model are almost the exact opposite, where radiational and evaporative cooling caused a strong downward flux in the sub-cloud layer and an upward flux in the cloud layer. The results calculated here suggest that the sub-cloud and well-mixed cloud layers may have different processes governing the turbulent energy transport, with radiational cooling and entrainment playing locally important roles inside the cloud layer.

The momentum fluxes,  $\overline{u'w'}$  and  $\overline{v'w'}$ , don't correspond as closely to the North Sea (Nicholls, 1984) results. The  $\overline{u'w'}$  component has a maximum at the

CTBL surface, and decreases to a minimum in the middle of the sub-cloud layer. The flux becomes approximately zero near the cloud base. The flux then increases to a relative maximum just above the cloud base and decreases again to a zero value at the cloud top. The  $\bar{v'w'}$  component flux is positive in the sub-cloud layer, with a maximum at the mid-point of the layer. The flux becomes negative in the lower part of the cloud layer with a minimum near the cloud base. The flux becomes approximately zero at the top of the CTBL. The difference in these profiles from the North Sea observations is due to the relatively large convective turbulent vertical velocity (due to a strong air-lake temperature difference) and its influence on the momentum flux. Even with the large turbulent vertical velocity component, these horizontal fluxes are small compared to the vertical turbulent energy fluxes. The vertical energy transport, due to both heating from below and cooling from above, dominates any horizontal transport in the Type I CTBL.

The water vapor flux,  $\bar{w'q'}$ , (Fig 4.24) also shows the strong influence of thermal convection on the moisture transport in the CTBL. The maximum upward transport in the sub-cloud layer is found near the surface of the CTBL. The upward flux decreases very slightly with height, as the amount of vapor and the upward vertical velocity remain high through the sub-cloud layer of the CTBL. Within the well-mixed cloud layer, the maximum upward vapor transport is found near the cloud bases. The amount of upward transport decreases in the upper cloud layer to almost zero at the cloud top. The second upward transport maximum in the cloud layer results from a local maximum in the amount of water vapor near the cloud bases. This vapor maximum is caused by both the upward transport of water vapor from the lake, and by the weak downward transport of water vapor from the cloud tops by entrainment instability. The decrease in moisture transport in the upper levels of the cloud layer is the result in a decrease in the amount of water vapor present, and

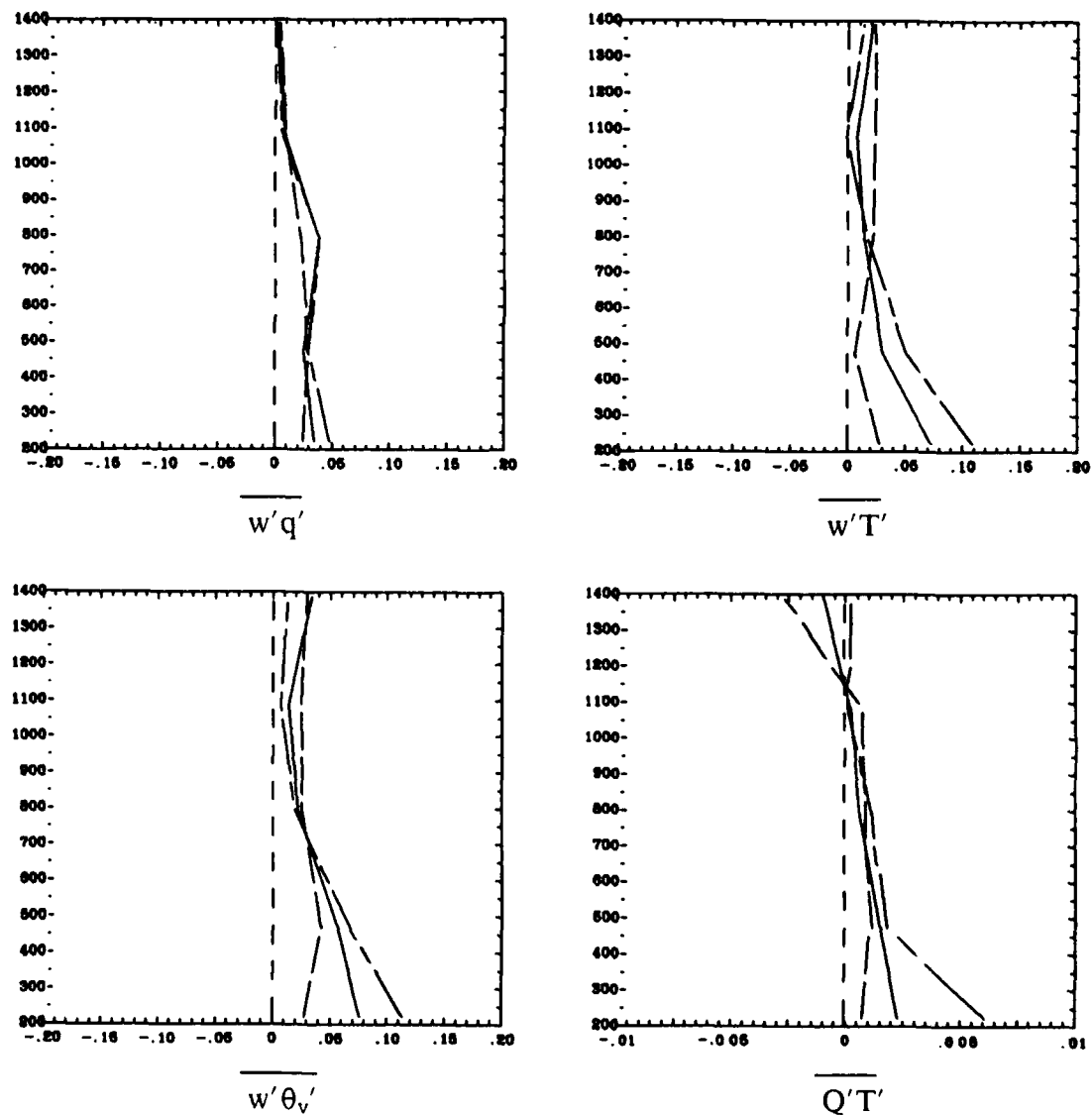


**Figure 4.24** Measured covariances for heat and moisture. The dashed lines represent the segments from 61-66 km and 66-71 km, respectively. The solid line represents the 61-77 km average. Note the different scale on the  $\bar{Q}'\bar{T}'$  plot.

the presence of weak downward vertical velocity at the top of the CTBL. The amount of water vapor decreases near the cloud tops as the upward moving air parcels cool, and the vapor condenses into liquid water. The amount of liquid water increases as the water vapor in the air parcels condenses, and reaches a maximum in the upper cloud layer. At the very top of the clouds the amount of liquid water decreases, as the entrainment process causes evaporative cooling of air parcels. These parcels sink down to the cloud bases to increase the specific humidity values there. These results correspond to the profiles of the well-mixed cloud layer for both observations (Nicholls, 1984), and for a 3-D numerical model (Deardorff, 1980a), of a Type II CTBL. In the sub-cloud layer, the strong thermal forcing caused a stronger moisture flux in the Type I CTBL profiles than were found in the Type II CTBL observations or model results.

The temperature flux,  $\overline{w'T'}$ , also shows the strong low-level thermal forcing from the lake. The maximum upward heat flux is found at the CTBL surface, where the ambient temperature values are warmest. The strength of the upward heat flux decreases with height through the sub-cloud layer, and reaches its minimum sub-cloud value at the cloud base height. The upward heat flux continues to decrease with height in the lower cloud layer, then increases with height near the cloud tops where entrainment instability, radiational cloud-top cooling, and weak downward vertical velocity combine to form an increased upward heat flux.

The buoyancy flux,  $\overline{w'\theta_v'}$ , is at its strongest near the bottom of the CTBL and decreases to a minimum value at the cloud base level. The buoyancy flux continues to decrease with height in the well-mixed cloud layer, and reaches a minimum in the middle of the layer. Near the top of the CTBL, the weak downward motion of evaporatively-cooled air parcels causes the buoyancy flux to again increase with height to a secondary maximum. The Type II CTBL profiles are dominated by

evaporative cooling process, with a neutral or downward buoyancy flux in the sub-cloud layer and a strong upward flux in the cloud layer.

The covariance between moisture and temperature,  $\overline{Q'T'}$ , is very weak for all three profiles. The maximum covariance between heat and moisture occurs at the surface of the CTBL, where the air parcels are both moist and warm. The air parcels remain warm and moist throughout most of the CTBL. The covariance becomes slightly negative at the top of the CTBL, where the air parcels with high humidity are relatively cool, compared to the warm, dry air parcels entrained from the inversion layer.

In summary, these fluxes and covariances show that low-level thermal forcing, as expected, is the main engine driving the vertical transport of heat, moisture and momentum in the Type I CTBL. The upward moving air parcels are warm, moist, and unstable through most of the CTBL. The effects of radiational cooling and the entrainment of air from the inversion layer, however, do have locally important effects on the properties of the air parcels and the turbulent transfers within the well-mixed cloud layer of the CTBL. Warm, dry air parcels are entrained into the cloud tops and acquire water vapor through evaporative cooling. The downward moving air parcels in the upper cloud layer are cool, moist and unstable. As these air parcels sink, they also drag along warm, dry inversion layer air in their wake into the lower cloud levels. This inversion air acts to dissipate the cloud bands (see Deardorff, 1980b). In the case of the Type II CTBL, this entrainment instability is what breaks up the statocumulus cloud decks. In the Type I CTBL, the thermal forcing is so dominant that the entrainment instability has little effect on the CTBL in general. While the dynamics within the well-mixed cloud layer have similarities between the Type I and Type II CTBL's, numerical models of the Type II CTBL are of limited value in studying the Type I CTBL. Any model of a Type I CTBL must include the

thermal forcing at the bottom boundary and its effect on the transport of heat, moisture and momentum in the sub-cloud as well as in the cloud layer. While there are different processes occurring in the sub-cloud layer as opposed to the cloud layer, the strong surface heating makes it impossible to treat the cloud and sub-cloud layers as decoupled, as they sometimes are in the Type II CTBL (Nicholls, 1984). The vertical fluxes of liquid water would also give important insights into the dynamics of this CTBL, but instrument problems limited the amount of liquid water data available in this case study, as will be shown in the next chapter.

## 5. CLOUD PHYSICS

### 5.1 Precipitation Processes

The momentum, heat and moisture fluxes calculated in the previous chapter underscored the dominant role played by strong low-level thermal forcing in the generation of vertical turbulent kinetic energy (TKE) in the Type I CTBL. The fluxes also indicated that diabatic processes, such as evaporation caused by entrainment instability and radiative cooling play an important role in generating vertical TKE within the well-mixed cloud layer at the top of the CTBL. Another important diabatic process that has not yet been addressed is condensation. As air parcels rise to the top of the CTBL, they cool and water vapor in the parcels condenses into liquid water. Nicholls (1984) found that the liquid water droplets in the upper cloud levels undergo gravitational settling. Once the droplets fall far enough into the cloud, they will evaporate again and increase the water vapor content and buoyancy in the lower part of the cloud layer. This gravitational flux of liquid water helps control the liquid water content of clouds and affects the stability of the CTBL. The 'drizzle flux' can aid in the generation of vertical TKE within the cloud layer by increasing the buoyancy flux ( $w'\theta'_v$ ).

In this chapter, data from the Johnson-Williams liquid water detector (J-W probe) and two droplet spectrometer probes – the FSSP and the 1D-P (200Y) were used to examine the liquid water content (LWC) and droplet concentrations. The same methodology mentioned in Chapter 4 were used on these data to construct vertical cross-sections that reveal the structure of the microphysical properties of the clouds in this Type I CTBL. Table 5.1 lists the specifications of the instruments used

**Table 5.1** The instrument specifications for the microphysical data collected by the NCAR King Air and Queen Air research aircraft.

### PARTICLE SAMPLING INSTRUMENTATION (1Hz)

AIRCRAFT	SAMPLING DEVICE	RANGE	PARTICLE CONCENTRATION	SLWC/ICE (g/m <sup>3</sup> )/(cm <sup>-3</sup> )	TEMPERATURE RANGE
QUEEN AIR	FSSP	.5 to 45 $\mu\text{m}$	< 700 per cm	<.15 g/m <sup>3</sup>	-8 to -18.4°C
QUEEN AIR	FSSP	.5 to 9 $\mu\text{m}$	< 700 per cm	<.08 g/m <sup>3</sup>	-8 to -18.4°C
QUEEN AIR	FSSP	10 to 45 $\mu\text{m}$	< 35 per cm	< 35 per cm <sup>3</sup>	-8 to -18.4°C
KING AIR	Johnson (averaged)	0 to 5 g/m	-----	<.13 g/m <sup>3</sup>	-15 to -19.3°C
QUEEN & KING AIR	200Y	300 to 4500 $\mu\text{m}$	< 11 per cm	< 11 per cm <sup>3</sup>	-8 to -19.3°C

Levels 4 and 5 are in the cloud layer. The FSSP measurements of particles < 10 $\mu\text{m}$  assumes all particles are supercooled water droplets. The FSSP measurements for particles > 10  $\mu\text{m}$  assumes all particles are ice crystals, broken crystals/snowflakes (Hobbs and DeePak). The 200Y measurements assume all particles are very small snowflake size particles. SLWC stands for supercooled liquid water content (in cloud).

in the data collection. The most common instrument used to measure the liquid water content is the J-W probe, a hot-wire LWC meter. J-W data are available for the top level (King Air flight) only. The data from the rest of the flight levels (Queen Air flight) were unusable due to instrument drift, a common problem with J-W data. While the FSSP doesn't directly measure LWC, it is possible to estimate the LWC for the other flight levels by using the FSSP data. The FSSP measures the concentration of small particles (radius between 3 and 45  $\mu\text{m}$ ), every second (1Hz data). The following equation can be used to calculate the liquid water content from the droplet concentration:

$$q_L = \frac{4}{3} \pi \rho_L \int_{1.5\mu\text{m}}^{22.5\mu\text{m}} r^3 n(r) dr \quad (5.1)$$

where  $q$  = liquid water content ( $\text{g}/\text{m}^3$ )  
 $n(r)$  = particle concentration (per  $\text{cm}^3 \mu\text{m}$ )  
 $r$  = mean particle radius ( $\mu\text{m}$ )  
 $\rho_L$  = density of liquid water ( $\text{g}/\text{m}^3$ )

FSSP data are available for the bottom four levels (Queen Air flight), but not for the top level (King Air flight) due to instrument problems. To construct any kind of LWC cross-section, it was necessary to use both the J-W and FSSP data. In order to use the FSSP liquid water values, it was also necessary to assume that all the particles collected are water droplets and not ice crystals. The validity of this assumption will be discussed shortly. There was also 1D-P (200Y) data available for all five levels, which gave information about the larger particles ( $300 - 4500\mu\text{m}$ ). In this case of wintertime statocumulus, we would expect to see low liquid water contents and lots of ice crystals. All the precipitation reported during the flight was snow.

The first step in examining the cloud microstructure was to try to locate the cloud layer of the CTBL more precisely. The data examined in the previous chapter

indicate that the base of the cloud layer is located above the bottom three flight levels (at approximately 800m). The height of the cloud bases rises from west to east as the CTBL depth increases. The relative humidity cross-section (Fig 5.1) can be used to determine the cloud location by using the 90% RH contour. The cloud base is approximately 400m above sea level at the extreme western end of the CTBL, gradually rising to approximately 900m at the Michigan end of the cross-section. The mean cloud base height over the entire cross-section is approximately 770m. The top of the CTBL and the inversion layer are also present at the western half of the RH cross-section (8 – 40km). There is also evidence of the mesoscale wave feature found in the other cross-sections. This feature is marked by protrusions of higher RH down into the sub-cloud layer every 20km. There are also some areas along the top of the CTBL (40 – 60km) showing lower RH values, where it's possible that the entrainment of dryer inversion air is occurring.

Figure 5.2 shows the liquid water cross-sections that were created using the J-W and FSSP data. The first profile (Fig 5.2.1) shows the LWC based on J-W data for the top level, and FSSP for the bottom four levels – assuming that all particles measured by the FSSP were liquid water. The maximum liquid water values are found in the upper part of the cloud layer, as expected. In the western part of the cross-section where the top of the CTBL can be seen (8 – 40km), the LWC values begin to decrease with height under the influence of entrainment from the inversion. The liquid water values are low in this cross-section, with maximum values of only  $.1\text{ g/m}^3$  in the upper levels of the cloud layer. There are also high LWC values extending down into the sub-cloud layer, which correspond to the larger precipitation bands. The large precipitation band associated with the Michigan land breeze convergence front (90 – 105km) is the largest, followed by the enhanced Wisconsin shore precipitation band (12 – 24km).

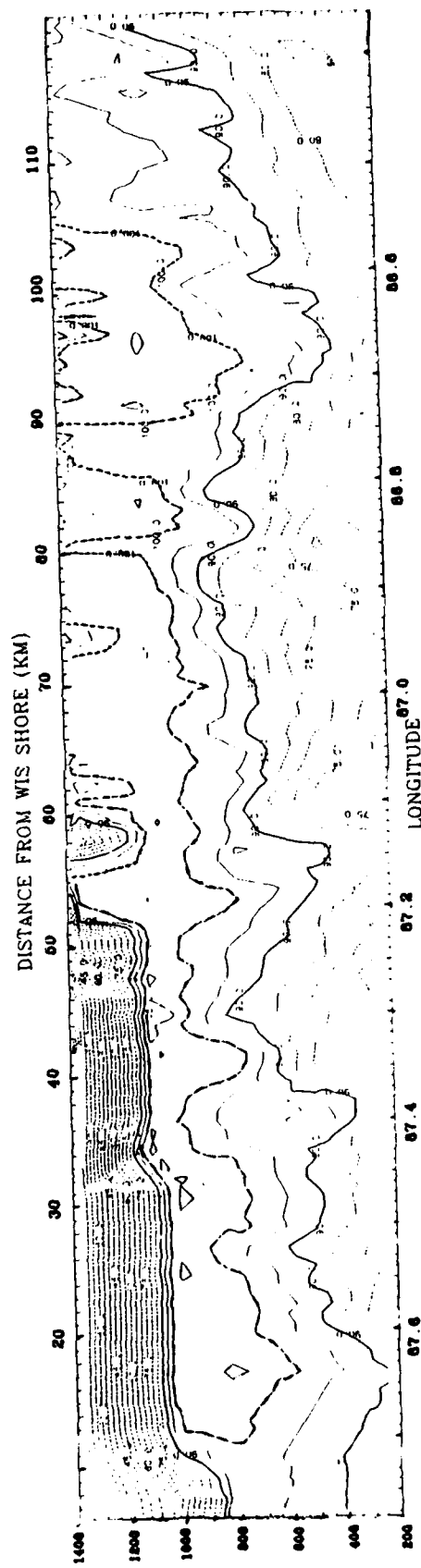


Figure 5.1 Vertical cross-section for relative humidity (%) based on the five research aircraft flight levels over Lake Michigan on 10 January 1984. Contour intervals are 5%.

Figure 5.2

Vertical cross-sections for liquid water content, for particles of diameter  $1.5 - 4.5 \mu\text{m}$  ( $\text{g}/\text{m}^3$  - top), for particles of diameter  $< 10 \mu\text{m}$  ( $\text{g}/\text{m}^3$  - middle), and for particles of diameter  $\geq 10 \mu\text{m}$  ( $\text{g}/\text{m}^3$  - bottom), based on the five research aircraft flight levels over Lake Michigan on 10 January 1984. Contour intervals are .01  $\text{g}/\text{m}^3$ .

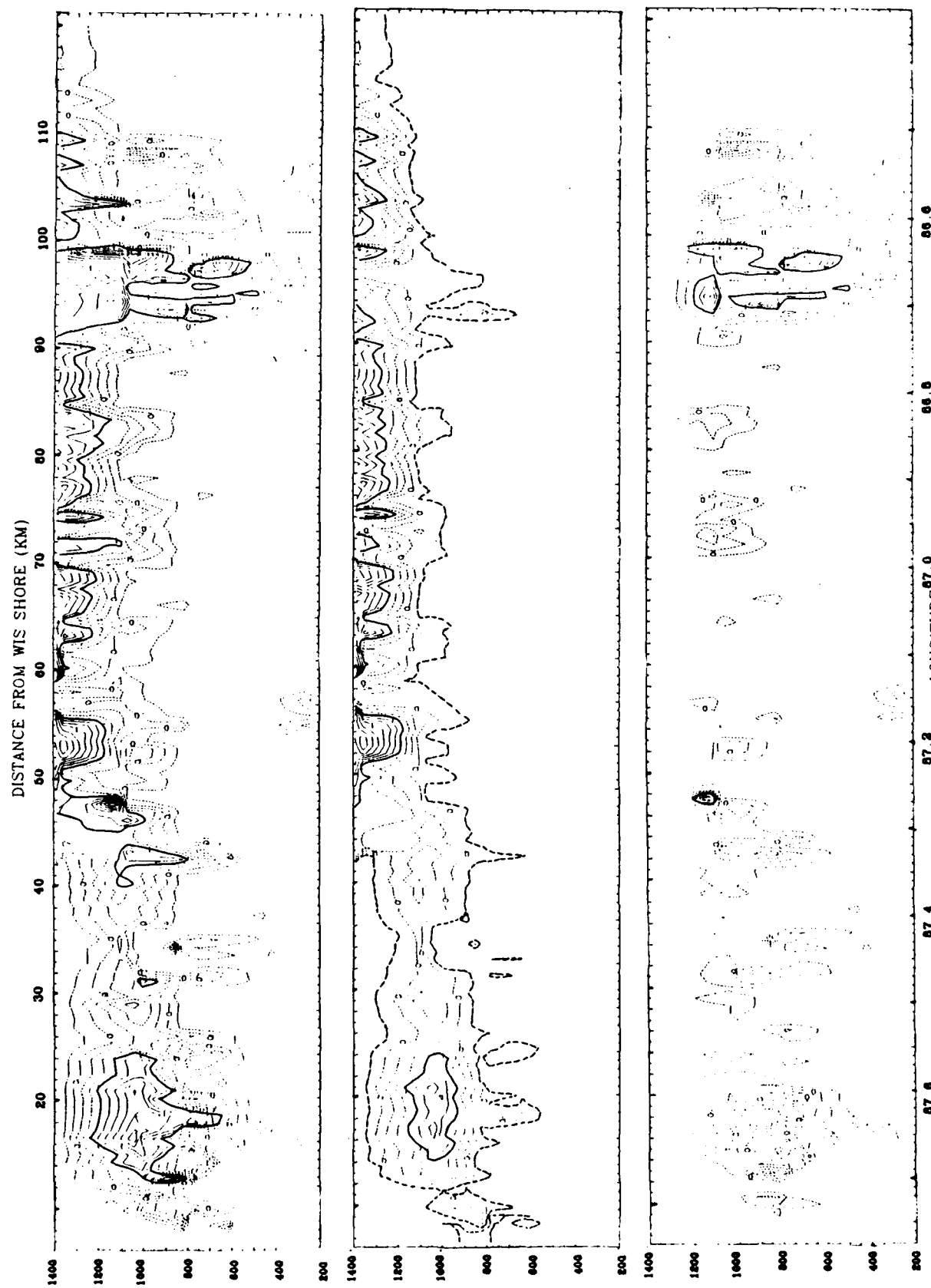


Figure 5.2

The log for flight mission # 85 mentioned that the only precipitation that occurred over Lake Michigan that day was in the form of snow. The high LWC values calculated from the FSSP data are obviously overestimating the amount of liquid water present. The temperatures reported in the CTBL are well below freezing ( $-15$  to  $-19^{\circ}\text{C}$ ), and it is likely that many of the particles assumed to be water droplets are actually ice crystals. The 2D-C and 2D-P data available for a portion of the top level (not shown), indicate that the LWC is low in these clouds and the number of ice crystals are high. Given the type of aircraft data available in this case study, it is impossible to make a clear distinction between water droplets and ice crystals at these low temperatures.. However, it is possible to separate the FSSP concentration data into two populations based on the particle size. Hobbs and Deepak (1981) noted that the diameters of ice crystals typically range between  $10\ \mu\text{m}$  and  $1\ \text{mm}$ , so the  $10\ \mu\text{m}$  diameter size was used to separate the FSSP concentrations into two groups. The first group consists of particles with diameters less than  $10\ \mu\text{m}$ , and the second group consists of particles with diameters greater than or equal to  $10\ \mu\text{m}$ .

Figures 5.2.2 and 5.2.3 show the liquid water content calculated for each population. In Figure 5.2.2, the liquid water values for the top level are again from the J-W probe. The four lower levels are the FSSP liquid water values calculated from those particles with diameters less than  $10\ \mu\text{m}$ . These liquid water values are only slightly less than those in Figure 5.2.1, and those maximum values associated with the main snow bands are now gone. The liquid water content cross-section calculated from this population of smaller particles shows the location of the well-mixed cloud layer accurately. Figure 5.2.3 shows the liquid water content calculated from the FSSP concentrations of particles with diameters greater than or equal to  $10\ \mu\text{m}$ . There are no FSSP data available for the top flight level, so only the four lower levels are represented here. This cross-section shows only indirect

evidence of the cloud layer, but does show clearly those particles large enough to be affected by gravity. These larger particles are likely to be single ice crystals or fragments of snowflakes that have broken apart in the turbulence of the CTBL. This population of larger particles shows the locations of the main snow bands at 90 km, 40 km, and 20 km quite well. However, it is still difficult to make a distinction between ice crystals and water droplets within the cloud layer. It would not be possible to use these liquid water content data to calculate an accurate gravitational settling flux of liquid water in this CTBL.

Figure 5.3 shows the actual FSSP particle counts that were used to calculate the liquid water contents. There are no FSSP data available for the top flight level. Figure 5.3.1 shows the total FSSP particle concentrations. The maximum concentrations ( $650 / \text{cm}^3$ ) are found in the upper levels of the cloud layer, and on the west side of the CTBL where the CTBL is the most shallow (8 – 40km). There are two contributing factors to this horizontal difference in the concentrations. The first is that the heavier precipitation occurring on the eastern side of the lake has been washing out a greater number of particles than has been the case on the western side of the lake. The second factor is the increase in the CTBL depth from west to east. On the western side of the lake the entire CTBL is contained within the cross-section, while on the eastern side of the lake the top of the CTBL is above the area covered by the cross-section. The upper cloud levels, where the maximum concentrations are found, can be seen on the western half of the cross-section but not on the eastern half. We have no data on what the cloud-top concentrations are in the eastern half of the CTBL.

The concentrations of smaller particles ( $d < 10\mu\text{m}$ ) are shown in Figure 5.3.2. The concentrations here are only slightly less than the total concentration, indicating that a majority of the particles in the CTBL are very small. The greatest difference

Figure 5.3 Vertical cross-sections for FSSP concentrations, for particles of diameter  $1.5 - 4.5 \mu\text{m}$  ( $\text{cm}^3$  – top), for particles of diameter  $< 10 \mu\text{m}$  ( $\text{cm}^3$  – middle), and for particles of diameter  $\geq 10 \mu\text{m}$  ( $\text{cm}^3$  – bottom), based on the five research aircraft flight levels over Lake Michigan on 10 January 1984. Contour intervals are: 50  $\text{cm}^{-3}$  (top and middle), and 5  $\text{cm}^{-3}$  (bottom).

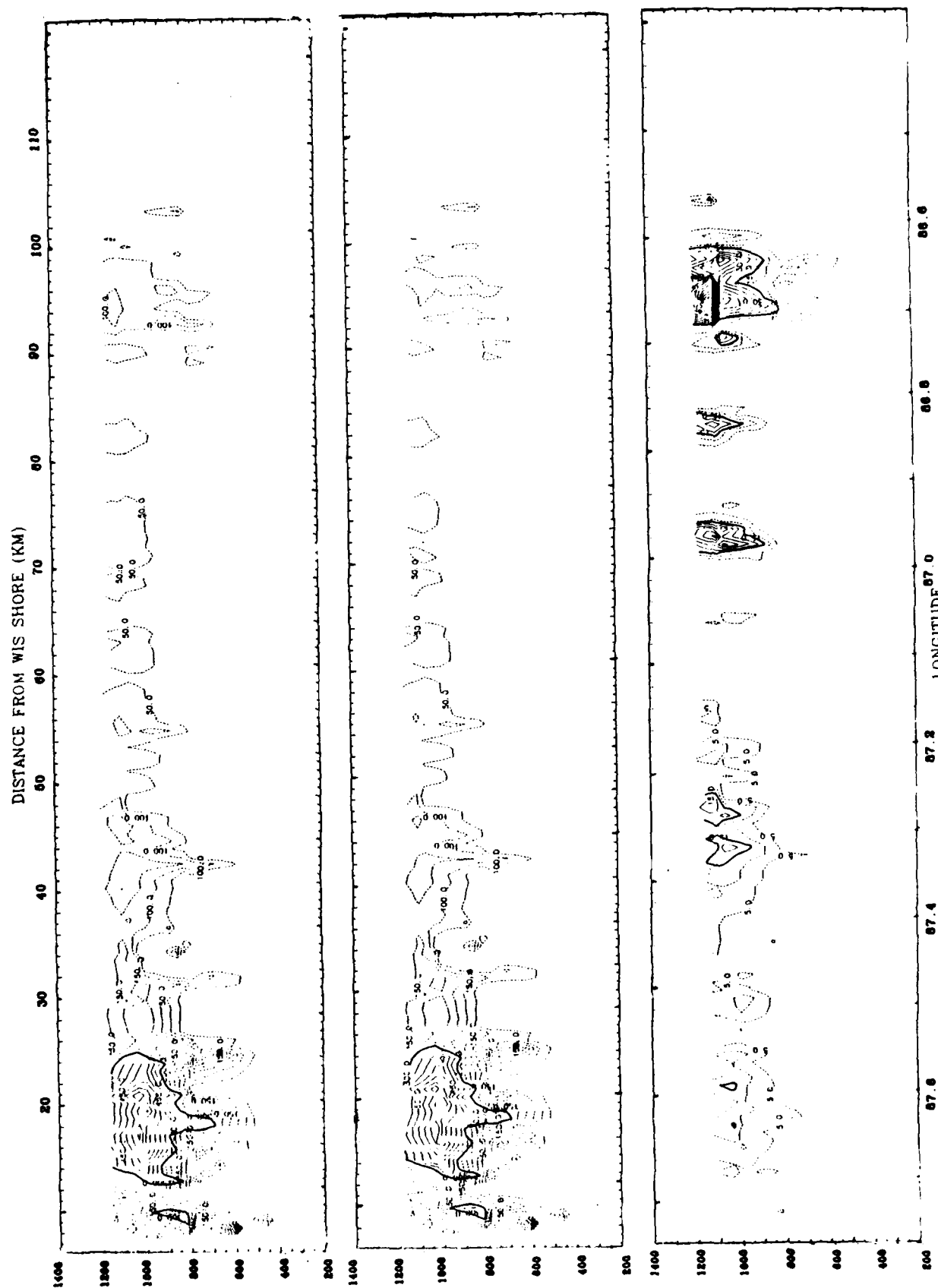


Figure 5.3

between these concentrations and the total concentrations occur on the eastern side of the lake, particularly in the Michigan land breeze precipitation band (90 – 105km). The concentrations associated with the Wisconsin convergence band are virtually unchanged between the two cross-sections. The larger particle concentrations ( $d \geq 10\mu\text{m}$ ) are in Figure 5.3.3. The concentrations here are an order of magnitude lower than the total concentrations or the small particle concentrations. The concentrations are also less horizontally uniform, and show the locations of some of the main precipitation bands. The largest concentrations ( $50 / \text{cm}^3$ ) are found in the Michigan land breeze convergence band (90 – 105km). Other maxima are present at approximately 20km intervals. The other large areas of high concentrations are the Wisconsin convergence band (12 – 24km), and the mid-lake snow band (40 – 60km). It is likely that some of the snowflakes in these precipitation bands may be larger than the maximum radius of 45um that was measured here. But these detectable particles may be the result of larger snowflakes breaking due to turbulence.

The last microphysical data to be examined are the 1D-P (200Y) particle data, which consists of the larger-sized particles (see table 5.1). Figure 5.4 shows the cross-sections of the concentrations and mean particle diameter sizes. Since these larger particles are likely to be ice crystals and snowflakes, it would be misleading to calculate any liquid water content here. The maximum concentrations seen here (Fig 5.4.1) are found in the lower levels of the cloud layer and in the main precipitation bands. This difference from the FSSP particles is explained by the fact that these particles are several orders of magnitude larger than the FSSP particles, and are large enough to fall rapidly.

The largest concentrations and the largest-sized particles (Fig 5.4.2) are found in the Michigan land breeze band (90 – 110km) and the Wisconsin convergence band (10 – 22km). These larger particles follow an opposite pattern to the FSSP data

Figure 5.4 Vertical cross-sections for particle concentrations ( $/cm^3$  - top), and the mean diameters ( $\mu m$  - bottom), for particles of diameter  $300 - 4500 \mu m$  from 1D-P (200Y) data, based on the five research aircraft flight levels over Lake Michigan on 10 January 1984. Contour intervals are:  $.1 /cm^3$  (top), and  $500 \mu m$  (bottom).

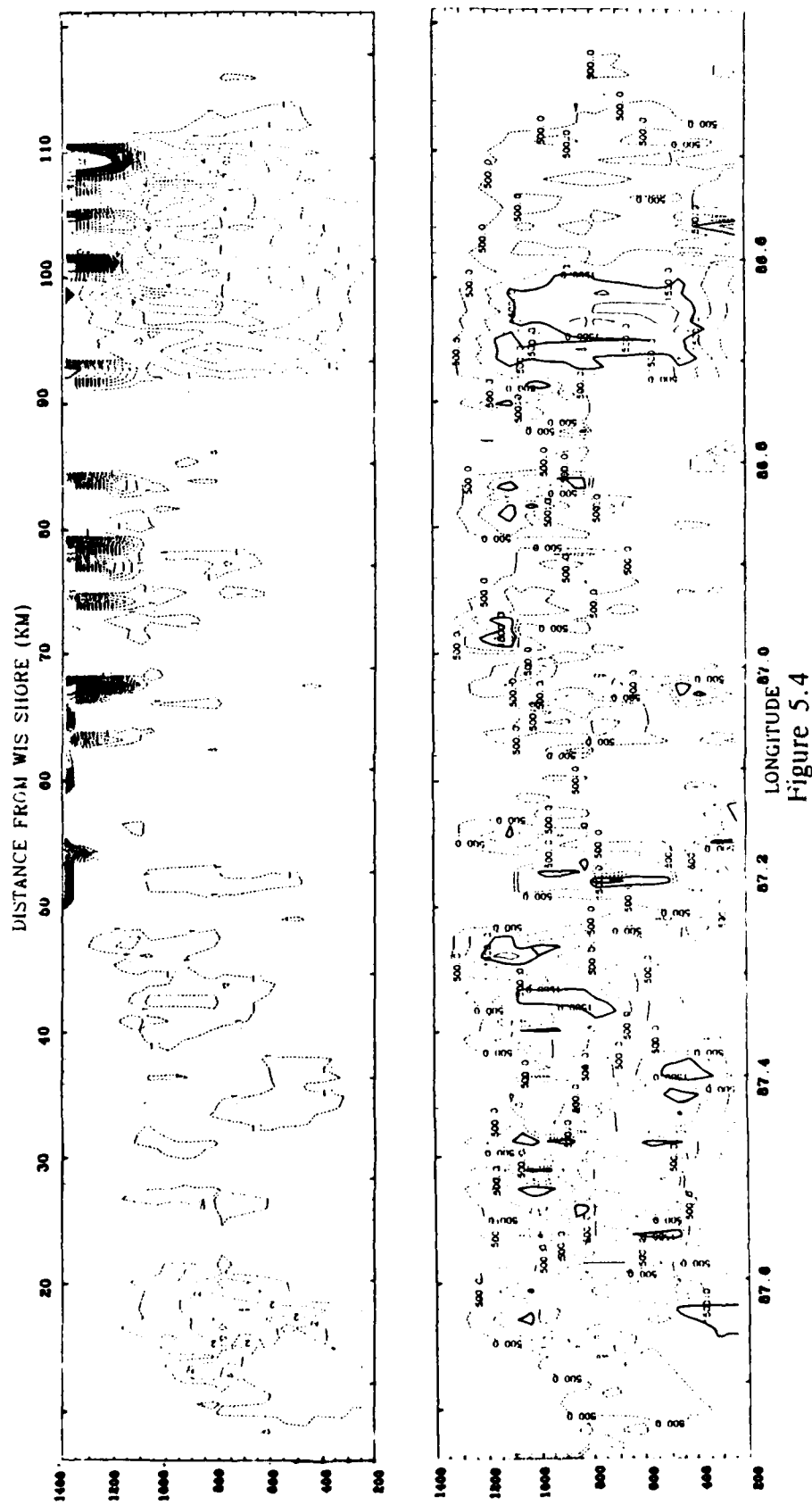


Figure 5.4

in that the maximum concentrations in Fig 5.4 are found at the eastern end of the lake, and in the middle levels of the cloud layer. The 200Y particle concentrations are also much less horizontally uniform within the cloud layer than the FSSP data were. When comparing the locations of the maximum particle sizes versus the maximum concentrations, the largest particles are found to be below and to the west of the maximum concentrations in the cloud layer. This difference is explained when the strong easterly return flow in the upper CTBL is taken into account. In the lower CTBL, the locations of the largest particles correspond to locations of the maximum concentrations.

The lack of reliable microphysical data in this case study, especially the 2D-P and 2D-C data, makes it impossible to examine the cloud microphysical characteristics in any more detail. Without detailed liquid water and ice crystal data it's impossible to estimate the gravitational flux of liquid water, or how radiation and entrainment processes change the LWC and the possible effect of changes in the LWC on the structure and stability of the CTBL. The conclusions that can be drawn from these data are about the mean structure of the CTBL, rather than about any microscale fluctuations of liquid water in the cloud layer.

## 6. SUMMARY AND CONCLUSIONS

Meteorological data, sampled at 20Hz frequency from research aircraft flights, were used to study the structure of a Type I CTBL that formed as a result of air mass modification by a CAO over Lake Michigan on 10 January 1984. Surface and upper air data were used as a source of information to describe the synoptic scale conditions that accompanied the event.

The surface and upper air data for 10 January 1984 showed a large continental polar air mass over the Midwest with strong north-northwest flow over the Great Lakes region. Strong cold air advection aloft enhanced the CAO. This northerly flow over Lake Superior and Lake Michigan caused the formation of a Type I CTBL over the relatively warm water. The thermal forcing was sufficient to cause 2-D cloud streets to form over both lakes. Aircraft data collected over Lake Michigan showed that the CTBL extended across the entire east-west traverse of the lake, with a gradual increase in the depth of the CTBL from west to east due to a difference in fetch. Two NCAR research aircraft flew several legs across the lake at 43°N latitude, collecting data from five separate levels within the CTBL. These multiple levels provided a unique opportunity to study in detail the structure of a Type I CTBL. The strong northerly flow seen in the aircraft data made possible the assumption of a north-south steady-state (parallel to the cloud streets), during the 1 hour and 50 minute time period of the flights. This assumption allowed vertical cross-sections of the CTBL to be constructed from the aircraft data.

The raw aircraft data plots, and the cross-sections constructed from them, showed a complex CTBL structure with many features. The depth of the CTBL

almost doubles from west to east across the lake. The contours of specific humidity define the shape of the CTBL. A strong off-shore flow from lower Michigan and a band of enhanced convection marking the boundary of this Michigan land breeze dominate the eastern half of the CTBL cross-section. Another enhanced precipitation band is present at mid-lake, and the off-shore flow from Wisconsin creates an enhanced band of convection near the Wisconsin shore. There are also indications of smaller mesoscale features, possibly related to the 2-D cloud streets, at a length scale of approximately 20km. The features found in this particular CTBL, particularly the Michigan land breeze and its convergence band, indicate that when considering a Type I CTBL over a relatively small body of water (such as Lake Michigan) the local geography must be considered. The off-shore flow found along both lakeshores imposes lateral boundary conditions on the CTBL.

A large sample from the homogenous portions of the CTBL was taken for spectral analysis. Three different length scales were found in the spectral results. The Basic Convective Mode (BCM), as defined by Ross and Agee, was present at a wavelength of approximately 3km. This wavelength also agrees with the results of Kaimal et. al. (1976), where the spectral peak was present at  $1.5Z_i$  ( $Z_i$  is approximately 2000m). The next length scale present was at a wavelength of approximately 10km. This peak was most pronounced in the  $v$  component of wind, and probably represents the width of the 2-D cloud streets. The largest length scale present was the Mesoscale Cellular Convection mode (MCC) at an approximate wavelength of 30km. The MCC wavelength, which indicates the distance between the 2-D cloud streets, was most pronounced in the temperature spectra. In addition to these mesoscale length scales, the smaller wavelengths in the inertial subrange showed a large amount of turbulent kinetic energy (TKE) present in the CTBL. The strongest turbulence was found in the wind component spectra, while the turbulent energy in

temperature and specific humidity data were an order of magnitude smaller. The vertical velocity, temperature, and specific humidity spectra showed the maximum amount of vertical TKE at the bottom of the CTBL. The amount of vertical TKE decreased with height through most of the CTBL. The exception to this was at the very top of the CTBL, where the amount of vertical TKE in the temperature spectra increased to a secondary maximum. These results suggest that two separate processes are at work here. The transfer of heat and moisture from the lake generates large amounts of vertical TKE in the lower part of the CTBL. At the top of the CTBL, diabatic processes involving the turbulent mixing of air between the CTBL and relatively warmer inversion layer are responsible for generating a smaller amount of vertical TKE.

Moisture, heat, and momentum fluxes were calculated for a representative sample of the CTBL in order to examine the turbulent transports in a Type I CTBL in detail. The results were compared to observations and model results for a Type II CTBL. The vertical fluxes of TKE, momentum, heat and moisture calculated here were all an order of magnitude larger than those observed by Nicholls (1984), and those obtained from model results by Deardorff (1980a) and Moeng (1986), for the Type II CTBL. The flux profiles calculated for a Type I CTBL showed that strong thermal forcing drives the convection, which resulted in the maximum vertical fluxes of heat, moisture and momentum occurring near the bottom of the CTBL in the sub-cloud layer. This flux maximum is only weakly present in those models of the Type II CTBL with weak thermal forcing (Deardorff), and is replaced by a flux minimum in those models with no thermal forcing (Moeng). The vertical flux profiles also showed a secondary transport maximum in the lower part of the cloud layer. This maximum is the result of diabatic processes at the top of the CTBL, such as radiative cloud-top cooling, entrainment instability caused by evaporative cooling,

and a gravitational flux of liquid water. All the observational and model results for the Type II CTBL show the maximum vertical fluxes in the cloud layer as a result of these diabatic processes driving the convection in the CTBL.

The correlation between temperature and specific humidity was surprisingly weak. The turbulent fluctuations in the temperature, as compared to the turbulence in the velocity components, were relatively weak. This fact, as well as the relative lack of turbulent humidity fluctuations within the CTBL sample, were the cause of the small values. The correlation between T and Q was positive through most of the CTBL, indicating that the moist air parcels are warm as well. The correlation becomes negative at the top of the CTBL, where the dry air parcels from the inversion are warm, and the moist air parcels from the CTBL are relatively cold.

The differences in the vertical flux profiles between the Type I and Type II CTBL show an important difference in the turbulent transports between the two types of CTBL. In the Type I CTBL, thermal forcing from below is the dominant factor in the turbulent transports, and causes the turbulent flux profiles to show the maximum turbulent transport at the bottom of the CTBL, and the magnitude of the fluxes to be an order of magnitude larger than those in the Type II CTBL. The Type II CTBL is driven by the relatively weak diabatic processes at the cloud tops, which play only a secondary role in the turbulent transports of a Type I CTBL. Turbulent transport models for the Type I CTBL must incorporate both strong thermal forcing from below and cloud-top diabatic processes to give an accurate representation of the vertical fluxes.

Efforts to examine the microphysical processes with respect to liquid water were hampered by lack of data due to instrument problems. Liquid water cross-sections were constructed by estimating the liquid water content by use of the FSSP droplet concentrations. Those cross-sections indicated that the liquid water

content of the clouds was low (.1 g/kg), and that the concentrations of ice crystals were high. The largest concentrations of droplets and small ice crystals were found in the shallow section of the CTBL (near the Wisconsin shore), near the cloud tops. The maximum concentrations of large ice crystals and snowflakes occurred in the deeper section of the CTBL (near Michigan), in the larger snow bands. The lack of exact liquid water data made it impossible to calculate the turbulent liquid water fluxes.

**LIST OF REFERENCES**

### LIST OF REFERENCES

Agee, E.M. and T.S. Chen, 1973: A model for investigating eddy viscosity effects on mesoscale cellular convection. *J. Atmos. Sci.*, **30**, 180-199.

Agee, E.M., T.S. Chen and K.E. Dowell, 1973: A review of mesoscale cellular convection. *Bull. Amer. Met. Soc.*, **54**, 1004-1012.

Agee, E.M., 1987: Mesoscale cellular convection over the oceans. *Dyn. Atmos. Oceans*, **10**, 317-341.

Agee, E.M., and S. Gilbert, 1989: Aircraft investigation of mesoscale convection over Lake Michigan during the 10 January 1984 cold air outbreak. *J. Atmos. Sci.*, (in press).

Benard, H., 1901: Les tourbillons cellulaires dans une nappe liquide transportant de la chaleur par convection en régime permanent. *Ann. Chim. Phys.*, **23**, 62-144.

Braham, R.R., and R.D. Kelly, 1982: Lake-effect snow storms on Lake Michigan. *Cloud Dynamics*, Agee and Asai ed., D. Reidel pub., 87-102.

Braham, R.R., 1986: Cloud and motion fields in open-cell convection over Lake Michigan. *Proc. 23rd Conf. Radar Meteor. and Conf. on Cloud Phys. Snowmass, CO Sept 22-26*.

Brümmer, B., 1985: Structure, dynamics and energetics of boundary layer rolls from Kon Tur aircraft observations. *Contrib. Atmos. Phys.*, **58**, 237-254.

Bunker, A.F., 1960: Heat and water vapor fluxes in air flowing southward over the western North Atlantic Ocean. *J. Met.*, **17**, 52-63.

Chandrasekhar, S., 1957: Thermal convection. *Daedalus*, **86**, 4, 325-339.

Christopherson, D.G., 1940: Note on the vibrations of membranes. *Quart. J. Math.*, **11**, 63-63.

Curry, J.A., 1983: On the formation of continental polar air. *J. Atmos. Sci.*, **40**, 2278-2292.

Deardorff, J.W., 1980a: Stratocumulus-capped mixed layer derived from a three dimensional model. *Bdry. Layer Met.*, **18**, 495-527.

Deardorff, J.W., 1980b: Cloud top entrainment instability. *J. Atmos. Sci.*, **37**, 131-147.

Fiedler, B.H., 1984: The mesoscale stability of entrainment into cloud-topped mixed layers. *J. Atmos. Sci.*, **41**, 92-101.

Friehe, C.A., R.L. Grossman and Y. Pann, 1986: Calibration of an airborne Lyman-Alpha hygrometer and measurement of water vapor flux using a thermoelectric hygrometer. *J. Atmos. and Oceanic Tech.*, **3**, 299-304.

Helfand, H.M., and E. Kalnay, 1983: A model to determin open or closed cellular convection. *J. Atmos. Sci.*, **40**, 631-650.

Hobbs, P.V., and A. Deepak, 1981: *Clouds: their formation, optical properties, and effects*. Academic Press Inc.

Hubert, L.F., 1966: Mesoscale cellular convection. *Rept. 37*, Meteorological Satellite Laboratory, Wasington, D.C., 68pp.

Kaimal, J., J. Wyngarrd, O. Cote, V. Izumi, S. Coughey, and C. Readings, 1976: Turbulent structure in the convective boundary layer. *J. Atmos. Sci.*, **33**, 2152-2169.

Kelly, R.D., 1984: Horizontal roll and boundary layer interrelationships observed over Lake Michigan. *J. Atmos. Sci.*, **41**, 1816-1826.

Kruger, A.F., and S. Fritz, 1961: Cellular cloud patterns revealed by TIROS I. *Tellus*, **13**, 1-7.

Krishnamurti, R., 1970a: On the transition to turbulent convection. Part 1: The transition from 2-D to 3-D flow. *J. Fluid Mech.*, **42**, 295-307.

Krishnamurti, R., 1970b: On the transition to turbulent convection. Part 2: The transition to time-dependent flow. *J. Fluid Mech.*, **42**, 309-320.

Krishnamurti, R., 1975: On cellular cloud patterns. Part 3: Applicability of the mathematical and laboratory models. *J. Atmos. Sci.*, **32**, 1373-1383.

Kuo, H.L., 1979: Power laws of high Rayleigh number convection. *Bound. Layer Met.*, **17**, 29-39.

LeMone, M.A., 1973: The structure and dynamics of horizontal rolls in an unstable planetary boundary layer. *J. Atmos. Sci.*, **30**, 1077-1091.

LeMone, M.A., 1976: Modulation of turbulence energy by longitudinal rolls in an unstable planetary boundary layer. *J. Atmos. Sci.*, **33**, 1308-1320.

Lenschow, D.H., 1965: Airbourne measurements of atmospheric boundary layer structure. Studies of the Effects of Variations in Boundary Conditions on the Atmospheric Boundary Layer, Sec. 4, Final Rept., Contract DA-36-039-AMC-00878(E), Dept. of Met., University of Wisconsin, 147-208.

Lenschow, D.H., 1973: Two examples of planetary boundary layer modification over the Great Lakes. *J. Atmos. Sci.*, **30**, 568-581.

Lenschow, D.H., and P.L. Stephens, 1980: The role of thermals in the convective boundary layer. *Bdry. Layer Met.*, **19**, 509-532.

Lilly, D.K., 1968: Models of cloud-topped mixed layers under a strong inversion. *Quart. J. Roy. Met. Soc.*, **94**, 292-309.

Lyons, W.A., 1972: The climatology and prediction of the Chicago Lake Breeze. *J. Appl. Met.*, **11**, 8, 1259-1270.

Malkus, W.V.R., and G. Veronis, 1958: Finite amplitude cellular convection. *J. Fluid Mech.*, **4**, 225-260.

Mason, P.J., and R.J. Sykes, 1982: A 2-D numerical study of horizontal roll vortices in an inversion capped PBL. *Quart. J. Roy. Met. Soc.*, **108**, 801-823.

Miura, Y., 1986: Aspect ratios of longitudinal rolls and convection cells observed during cold air outbreaks. *J. Atmos. Sci.*, **43**, 26-39.

Moeng, C.-H., 1986: Large-eddy simulation of a stratus-topped boundary layer. Part 1: Structure and budgets. *J. Atmos. Sci.*, **43**, 2886-2900.

Nicholls, S., 1984: Dynamics of statocumulus; aircraft observations and comparisons with a mixed layer model. *Quart. J. Roy. Met. Soc.*, **110**, 783-820.

Orlanski, I., 1975: Rational subdivision of scales for atmospheric processes. *Bull. Amer. Met. Soc.*, **56**, 5, 527-530.

Palm, E., 1960: On the tendency toward hexagonal cells in steady convection. *J. Fluid Mech.*, **8**, 183-192.

Passarelli, R.E., and R.R. Braham, 1981: Role of the land breeze in the formation of Great Lakes snowstorms. *Bull. Amer. Met. Soc.*, **62**, 482-491.

Peace, R.L. Jr., and R.B. Sykes Jr., 1966: Mesoscale study of a lake-effect snow storm. *Mon. Wea. Rev.*, **94**, 495-507.

Pellew, A., and R.V. Southwell, 1940: On maintained convection motion in a fluid heated from below. *Proc. Roy. Soc., A*, **176**, 312-343.

Petterssen, S., 1956: *Weather analysis and forecasting*. Vol 2. McGraw Hill, 260 pp.

Randall, D.A., 1980: Conditional instability of the first kind upside-down. *J. Atmos. Sci.*, **37**, 125-130.

Rayleigh, O.M., 1916: On convection currents in a horizontal layer of fluid, when the higher temperature is on the underside. *Phil. Mag.*, Ser. **6**, 32, 529-546.

Rokosz, S.D., 1985: Modification of polar air masses over Lake Michigan. M.S. thesis, Purdue University, 216pp.

Ross, B., and E.M. Agee, 1985: Aircraft investigation of wintertime convective and non-convective boundary layers over the East China Sea. *J. Met. Soc. Japan*, **63**, 405-416.

Rothermel, J., and E.M. Agee, 1980: Aircraft investigation of mesoscale cellular convection during AMTEX 75. *J. Atmos. Sci.*, **37**, 1027-1040.

Rothermel, J., and E.M. Agee, 1986: A numerical study of atmospheric convective scaling. *J. Atmos. Sci.*, **43**, 1185-1197.

Schoenberger, L.M., 1984: Doppler radar observation of a land-breeze cold front. *Mon. Wea. Rev.*, **112**, 2455-2464.

Schoenberger, L.M., 1986a: Mesoscale features of the Michigan land breeze using PAM II temperature data. *Wea. and Forec.*, **1**, 127-135.

Schoenberger, L.M., 1986b: Mesoscale features of a midlake snow band. *Proc. 23rd Conf. Radar Met. & Conf. Cloud Phys.*, JP206-JP209.

Sheu, P.J., and E.M. Agee, 1977: Kinematic analysis and air-sea heat flux associated with mesoscale cellular convection during ATMEX 75. *J. Atmos. Sci.*, **34**, 793-801.

Van Delden, A., 1986: On the preferred mode of cumulus convection. *Beitr. Phys. Atmos.*, **58**, 202-219.

Walter, B.A., and J.E. Overland, 1984: Observations of longitudinal rolls in near neutral atmosphere. *Mon. Wea. Rev.*, **112**, 200-208.

Walters, B.A., Jr., 1986: The mesoscale organization, dynamics, and evolution of the marine planetary boundary layer during cold air outbreaks. PhD. dissertation, University of Washington, 200pp.

Zivkovic, M., and E.M. Agee, 1989: Further aspects of transitions in two dimensional thermal convection. *J. Atmos. Sci.*, **24**, 3983-3995.